C13.10:257

Microstructure of Ceramic Materials

Proceedings of an
American Ceramic Society Symposium
Pittsburgh, Pa., April 27–28, 1963

United States Department of Commerce
National Bureau of Standards
Miscellaneous Publication 257

C 13.10:257

PENNSYLVANIA STATE UNIVERSITY
MAR 4 1969
DOCUMENTS COLLECTION

UNITED STATES DEPARTMENT OF COMMERCE • Luther H. Hodges, *Secretary*
NATIONAL BUREAU OF STANDARDS • A. V. Astin, *Director*

Microstructure of Ceramic Materials

Proceedings of a Symposium

April 27–28, 1963

Held under the auspices of the Ceramic Educational Council of the American Ceramic Society, with the cooperation of the National Bureau of Standards, and under the sponsorship of the Edward Orton Junior Ceramic Foundation and the Office of Naval Research. The Symposium took place at the 65th Annual Meeting of the American Ceramic Society in Pittsburgh.

National Bureau of Standards Miscellaneous Publication 257

Issued April 6, 1964

For sale by the Superintendent of Documents, U.S. Government Printing Office, Washington, D.C., 20402
Price $1.75 (Buckram)

Library of Congress Catalog Card Number: 64–60020

Contents

		Page
Introduction		iv
1.	Geometry of Microstructures	1
	Lawrence H. Van Vlack Department of Chemical and Metallurgical Engineering University of Michigan Ann Arbor, Michigan	
2.	Experimental Techniques for Microstructure Observation	15
	Van Derck Frechette Alfred University Alfred, New York	
3.	The Effect of Heat Treatment on Microstructure	29
	Joseph E. Burke Research Laboratory General Electric Company Schenectady, New York	
4.	Correlation of Mechanical Properties with Microstructure	41
	Robert J. Stokes Research Center Minneapolis-Honeywell Regulator Co. Hopkins, Minnesota	
5.	Microstructure of Magnetic Ceramics	73
	A. L. Stuijts Philips Research Labs. Eindhoven Netherlands	
6.	Microstructure of Porcelain	93
	Sten T. Lundin Royal Institute of Technology Stockholm Sweden	

Introduction

In all materials, the physical and even the chemical properties of a polycrystalline body are not exactly the same as those of a single crystal of the same materials. Many materials are anisotropic - their properties depend upon the orientation of the measuring system with respect to the crystallographic axes - and the polycrystalline properties are some form of an average over the crystal directions. Thus the dielectric constant, elastic constants, index of refraction, magnetic susceptibility, and many other "bulk" properties depend to some extent on the microstructure of the specimen.

Beyond this, some properties depend on the motion of various entities through the material-transport of atoms and ions in diffusion, transport of phonons in thermal conduction and electrons and ions in electrical conduction, motion of dislocations and other defects in plastic deformation and of domain walls in ferromagnetic and ferroelectric switching, and even the propagation of cracks in fracture. In these transport processes, the grain boundaries between the crystals in a polycrystalline body behave differently from the bulk material, and their presence markedly affects the resulting properties. Diffusion is usually faster at grain boundaries, especially at low temperatures, so that diffusion is enhanced in polycrystalline bodies. Electrons and phonons are scattered by grain boundaries, so that electrical and thermal conduction tends to be lower in the polycrystals. The movements of dislocations across grain boundaries are impeded, so that plastic deformation is inhibited by their presence, and polycrystalline bodies tend to be stiffer and less ductile than the corresponding single crystals.

Finally, the presence of grain boundaries not only modifies the behavior, but sometimes even introduces new elements. Thus in brittle fracture the grain boundaries provide sources of cracks, making polycrystals weaker in general than single crystals. The presence of strain and of impurities at grain boundaries raises the local free energy, so that chemical effects, such as etching rates, are enhanced.

It is clear, then, that a knowledge of the microstructure of a polycrystalline body is essential in any attempt to study and control its properties. This is particularly important in the field of ceramics, where the overwhelmingly important form is the polycrystalline body. In order to review the problems involved in specifying and studying microstructure in ceramics and the factors involved in the interaction between microstructure and physical properties of ceramics, this Symposium on Microstructure of Ceramic Materials was held. The papers presented are published in this volume. Primary responsibility for their technical content must rest, of course, with the individual authors and their organizations.

In the first two Chapters, Prof. Van Vlack reviews the geometry of microstructures and how they can be specified and Prof. Frechette describes the principal experimental techniques by which observations of microstructures are made. In Chapter 3, Dr. Burke then describes the factors controlling the development of the microstructure during heat treatment of the ceramic, and their relation to the processing variables of time and temperature.

In the next two Chapters, Dr. Stokes discusses the influence of microstructure on the mechanical behavior, and Dr. Stuijts describes the influence on the ferromagnetic properties of ferrites. In the last Chapter, Prof. Lundin examines in detail the microstructure of one material, porcelain, and its ramifications.

Ivan B. Cutler, Chairman
University of Utah

Willis E. Moody, Co-Chairman
Georgia Institute of Technology

Joseph E. Burke
General Electric Company

Alan D. Franklin, Editor
National Bureau of Standards

William D. Kingery
Massachusetts Institute of
Technology

Geometry of Microstructures

Lawrence H. Van Vlack

1. Introduction

The internal structure that a material possesses on a microscopic scale is generally called microstructure. This presentation is concerned with the geometry of such microstructures as encountered in ceramic materials.

A study of microstructures does not involve the study of atomic coordination as it exists in various crystalline and amorphous phases. However, it does involve the phase and grain relationships at the lower end of the electron microscopic range, and extends through the size spectrum up to and well into the "hand lens" range. Examples at the lower end of the microstructural size range include the nuclei which start the crystallization of glass and therefore introduce a heterogeneity of structure. Microstructures at the coarse end of the size range are found in ceramic products which can be illustrated by abrasive grinding wheels. These products contain a distribution of specific sizes and shapes of abrasive phases that are bonded with a silicate or similar material and include closely controlled porosity.

The geometric variations which are encountered in microstructures include (1) size, (2) shape, and (3) the preferred orientation of constituent grains[1] (Fig. 1). In addition, when more than one phase is present, there can be the added variables: (4) amount of phases, and (5) the distribution of phases among each other (Fig. 2). Item (4) above is most closely related to the chemistry of the ceramic product because the amount of phases depends directly upon the composition. The other structural variables are less closely related to the composition and depend more specifically upon factors of processing and service history. Each of the preceding five microstructural variations involves grain boundaries and the consequent crystal structural discontinuities.

Many ceramic materials possess porosity. From a microstructural point of view, pores can be considered as an additional phase of zero composition. Of course this "phase" is a very important feature in the microstructure, because the pores markedly affect the microstructural dependent properties.

As will be pointed out in later presentations, the microstructures and therefore the consequent properties of the ceramic are not static in behavior, for they may be altered by external factors such as mechanical forces, thermal conditions, chemical environments, and electric or magnetic fields. Therefore, a microstructure may be varied by processing factors and servicing conditions. This presentation will first consider the characteristics of internal boundaries, then single phase microstructures, and finally polyphase microstructures.

2. Internal Boundaries

The most general characteristic of a microstructure is the presence of its internal boundaries which separate the grains and phases within the material. Whether these internal boundaries are between the disoriented grains of one phase, between grains of different phases, or between electrical and magnetic domains of one grain, they represent a specific change in the internal structure of the ceramic. Internal boundaries are thus an important feature in a ceramic and have significant effects on the properties of the material.

It is possible to characterize boundaries as grain boundaries, domain boundaries, phase boundaries, or surfaces. However, such characterization is usually unnecessary for a general discussion, because each of the above boundaries may be considered to be a surface or zone of crystalline mismatch. Boundary discontinuities in a microstructure

[1]The term, grain, as used in the discussion of microstructure denotes a single crystalline volume. This is in contrast to grog grains which are usually 1-10 mm in size and contain numerous small crystals.

represent locations of higher atomic energies; therefore a "driving force" exists which tends to reduce the boundary areas with consequential boundary movements.

2.1. Boundary Structure

The atomic structure of a grain or phase boundary must be inferred because it is currently impossible to view the involved atoms directly. However, several conclusions may be made about these boundaries as a result of indirect experimental evidence and on the basis of appropriate models. In doing so, several types of boundaries can be cited. The first of these is the small-angle boundary which consists of aligned dislocations as illustrated in Fig. 3. Experimental evidence strongly supports this structure. For example, since dislocations are revealed by etching, it is a simple procedure to determine the angle of this boundary from the spacing of the etch pits and lattice dimensions. An independent and corroborative check of the angle can then be made by diffraction measurements. Figure 4 reveals such etching pits along small angle boundaries in LiF. Similar boundaries have been observed in other materials such as Al_2O_3 and TiO_2 and have received specific interest in view of their indication of deformation and its consequences [1,2].[2]

Large-angle boundaries are most simply represented by Fig. 5. This can be considered to be typical of most of the boundaries which are found between grains and phases within various materials. Again it is impossible to be specific about the structures along these boundaries except by inference. However, substantial evidence does imply that the boundaries represent a zone of mismatch in atom spacings with a consequence that the atoms at the boundary are at a higher energy level than those within the grain proper. Furthermore, the mismatch produces relatively large interstices between the atoms for grain boundary diffusion and for impurity absorption. Because such boundaries possess atoms with higher energies, it comes without surprise that the boundary is frequently the site for nucleation and subsequent crystalline growth.

Twins, a not uncommon feature of mineral phases, represent a special large angle boundary situation, in which the adjacent grains are coherent with one another (Fig. 6). The only mismatch involves second-neighbor and more distant atoms.

Coherent boundaries may arise between unlike phases as represented in Fig. 7. As with twin boundaries, coherency between phases is favored by specific crystallographic orientations in which the atoms along the boundary are part of the two adjacent phases. The presence of these boundaries leads to Widmanstatten-type structures as shown in Fig. 8.

Domain boundaries are often categorized separately from the above boundary types. However, there is no specific reason for such separation because they also represent surfaces or zones of mismatch between adjacent groups of coordinated atoms. This is indicated in Fig. 9 where separate parts (domains) of a single crystal will have opposing polarity as a result of inverted unit cell alignments. The boundary between these areas is shown schematically in Fig. 10 as a transition zone which possesses higher energy because of the changing alignment.

2.2. Boundary Energies

The interatomic spacings within equilibrated phases are such that the atoms possess the lowest total energy. Higher energies exist when the interatomic spacings are either increased or decreased. The major part of the boundary energy arises from the variation in the spacing of adjacent atoms at the boundary. Additional but smaller energies are required for the mismatch of second-neighbor or more distant atoms. It may be deduced from the above that the large-angle boundaries have high energies, while small-angle boundaries, twin boundaries, and coherent phase boundaries have lower energies. This conclusion may be verified by calculations and by experiments.

Since the small-angle boundary is a series of aligned dislocations, its energy may be calculated as a summation of the energy associated with each of the individual dislocations. As such, it possesses energies ranging from 0 to 100 ergs/cm^2.

The energies of several large-angle metallic boundaries are indicated in Table 1 [3]. The determination of these energies commonly involves the experimental use of dihedral angle measurements which are illustrated in Fig. 11 as a vectoral balance [4]. Since the boundary area requires extra energy, there is a natural

[2] Figures in brackets indicate the literature references at the end of this paper.

tendency for this area to be reduced. Thus the angle along grain and phase edges undergoes an adjustment which is mathematically equivalent to the result of a surface tension in the following relationship:

$$\frac{\gamma 1/3}{\sin \phi_2} = \frac{\gamma 1/2}{\sin \phi_3} = \frac{\gamma 2/3}{\sin \phi_1} \quad . \tag{1}$$

When two of the boundaries are comparable, Eq. 1 reduces to:

$$\gamma_{a/a} = 2\, \gamma_{a/b} \cos \frac{\Theta}{2} \tag{2}$$

as shown in Fig. 11(b). The dihedral angle, Θ, is a special case of the edge angle ϕ. The energy of the boundary or interface between two grains or phases is represented by γ. It is necessary to use statistical methods to determine the two dihedral angles accurately if the observed angles are on a random 2-dimensional plane through the usual 3-dimensional microstructure [5]. However, a reasonably accurate approximation is obtainable from the median angle of a small number of observed angles [6]. Thus, comparative values may be made of the boundaries of several types.

The energy of boundaries between adjacent grains of the same phase will vary with the relative orientation of the two adjacent grains. The extreme case is that of two grains with identical orientation in which the boundary disappears and the energy drops to zero. As the adjacent grains are rotated out of alignment, the boundary energy is increased until there is a maximum amount of mismatch between the structures of the two grains [7]. The specific orientation with these higher energies will vary with the structure of the grains and with the direction of rotation. However, for many materials it can be concluded that most boundaries have energies close to the maximum and only a few favored low angle and twin orientations diverge significantly from the maximum energy values.

2.3. Boundary Movements

The average grain size of a single-phase ceramic will increase with time if the temperature is such as to give significant atom movements. The driving force for such grain growth is the free energy released as the atom moves across the boundary from the convex surface to the concave surface where the atom becomes coordinated with the larger number of neighbors at equilibrium atom spacings (Fig. 12). As a result, the boundary moves toward the center of curvature (Fig. 13), and the larger grains will grow at the expense of the smaller grains. This is true in both single phase microstructures and polyphase microstructures, as will be indicated later. The net effect is less boundary area per unit volume.

Boundary movements are influenced by grain size, temperature, and the presence of insoluble impurities. Smaller grain sizes provide a greater driving force for atom movements across the boundary as indicated in the previous paragraph. Beck [8] has provided the relationship:

$$dD/dt = k/D^m \quad , \tag{3}$$

where D is the index to grain diameter, t is time and k and m are constants. Since experimental data indicate the value of m is close to 1, this equation integrates to:

$$D^2 - D_o^2 = 2\, kt \quad . \tag{4}$$

Therefore the change in cross-sectional area of the grain is nearly proportional to time, or if the initial size may be assumed to be zero, the diameter increases with the square root of time. The value of k in Eq. 3 and 4 is usually an exponential function of temperature in which k reflects the activation energy for the atom movements shown in Fig. 12.

The most obvious limitation to grain growth occurs as the grain size approaches the dimensions of the ceramic product, and therefore grain growth is inhibited. A less obvious, but equally important, limitation occurs in the presence of an inhibiting second phase as shown in Fig. 14. In general, the boundary as seen in two-dimensions must be increased and the curvature reversed locally before a boundary can move beyond the dispersed particles, thus inhibiting grain growth. Zener [9] has presented the following relationship for the limitation of boundary movements:

$$R/r \approx 1/f \tag{5}$$

R and r are the radii of curvature for the grain surface and the dispersed phase respectively. The volume fraction of the dispersed phase is given as f. Such grain growth inhibitors have been used in various ceramic materials such as Al_2O_3 and MgO.

The movements of domain boundaries are accentuated by the introduction of an externally applied field. This is achieved by the inverting of the polarity of the cells within and adjacent to the boundary zone so as to expand the favorably aligned domains and reduce the volume of the unfavorably aligned domains (Fig. 15). These boundary movements are reversible as the external field is inverted. Domain boundary movements, like grain boundary movements, are influenced by the presence of external surfaces and by impurity particles.

3. Single Phase Microstructures

It was pointed out previously that a single phase microstructure may have variations in grain size, grain shape, and preferred orientation of the grains. These are not wholly independent because grain shape and grain size are both consequences of grain growth. Likewise, the grain shape is commonly dependent on the crystalline orientation of the grains during growth. In the simplest situation the grain may be considered to be uniform in size, equiaxed in shape, and random in orientation. This can be illustrated in Fig. 16 for periclase (MgO).

3.1. Grain Size and Boundary Area

The grain size as shown in Fig. 16 does not indicate the true grain size distribution inasmuch as that figure reveals a random 2-dimensional section through a 3-dimensional solid, and very few grains show a maximum cross-sectional area. A theoretical distribution of grain size areas for uniform grain size would provide a median area of about 0.8 of the maximum area. Since the various measurements in ceramics reveal that the median area is less than the above figure, it is to be concluded that there is a distribution of grain sizes. This is to be expected since the process of grain growth requires that certain grains decrease in size and disappear (Fig. 13). Burke [10] has shown that this does not proceed uniformly for any one grain because of the complex boundary network around any disappearing grain. Smith [11] used a soap bubble as a model for grain growth and boundary movement. Since the analogy is theoretically sound, qualitative comparisons are justified. This procedure provides the suitable means of studying changes in 3-dimensional solids.

Abnormal grain growth may occur in materials. Burke [10] explains such growth in metals by noting that if an individual grain is favored to become significantly larger than the balance of the grains, then it possesses an additional advantage for still further grain growth by virtue of sharper boundary curvatures (Figs. 17 and 18). The circumstances which produce the initial size advantages for specific grains can only be surmised. However, factors such as impurities, the distribution of inhibiting particles, location of nucleants, and the oxidation of adjacent grains are undoubtedly important.

Grain size has commonly been indicated as the grain diameter. Also, an ASTM procedure assigns a number, n, to a grain size where,

$$N = 2^{n-1} \qquad (6)$$

and N is the number of grains observed in 0.0001 sq. in. of a 2-dimensional section (i.e., 1 $in.^2$ at a magnification of X100). These are appropriate for those microstructures in which it may be assumed that all grains are spheres with identical diameters. Since microstructures seldom if ever meet these conditions, diameters and grain numbers are at best only an index of size.

Statistical procedures are available which take into account a distribution of actual sizes, as well as a distribution of observed sizes in a microstructure which arises because the grains are not cut through their greatest diameter [12,13]. Such procedures require a knowledge of shape and size distributions before they are meaninfgul. An alternate index of grain size is that of determining the grain boundary area in a microstructure without regard to shape or size distribution. This area is often more important than the grain size per se, because the amount of area influences the properties which arise out of the microstructures. Several workers [12,14] arrived independently at the following extremely simple relationship:

$$B_V = 2 N_L$$

In this equation, B_V is the boundary area (mm^2) per unit volume (mm^3), and N_L is the

number of grain boundaries traversed per millimeter by a random line. The several derivations of this equation are cited by Underwood [13] and Saltykov [12]. The significant feature about Equation 7 is the fact that the boundary area is measurable without determining the grain size and may be determined for materials with non-uniform grain sizes. The only requirement is that the sample lacks grain size gradients or grain shape heterogeneities.

The use of the random line technique is illustrated in Fig. 19 for the MgO of Fig. 16. Several lines give a figure of about 85 grains/mm, thus indicating a boundary area of 170 mm^2/mm^3.

It is possible in a single phase material to relate the number of grains per unit volume, N_V, to the boundary area, B_V, in that volume, if some assumptions are made concerning the grain shapes.

$$N_V = (B_V/F)^3 \tag{8}$$

where F is a shape factor equal to 3.0, 2.86, 2.67, and 2.66, respectively for cubes hexagonal prisms, rhombic dodecahedrons, and truncated octahedrons, i.e. cube-octahedrons [15]. Underwood [15] concludes that the latter are most appropriate in equiaxed microstructures. Thus Equation 8 reduces to

$$N_V = B_V^3/19 \tag{8a}$$

$$N_V = 0.42\ N_L^3 \tag{8b}$$

As a result, the MgO ceramic of Fig. 16 would contain about 260,000 grains per mm^3. Although this number could be converted to an equivalent grain "diameter," it is not recommended because assumptions would have to be made concerning grain shapes.

3.2 Grain Shape

Although it is common to speak of grain size in terms of diameter, it is obvious that grains of single-phase, nonporous ceramics are not spherical. Rather, they must completely fill space and also maintain a minimum in total boundary energy. Thus, they have an irregular shape at best. The term, equiaxed, is used for those grains that have approximately equal dimensions in the three coordinate directions. This is the case for the periclase (MgO) of Fig. 16. In other cases there can be an elongation in one direction as indicated for UO_2 in Fig. 20.

The grain shape in a single phase material may be described by a length/width ratio. Thus both the schematic microstructure of Fig. 1(c) and the actual microstructure of Fig. 20 would possess an L/W ratio between 3/1 and 4/1, depending on whether maximum or typical widths are used. Here, as with grain size, we also encounter the question of 3-dimensional sizes vs. 2-dimensional observations. As a result it may be desirable to utilize a statistical calculation of shape when there is an elongation to the structure. However, instead of using the random lines of Equation 7, lines are intentionally aligned in the two principal coordinate directions. An elongation, E, may be calculated.

$$E = \frac{(N_L)_\perp - (N_L)_\parallel}{(N_L)_\perp + (\pi/2-1)\ (N_L)_\parallel} \tag{9}$$

As before, N_L is the number of grain boundaries traversed per mm; $\parallel$ and $\perp$ indicate the two principal coordinate directions; and E is the degree of elongation [13]. The degree of elongation for Fig. 1(c) is about 0.55. This is in contrast to zero elongation for the other three sketches of Fig. 1, and 1.0 for perfect elongation.

Microstructures may possess patterns of elongation of the grain shapes other than those shown in Fig. 1(c) where it is implied that the elongation in one direction is greater than the other two, i.e., $(N_L)_a < (N_L)_b = (N_L)_c$. Other possibilities include $(N_L)_a = (N_L)_b < (N_L)_c$, and $(N_L)_a < (N_L)_b < (N_L)_c$. Because of these possibilities, it is not safe to draw conclusions about the grain shape and microstructural elongation on the basis of <u>one</u> section only. As the minimum, it is necessary to examine two perpendicular sections.

At this point it should be noted that there is a major contrast between metals and ceramics. Because the grain shapes in single-phase metals normally tend to be equiaxed,

elongated grains in metals are generally achieved as a consequence of processing factors such as deformation and recrystallization. In contrast, it is not uncommon to have considerable anisotropy in the growth rates of ceramic grains with microstructures, and as a rule, deformation and recrystallization are not important factors.

3.3. Preferred Orientation of Grains

The crystalline orientation of the various grains in single-phase ceramic products is typically quite random. Unlike metals, these ceramic products are not subject to mechanical deformation, which favors an alignment of the individual grains both before and after recrystallization. However, ceramic products with a preferred orientation are possible and will undoubtedly have increased significance in the future. Grains in a ceramic which are nucleated at an external surface to produce columnar recrystallization commonly will have a preferred orientation with the fastest growth direction aligned with the grain length (Fig. 20). Those grains which were nucleated so they grew in other orientations were soon overtaken by the more favorably oriented grains. Other factors, such as electrical or magnetic fields, become important in grain orientation if they are present at the time when the product is made. This subject will undoubtedly be covered in subsequent lectures.

Preferred orientation (Fig. 1d) may be indicated geometrically as the direction favored for the normals to specific crystal planes. Thus the preferred orientation of UO_2 in Fig. 20 is <100>, which was the direction of the thermal gradient during solidification. This orientation is obviously not perfect, because if it were there would be no remaining boundaries of mismatch, and only a large single crystal would result. Quantitative measures of the amount of preferred orientation are difficult. However, pole figures do provide an indication of the amount [16].

4. Polyphase Microstructures

4.1. Introduction

The microstructural variations of polyphase (and porous) materials involve not only the previously cited (1) grain size, (2) grain shape, and (3) preferred orientation, but also the geometric relationships of the phases. Included are: (4) the relative amounts of the phases, and (5) the mutual distribution of the two or more phases which are present.

An analysis of the first three geometric factors for polyphase microstructures may be approached much as they were for single-phase microstructures. Equation 7 may be used to describe the amount of any type of interface per unit volume. Thus, Fig. 8 can be shown to have 900 mm^2/mm^3 of coherent $UC-UC_2$ interface. Likewise, the domain boundary area of Fig. 9 is about 700 mm^2/mm^3. Since the latter microstructure contains dispersed domains within continuous matrix (also a domain), it is possible to determine the average size of the dispersed areas from their numbers [15]. Also, relatively simple micrographic procedures permit a determination of the distribution of true plate thicknesses and spacings of the $UC-UC_2$ microstructure shown in Fig. 8. The reader is referred to Cahn and Fullman [17] for further elaboration.

The energy of a phase boundary, like the energy of a grain boundary, is a driving force which promotes grain growth in polyphase ceramics. Figure 21 illustrates the changes which occur with added time and elevated temperatures [19]. The relative amounts of the two phases are identical in the two examples, thus indicating chemical or phase equilibrium. However, geometric equilibrium has not been fully attained, and in fact will not be as long as there is an opportunity for further grain growth. In effect, the growth process which is shown in Fig. 21 requires steps of solution (of grains with small radii of curvature), diffusion, and precipitation (onto grains with larger radii of curvature). Thus, unless the atomic mobilities and surface energies are high, the growth process is slower in polyphase materials than in single phase microstructures where the atoms simply move across the grain boundary (Fig. 12).

The grain shape analysis of single phase microstructures (Equation 9) may be used only if there is an alignment of the grain shapes. Even so, it is possible to obtain information concerning the shapes of dispersed grains which are not equidimensional. For example, the mullite grains which are present in a siliceous glass in Fig. 22 are acicular, or needle-like prisms with an euhedral outline of $a \approx b < c$. Hence we generally observe only the small cross-section. Occasionally, a grain lies in such a manner that its major elongation is revealed. Likewise, the corundum of Fig. 23 (also present in a siliceous glass) develops a plate-like grain which commonly reveals an elongated trace on the 2-dimensional microsection. This arises because $a \approx b > c$. In this example, however, the third dimension is not as markedly different from the two

as it was in Fig. 22, so the plate-like characteristics are less commonly revealed.

4.2. Amounts of Phases

It is assumed that the reader is familiar with the relationships between relative amounts of two or more phases and the compositions of ceramic materials as indicated by a phase diagram. Therefore, that subject will be passed with only a mention of references [18,20].

There are several procedures for determining the quantity of a selected phase within a microstructure. They all provide volumetric answers; so, of course, subsequent calculations are required if weight percentages are desired. Point analyses and linear analyses are the most widely recommended procedures (Fig. 24).

Point analyses utilize the following relationship:- a random point in a microstructure has a probability of lying within each phase which is equal to the volume percent of that phase within the microstructure. The linear analysis is based on a similar probability, viz., a random line will be within any phase in proportion to the amount of that phase. It can be shown that a point analysis can be slightly more accurate than the linear analysis for a given amount of effort on the part of the micrographer. In each case, special efforts must be maintained to avoid any-nonstatistical selection of points or lines, and care should be taken so that one phase is not preferentially lost during sample preparation. On the other hand, if the microsection is representative, microporosity can be determined by either of these two methods simply by determining the volume of the pore space as a fraction of the total volume.

Assuming that the microscopic section is representative of the whole structure, and statistical randomness has been maintained, the binomial accuracy standard deviation of the data is given by the following relationship:

$$\sigma_v = \sqrt{F(1.0 - F)/N} \quad , \tag{10}$$

or the fraction may be estimated from:

$$F = (1 \pm \sqrt{1 - 4N\sigma_v^2})/2 \quad . \tag{10a}$$

Within these equations, σ_v is the standard deviation of analyzed volume fractions from successive samplings, $\underline{F}$ is the estimated true fraction, and $\underline{N}$ is the number of randomly selected observation points.

4.3. Distribution of Phases

The mutual distribution of two or more phases within a microstructure can be a result of (1) changes in chemical equilibrium which modify the relative amounts of phases, and (2) geometric equilibrium which arises from boundary energy relationships.

Changes in chemical equilibrium introduce solution and precipitation. This can be illustrated by Fig. 25 where tridymite is present in a silica-saturated iron oxide liquid. During the active growth of the tridymite crystals, there was an euhedral development of the crystal faces so that the boundaries are regular between the two phases.

Geometric equilibrium often develops more slowly than chemical equilibrium. This is demonstrated when Fig. 26 is contrasted with Fig. 25. The two have the same composition and the same volumetric phase ratios. However, with time at temperature, there has been a partial anhedralization which reduces the total interface area (and energy). The degree of anhedralization varies with the material. The microstructures of Fig. 21 do not show euhedral growth of wüstite (FeO) in the times indicated. However, some crystal faces are developed on the grains when saturation is exceeded during a quench.

The distributional variations of phases become most noticeable when one of the phases is a liquid. The schematic presentation of Fig. 2 is illustrated in actual microstructures in Figs. 27 and 28. In the simplest case, it is possible to have a liquid phase penetrate along the grain boundaries (Fig. 27). Under such a condition there is negligible solid-to-solid contact at the elevated temperatures with consequent effects upon properties [21]. Also, subsequent effects may be realized at lower temperatures as indicated in Fig. 29 where the fracture path follows the silicate phase which was originally distributed as a high temperature liquid.

A contrast to the foregoing conditions is shown in Fig. 28 where solid-to-solid contact was maintained between cristobalite grains by a finite dihedral angle [22].

Thus, although there are channels of liquid distributed through the microstructure, there remains a solid skeleton which maintains significant strength at high liquid contents.

The microstructural differences between Figs. 27 and 28 must be accounted for through the relative interfacial energies as indicated in Equation 2. In general, it may be concluded that the phase boundary energy is least when the compositions of the two adjacent phases are most similar (other things equal). In Fig. 28, there is a markedly greater dissimilarity in the compositions between the cristobalite (SiO_2) and the liquid than there is between the wüstite (FeO) and liquid in Fig. 27. Furthermore, all evidence would suggest that the grain boundaries between two cristobalite grains would have a relatively low energy as contrasted to the energy between two wüstite grains because the cristobalite has a low packing factor and therefore has additional degrees of freedom to compensate for the mismatch which accompanies the boundary.

5. Conclusions

The internal structure of a material may be analyzed on a basis of geometry with factors such as grain size, grain shape, grain orientations being important in single-phase microstructures. Polyphase microstructures will include these variables plus the variation in the quantities of the individual phases and their juxtaposition or distribution.

While there are both qualitative and quantitative data on the factors which affect geometric equilibrium and microstructures, it has been impossible in this presentation to present comparable information on the kinetics, or rate of obtaining geometric equilibrium within the microstructures. This is a more complex consideration with only a smattering of analytical information. At the same time it may be a major consideration because relatively few microstructures within ceramic materials will have gained full geometric equilibrium at the time of their use in engineering applications.

6. References

[1] R. Scheuplein and P. Gibbs, Surface Structure in Corundum: I. Etching of Dislocations, J. Am. Ceram. Soc. 43, 458 (1960).

[2] W. M. Hirthe and J. O. Britton, Dislocations in Rutile as Revealed by the Etch Pit Technique, J. Am. Ceram. Soc. 45, 546 (1962).

[3] D. McLean, Grain Boundaries in Metals, p. 77, Clarendon Press (Oxford, 1957).

[4] C. S. Smith, Grains, Phases and Interfaces: An Interpretation of Microstructure, Trans. AIME, 175, 15 (1948).

[5] D. Harker and E. Parker, Grain Shape and Grain Growth, Trans. ASM 34, 156 (1945).

[6] O. K. Riegger and L. H. Van Vlack, Dihedral Angle Measurement, Trans. AIME 218, 933 (1960).

[7] C. G. Dunn and F. Lionetti, The Effect of Orientation Difference on Grain Boundary Energies, Trans. AIME 185, 125 (1949).

[8] P. A. Beck, Effect of Recrystallized Grain Size in Grain Growth, J. Appl. Physics 19, 507 (1948).

[9] C. Zener, Grains, Phases and Interfaces: An Interpretation of Microstructure, Trans. AIME 175, 48 (1948).

[10] J. E. Burke, Recrystallization and Grain Growth, Grain Control in Industrial Metallurgy, p. 1, Am. Soc. Metals (Metals Park, O., 1948).

[11] C. S. Smith, Grain Shapes and Other Metallurgical Applications of Topology, Metal Interfaces, p. 65, Am. Soc. Metals (Metals Park, O., 1951).

[12] S. A. Saltykov, Stereometricheskaya Metallografiya, Literatury Po Chernoy I Tsvetnoy Metallurgii (Moskva, 1958).

[13] Ervin E. Underwood, Surface Area and Length in Volume, Quantitative Metallography, New York, McGraw-Hill, to be published.

[14] C. S. Smith and L. Guttman, Measurement of Internal Boundaries in Three-Dimensional Structures by Random Sectioning, Trans. AIME 197, 81 (1953).

[15] Ervin E. Underwood, Quantitative Metallography, Metals Engineering Quarterly, 1, [3] 70 (Aug., 1961). Also see 2, [4] 62 (Nov., 1961) for Part 2 of the article.

[16] B. D. Cullity, Elements of X-ray Diffraction, p. 272, Addison-Wesley Pub. Co. (Reading, Mass., 1956).

[17] J. W. Cahn and R. L. Fullman, On the Use of Lineal Analysis for Obtaining Particle Size Distribution Functions in Opaque Samples, Trans. AIME 206, 610 (1956).

[18] E. M. Levin, H. F. McMurdie, and F. P. Hall, Phase Diagrams for Ceramists, Am. Ceram. Soc. (Columbus, Ohio, 1956).

[19] L. H. Van Vlack and O. K. Riegger, Microstructures of Magnesio-wüstite [(Mg,Fe)O] in the Presence of SiO_2, Trans. AIME 224, 957 (1962).

[20] L. H. Van Vlack, Physical Ceramics, Addison-Wesley Pub. Co. (Reading, Mass., 1964).

[21] O. K. Riegger, G. I. Madden, and L. H. Van Vlack, The Microstructures of Periclase When Subjected to Steel-Making Variables, Trans. AIME (1963), in press.

[22] L. H. Van Vlack, The Microstructure of Silica in the Presence of Iron Oxide, J. Am. Ceram. Soc. 43, 140 (1960).

Table 1. Energies of Metallic Boundaries*

Boundary	Energy
Copper	646 ergs/cm^2
Iron (γ)	850
Silver	400
Copper twin	19
Iron twin (112)	187
Aluminum twin	120

* Adapted from D. Mclean, Grain Boundaries in Metals, p. 77, Clarendon Press (Oxford, 1957).

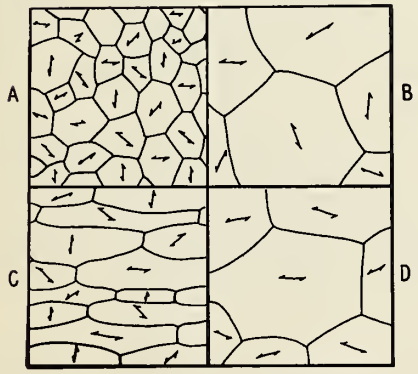

FIGURE 1. Microstructural variables (single-phase materials). (a vs. b) Grain size. (a vs. c) Grain shape. (b vs. d) Preferred crystal orientation. (Schematic.)

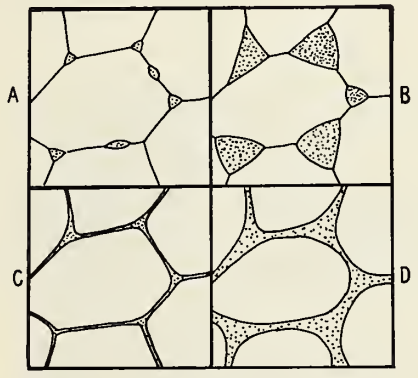

FIGURE 2. Microstructural variables (polyphase materials). These are in addition to those of fig. 1. (a vs. b) and (c vs. d) Amounts of phases. (a vs. c) and (b vs. d) Distribution of phases. (Schematic).

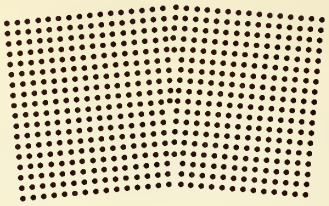

FIGURE 3. Small-angle boundary (schematic). This discontinuity in the microstructures consists of a series of aligned edge dislocations.

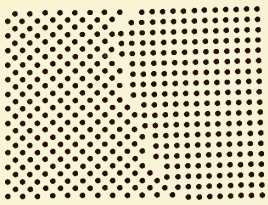

FIGURE 5. Large-angle grain boundary. Although this schematic representation probably oversimplifies the grain boundary structure, it does indicate the major mismatch of structure which results.

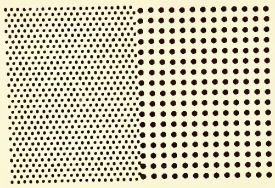

FIGURE 7. Coherent boundary (schematic). The adjacent phases have a closely matching repetition in structure.

FIGURE 9. Domains. Example: $BaTiO_3$ aligned with the c-axes perpendicular to the figure (X5625). Etched by H_3PO_4. The positive ends etched more rapidly than the negative ends. [Belitz, R. K., "Differential Etching of $BaTiO_3$ by H_3PO_4," J. Am. Ceram. Soc. 45, 617 (1962)].

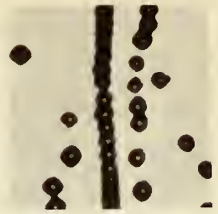

FIGURE 4. Small-angle boundary. Example: Etch pits in LiF (X225). Each etch pit is the site of an edge dislocation. The angle of the boundary can be calculated from the spacing of the dislocations.
(courtesy A. S. Keh.)

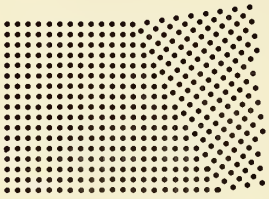

FIGURE 6. Twin boundary (schematic). The mismatch does not involve first-neighbor atoms.

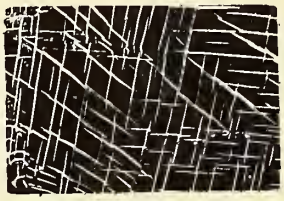

FIGURE 8. Widmanstatten structures. Example: UC_2 (bright) in UC (X281). [Chang, R., and C. G. Rhodes, "High-Pressure Hot-Pressing of Uranium Carbide Powders and Mechanism of Sintering of Refractory Bodies," J. Am. Ceram. Soc. 45, 379 (1962].

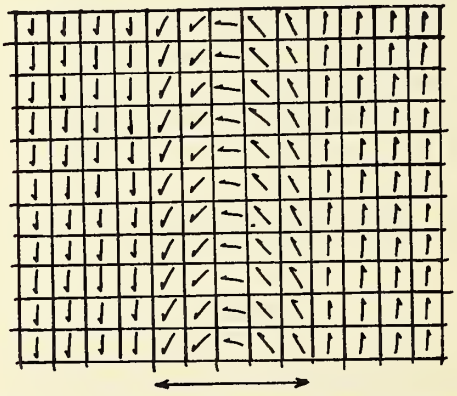

FIGURE 10. Domain boundaries (schematic). The realignment across the boundary requires energy. Therefore, there is a driving force to reduce the boundary area.

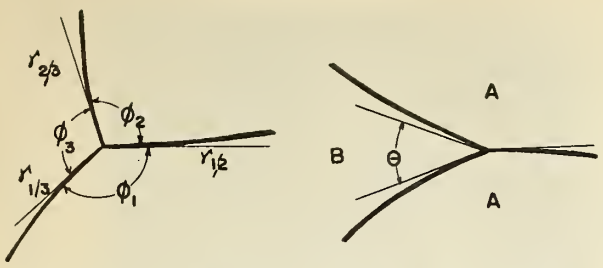

FIGURE 11. Energy balances. (a) Three unlike boundaries eq (1). (b) Dihedral angle between two like grains eq (2).

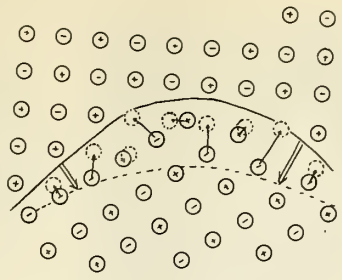

FIGURE 12. Boundary movements. Less energy is required to move an atom or ion from the surface of the grain with a convex surface to a grain with a concave surface than in the opposite direction. Therefore the boundary moves toward the center of curvature.

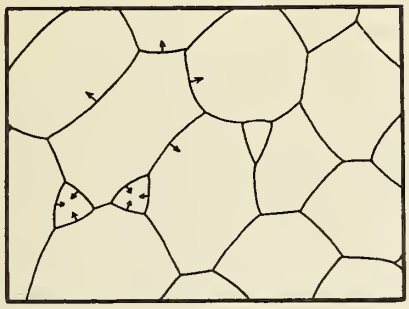

FIGURE 13. Grain growth. The movement of boundaries toward their centers of curvature produces grain growth and a disappearance of the smaller, more spherical grains.

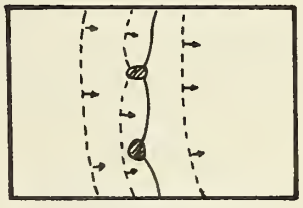

FIGURE 14. Growth inhibition. Second phases generally retard boundary movements because they introduce reversals in boundary curvature.

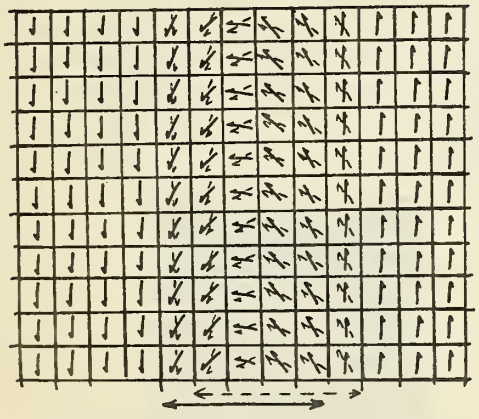

FIGURE 15. Domain boundary movements. The partially aligned dipoles along the boundary (fig. 10) are pulled into orientation with the external field, thus shifting the boundary zone.

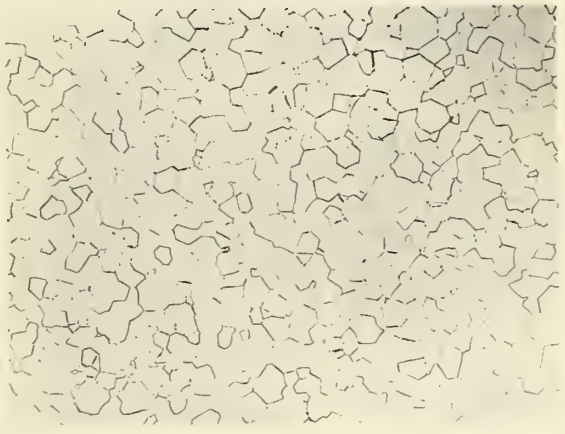

FIGURE 16. Equiaxed grains. Example: periclase (MgO). (approx. X140). This microstructure corresponds to that in fig. 1(a). [R. F. Gardner and G. W. Robinson, Jr., "Improved Method of Polishing Ultra-High Density MgO," Am. Ceram. Soc. 45, 46 (1962)].

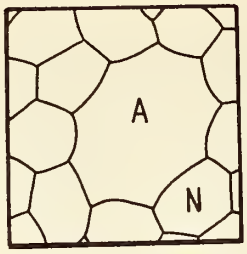

FIGURE 17. Abnormal grain growth (schematic). Abnormally large grains (A) have faster growth rates than normal grains (N) because the radii of curvature of their boundaries are smaller.

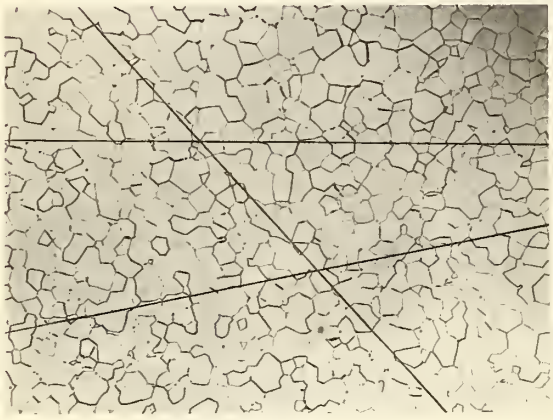

FIGURE 19. Boundary measurement. Example: random line technique. Eq (7) applies. (See fig. 16 for references). (approx. X140).

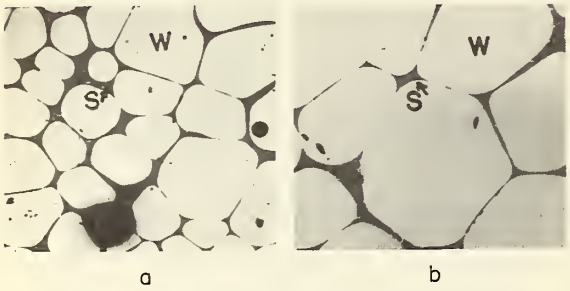

FIGURE 21. Grain Growth in polyphase microstructures. Example: Wüstite (FeO) growth in an iron oxide saturated silicate liquid (approx. X84). (a) Four hours at 1200°C (2190°F). (b) 64 hours at 1200°C [19]. W - wüstite; S - silicate liquid.

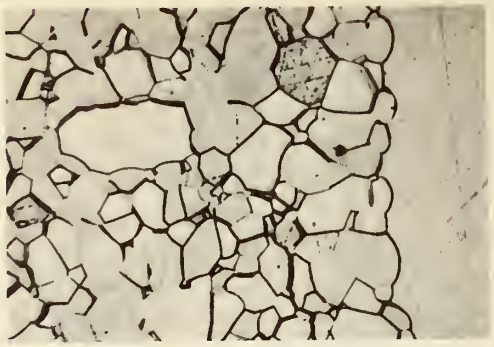

FIGURE 18. Abnormal grain growth. Example: corundum (Al_2O_3) heated to 1900 °C (X281).
(courtesy R. L. Coble.)

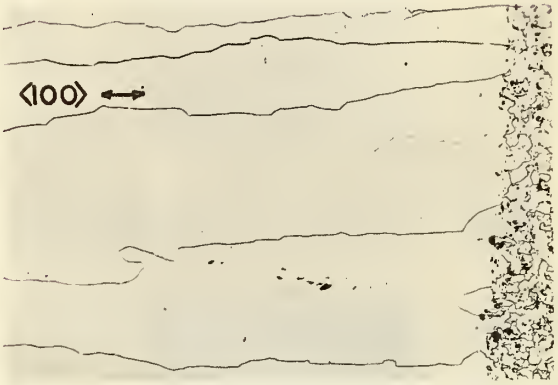

FIGURE 20. Grain elongation. Example: Uranium dioxide grains (approx. X42). The UO_2 had been melted and then solidified within a temperature gradient. [J. R. MacEwan and V. B. Lawson, "Grain Growth in Sintered Uranium Dioxide: II, Columnar Grain Growth," J. Am. Ceram. Soc. 45, 42 (1962)].

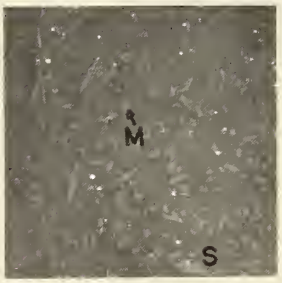

FIGURE 22. Grain shape (acicular). Example: mullite ($Al_6Si_2O_{13}$) in an alumino-silicate glass (X281). Most crystals of mullite are seen in cross-section only, in this reflected light microsection. The elongation is observed in the few which are aligned parallel to the surface. M - mullite; S - silicate glass.

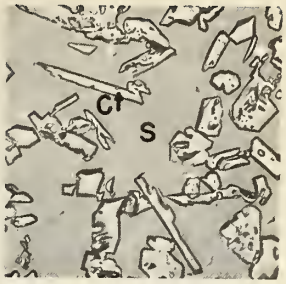

FIGURE 23. Grain shape (plates). Example: corundum (Al_2O_3) in an alumina-saturated silicate glass (X281). The elongated shapes are cross-sections of the plate. Those plates which lie parallel to the surface are nearly equidimensional in the microsection. C - corundum; S - silicate glass.

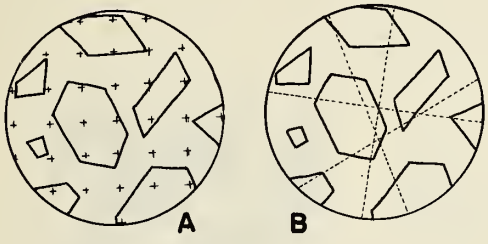

FIGURE 24. Volume analyses. (A) Point analysis. (B) Linear analysis. The probability that a point or a line falls within a phase in a microsection is equal to the volume fraction which is present.

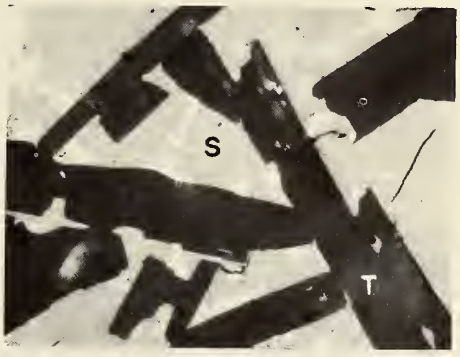

FIGURE 25. Euhedral growth. Example: tridymite (SiO_2) in a silica-saturated iron oxide liquid (X169). In many situations the rate of growth is sensitive to crystal direction. T - tridymite; S - silicate glass.

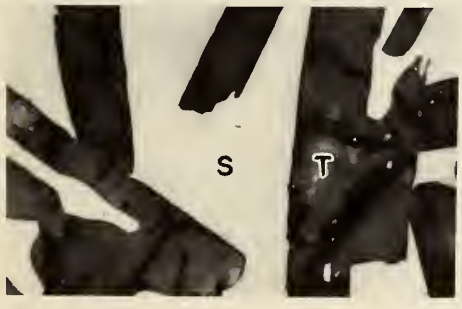

FIGURE 26. Anhedralization. Example: tridymite (SiO_2) in a silica-saturated iron oxide liquid (X169). With time at the equilibrating temperature, the surface area is minimized. (Cf. fig. 25.) T - tridymite; S - silicate glass.

FIGURE 27. Grain separation. Example: periclase (MgO) and an MgO-saturated calcium silicate liquid (approx. X140). Although less than 10 percent liquid is present, it allows only a negligible quantity of solid-to-solid contact (Cf. fig. 28, fig. 2c, and fig. 11b.) [21] P - periclase; S - silicate liquid.

FIGURE 28. Solid contact. Example: cristobalite (SiO_2) and a silica-saturated iron oxide liquid (X169). Although more than 25 percent liquid is present, a large dihedral angle (fig. 11b) provides solid-to-solid contact and structural rigidity at high temperatures. (Cf. fig. 27 and fig. 2b.) C - cristobalite; L - silicate glass.

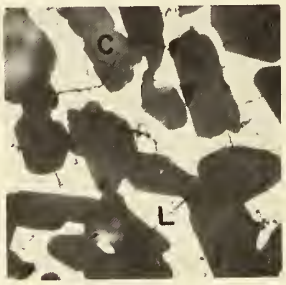

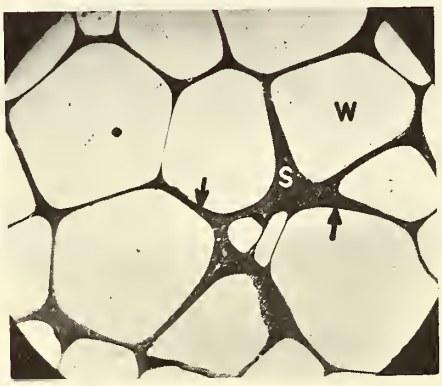

FIGURE 29. Microstructural-controlled behavior. Example: wüstite (FeO) and a silicate matrix. This matrix was liquid at the equilibrating temperature and subsequently has crystallized to fayalite (Fe_2SiO_4) and more wüstite (approx. X84). The crack is in the silicate matrix, but is closely associated with the silicate-wüstite boundary. W - wüstite; S - silicate liquid; Arrow - crack.

Experimental Techniques for Microstructure Investigation

V. D. Frechette

1. Introduction

The study of microstructures is concerned essentially with the ability to distinguish between materials having different chemical composition, structure or orientation and to distinguish between details separated by only small distances. Techniques for revealing microstructural features are almost all based either on the action of their details on incident radiation or on the quality and intensity of the radiation emitted by them when appropriately excited. Working treatments of the principles governing the resolution of microscopic details are available in standard works [1-4] and only the briefest review will be given here in order to identify the effects involved.

When a homogeneous object is viewed in transmission, i.e. by means of radiation transmitted through it, details corresponding to greater thickness may be revealed by their greater absorption as dark regions in the image. At constant thickness, details having greater absorption coefficients also yield darker images and, if the absorptions differ sufficiently for different light wavelengths, they may yield image color differences also.

Refraction effects at a boundary between grains may change the light path, thereby darkening the corresponding region of the image and brightening adjacent regions. The effect is intensified when the object is slightly out of focus and when the illuminating aperture is restricted. Boundaries may also be revealed by the scattering of light which takes place there to an extent which depends on the ratio of the refractive indices of the bordering phases. With illumination of the bright field type, i.e., when the light in the absence of any object in its path illuminates the entire field of view, the boundary layer shows up in the image as a darkening because the light is scattered by it and is lost to the true image. Under dark field conditions, in which illumination is arranged to just miss the field of view in the absence of an object in its path, scattering provides a mechanism by which details are rendered luminous and they form a bright image in a dark field.

Polarization-interference effects, which occur when an object is examined between crossed nicols or other polarizing elements with or without the aid of accessories, may be extremely valuable and the subject has been treated in numerous works [5-7]. Crystalline solids, except those of the cubic system, and stressed solids of any structure split plane-polarized light into two rays vibrating perpendicular to one another which travel along essentially the same path but with different velocities. During passage through a mineral grain one of these is retarded behind the other owing to its slower velocity; when the two rays emerge from the mineral and pass through the analysing nicol prism they interfere to an extent determined by that retardation and by the wave length of the light. Under crossed nicols, therefore, a mineral grain displays colors, corresponding to retardation, which are determined by the thickness of the grain and by its effective birefringence (birefringence is the difference between the refractive indices of the two rays) for the orientation in which it lies. Not only may grains be distinguished from one another by this process but their identity and their orientation may be inferred, particularly with the aid of interference figures formed in the back opening of the objective lens under strongly converging transmitted light.

In reflected light, details may be distinguished through operation of all of the above effects [8]. In addition differences in reflecting power characterize those materials whose refractive indices differ sufficiently as indicated by Fresnel's formula, stated for normal incidence:

$$R = \left[\frac{N-1}{N+1}\right]^2$$

where R is the fractional amount of light reflected and N is the refractive index.

Under both transmission and reflection conditions, the light beam passing through the grain or being reflected from its surface is retarded somewhat behind those light rays which pass around it, or encounter materials of other refractive index. In the phase contrast microscope [9] an annular diaphragm is inserted in the condenser, while a second annular plate is set at the conjugate plane of the condenser ring, to introduce an additional small phase shift. Interference between these two in the image plane provides sharp contrast between details which vary only very slightly from their surroundings. The phenomenon of interference is applied also in the so called interference microscope [10-19] for the determination of surface contours. In the simplest arrangement of this type the light rays reflected downward by a semi-silvered mirror are partly reflected by an optically flat plate, while those which are transmitted through the plate are reflected from the surface of the specimen. These two are tipped slightly with respect to one another so that there is seen in the field of view, for a perfectly flat specimen, a series of parallel bright lines, or interference fringes. Each bright line is the locus of those points on the specimen surface which are at a constant distance from the optical flat, this distance being precisely an odd number of half wave lengths of the light employed. Consequently any excursion of the specimen contour from the plane of its surroundings results in a displacement of the fringes. The test is an extremely sensitive one and make possible surface contouring of a specimen to within a small fraction of the wavelength of light, i.e., to about a hundredth of a micron, although lateral resolution is still confined to the usual limit of the lens system or about 0.2 microns for visible light.

2. Optical Microscopy

A tremendous increase in the use of the optical microscope on ceramics [20-24] and other materials in recent years has acted as a spur to and has itself been accelerated by the development of instruments and accessories [3,25] . Most notable are the new microscopes of the universal type featuring permanently aligned illuminators of high intensity and stable operation, conveniently mounted apparatus for photography including automated cameras for films, plates and Polaroid, and rapidly-interchangeable accessories for bright- and dark-field examination in transmitted and reflected light with the option of phase contrast and interferometric optics. A growing list of polarizing accessories extends the range of optical measurements that can be made and new mechanical devices facilitate particle size measurement and quantitative analysis. Inclined binocular eyepieces reduce operator fatigue to negligible proportions and high eyepoint eyepieces permit spectacles to be worn without sacrificing breadth of visible field, an advantage to observers having pronounced astigmatism. At lower magnifications zoom-type optics contribute significantly to speed and convenience.

The limit of resolution of the microscope is approximately 0.6λ /N.A. where is the wavelength of the light used and N.A. is numerical aperture of the λ illumination and objective lenses. For visible light this is approximately 0.2 microns. Ultraviolet light microscopy using photographic registration of the (invisible) image extends the resolution by a factor of two but at great loss of convenience.

3. Electron Microscopy

Very much shorter wavelengths (about.015 millimicrons) are associated with a beam of electrons. The electron microscope [26-37] uses an incandescent filament as a source of electrons, accelerates them to high velocity by means of an electric field, and focuses them with magnetic or electrostatic lenses in much the same way as an optical microscope focuses light beams. In practice it is particularly distinguished from the optical microscope by the very poor penetrating power of the electron beam, which limits the object to extremely thin sections unless a reflecting technique is to be employed. It is significant that the effectiveness of the electron microscope has grown directly in proportion to the development of methods of specimen preparation and particularly the replica techniques. Useful magnifications up to about 2×10^5 are routinely employed,(although most work is under 2×10^4) and under special conditions dislocations themselves may be directly observed by it through diffraction effects [38,39]. While the optical crystallography of materials, based on refractive indices and polarization effects, does not apply in the electron microscope, many instruments are provided with means for obtaining electron diffraction patterns of individual grains located in its field and thus phase identification and orientation may be studied.

The poor quality of reflected electron images has been overcome in an ingenious way in the scanning electron microscope[31]. In this instrument the electron beam is brought to a fine focus on a very small region of the sample and the scattered electrons are picked up in a fixed detector whose signal is fed to a cathode ray oscilloscope. The beam is swept across the surface of the sample in synchronization with the sweep of the oscilloscope which accordingly traces an image of the specimen whose brightness corresponds to the atomic number and density of atoms in the specimen components. Useful magnification by this method is not great and does not exceed that of the optical microscope. The depth of focus, however, is very much greater than that of the optical microscope at corresponding magnification, and excellent photographs of fracture surfaces of aluminum oxide have been obtained with it[40].

3. Electron Probe X-Ray Analysis

The high speed electrons of the electron microscope impinging on the sample excite the atoms to emit X-rays. These X-rays may be analyzed with respect to wavelength and intensity to yield spectra from which the constituent elements may be identified both qualitively and quantitatively. If the electron beam is confined to a very small area of the sample, a few square microns, complete chemical analysis of the small area may be obtained, excepting only those elements under atomic number eleven, whose emitted X-rays are so long in wavelength that they are easily lost. If the electron beam is swept across the surface while the X-ray detector is set to record a wavelength characteristic of a particular element, a plot may be obtained on an oscilloscope sweeping in syncronization with the electron beam; brightness in the oscilloscope image corresponds to points in the specimen where the element is to be found in abundance. Instruments of this kind are termed electron probes or electron micro-probe X-ray analyzers [41]. While few of these have seen application on ceramic materials up to the present, a few studies show the method to be effective and highly promising[42,43]. Indeed the application of the electron probe to problems of ion species segregation in polycrystalline materials is one of the most exciting on the present scene.

4. Emission Microscopes

Professor Castaing has suggested another way of imaging the specimen surface. If it is bombarded with a beam of ions of appropriate energy, it may be excited to give off secondary ions which may be focused with electro-magnetic lenses, passed through a mass spectrometer set to select a particular ion species, and brought to focus on an image converter which releases electrons to be focused in turn on a photographic plate.

Other emission type microscopes have been developed[29,34]and have been extremely successful with certain metals, but their use with ceramic materials has been limited[44].

5. Microradiography and X-ray Microscopy

Specimens containing radioactive elements may be photographed by simply pressing them against the photographic emulsion for an extended period of time. The resulting autoradiograph is not usually sharp enough to permit much magnification but it is a valuable technique for indicating concentration gradients as in the case of experiments on diffusion and especially self-diffusion. Cyclotron activation techniques extend the method to include a wide variety of elements and it should prove useful in specialized structural studies.

The use of X-rays to disclose structural features is well known. When the X-ray source is very small the radiograph attains high resolution [45]; in theory it is that of the electron microscope but practical difficulties are formidable and it is limited in the present state of development to the limit of the optical microscope[46]and little work is done beyond 100X. Except in particularly favorable cases good contrast in the image is difficult to obtain [47]. Neutron microradiography [48-50] seems to be a promising alternative, since the light elements which are so frequently of interest in ceramic problems are extremely opaque to thermal neutrons.

Two principal techniques are in use. Contact microradiography consists in obtaining the image by radiography in which the specimen is in contact with a photographic plate and enlarging it photographically. In point projection X-ray microscopy the specimen is some distance away from the plate so that it casts an enlarged shadow upon it.

The above are by no means the only methods for obtaining highly resolved images of a specimen, but they represent those whose present state of development seems to offer most promise for use on ceramic materials. It is especially significant that the vastly increased knowledge of the microstructure of ceramics which has come during the past decade has been accompanied and has been largely the result of greatly improved techniques in the preparation of specimens for examination.

Thin sections of specimens, fine-ground to flatness, cemented on a glass slide, and ground down to a thickness of 30 microns, more or less, [20,21] are suitable for the examination of course-grained materials, using the transmission optical microscope. With the aid of polarized light accessories these are capable of yielding structural information including grain orientation by the petrographic methods (petrofabric analysis) originated in connection with petrological problems [51]. For fine grained materials the thickness of these sections implies the overlapping of a number of grains in the image so that information concerning both detail and orientation are lost. Recently a method for making very much thinner sections has been suggested [52,53] . A shallow well is etched with hydrofluoric acid in the surface of the microscope slide. The specimen cemented in the bottom of this well is protected by the glass down to the last stages of finish grinding, so that sections 6 microns in thickness can be produced with care. The technique restores the thin section to an extremely useful place in the microscopy of ceramic materials. At the same time the ultra-microtome [54-57]employing a diamond knife, has been used successfully to get sections thin enough for direct electron microscopy although they are small in area.

Splinters and chips of materials can be produced easily by simply crushing materials under proper conditions and these have given results in optical and electron microscopy [58] . In the case of porcelain enamels this may involve only bending the specimen in the direction of the enameled surface. Thin scales may be pulled from surfaces by applying a concentrated gelatine solution or certain glues and drying in an oven.

Specimens for direct transmission electron microscopy may be prepared by special fabrication and heat treatment. Glasses and enamels have been prepared by blowing very thin bubbles followed by etching [59]. Sinterable materials may be prepared by sintering a little of the very fine powdered material on a metal grid [60].

Polished sections, while yielding meager optical information, offer strong advantages in quantitative studies, since they represent a single plane through the specimen and so yield textural information with less quantitative ambiguity. Distinction between the phases rests less on the optical properties of the phases themselves, and more on particular treatments to which some of the constituents of the specimen are more susceptible than others. On the one hand, this involves attack by chemical or physical agents, while on the other hand, it may involve the receptivity of certain details to decoration. The problem of preparing an initially flat polished surface has largely been solved with the advent of impregnation techniques to fill pores and diamond dust as the polishing medium, either fixed in rotating laps or used as a paste on an appropriate surface [21] . In every case, however, there is a certain art in the choice of the backing surface, the lubricant, polishing speed, pressure, and time [61-65].

In order to enhance the contrast between grains in a specimen, to distinguish phases from one another, and to reveal internal structure in the grains themselves, such as dislocations, an etch is usually helpful A variety of procedures are in use as the partial list in Table 1 indicates. The superb results obtained with portland cement clinkers and basic refractories [21] and with metallurgical slags [103] in differentiating between constituents of complex mixtures is a spur to more persistent efforts. An almost complete lack of discussion of the reasons for the selection of procedures lead to the suspicion that very much is still to be learned on this subject. It would be surprising if there are not far more effective etching proceedures still to be found. In the face of the difficulty of choosing an appropriate specific chemical etch, there is of course a hope for a universal etchant. Three are claimed in the field of ceramics. Thermal etching, i.e., raising the temperature of the polished specimen in a furnace with an oxy-acetlyne torch or in an arc image, has been found successful in bringing out grain boundaries in many cases. Examples are given in Table 2, which includes also examples of the relief polish and ion bombardment techniques.

Table 1. Some Chemical Etchants for Ceramics

Material and Reagent	Conditions	Comments	Reference
Aluminum Oxide			
85% H_3PO_4	Boiling 5-10 min.		Houle [62]
H_3PO_4 conc.	Boiling 4 min.		Gardner [63]
	210°C. 11-16 min.		Warshaw [66]
	425°C. 120-180 sec.	Polish (0001)	Alford [67]
$KHSO_4$	Melt 3-15 sec.		Houle [62]
	675°C. 15-20 sec.	Etch (000$\bar{1}$)	Alford [67]
	675°C. 135 sec.	Etch (11$\bar{2}$0)	Alford [67]
$K_2S_2O_7$	300°C. 3 min.		Warshaw [66]
H_2SO_4	200°C. 20 min. to 270°C. 5 min.		McVickers [64]
K_3AlF_6	1000°C. 30-60 sec.	Polish (11$\bar{2}$0)	Alford [67]
Dry H_2	1700°C. 1-2 min.		Houle [62]
Barium Ferrite			
5% HCl	20 sec.	$Ba_2Fe_2O_5$-$BaBe_2O_4$	Goto [68]
HCl		$BaFe_2O_4$-$BaFe_{12}O_{19}$	Goto [68]
Barium Titanate			
Few drops HF in 5 ml. HCl, 95 ml. H_2O	1-7 min		Kulcsar [69]
HF-HNO_3-H_2O	During polishing		DeVries [70]
0.5%HF in HNO_3	1½ min.		Tennery [71]
1% HF			DeVries [72]
85% H_3PO_4	100°C. 1 hr.	Etched pos.,neg. ends differentially	Belitz [73]
Beryllium Oxide			
HF (48%)	10 sec. - 5 min.		Houle [62]
Calcium Fluoride			
20% HCl	near boiling 5-10 sec.		Burn [74]
50% HCl	boiling 5 min.	to polish	Burn [74]
2% sulfamic acid in water	40-50 min.		Phillips [75]
Calcium Fluoride - Sodium Fluoride			
H_2SO_4			Kingery [76]
Calcium Oxide			
4% picric acid in methyl alcohol			Daniels [77]
Cadmium Manganese Ferrite			
HF (48%)	10 sec. - 2 min.		Eichbaum [78]
Cadmium Niobate			
HF			de Bretteville [79]
Carbon(Diamond)			Frank [80]
O_2	Hot		Gualtieri [81]
Chromium Sesquioxide			
$KHSO_4$	melt 3-15 sec.		Houle [62]
Glasses			
0.05% HF	2 min.	Titama-opacified enamel	Yee [59]
Acetic Acid		$Na_2O.2SiO_2$	Parikh [82]
HF (dilute)		To bring out cracks from microindenter	Argon [83]
NH_4F (sat'd sol'n) + NH_4HF_2	Several hours	Lithia glass	Jaccodini [84]
24% HF	15 sec.	Lithium silicate	Rindone [85]
Lead Titanate Zirconate			
Few drops HF in 100 ml. 5% HCl			Kulcsar [69]

Table 1. Some Chemical Etchants for Ceramics (Cont'd)

Material and Reagent	Conditions	Comments	Reference	
Lithium Fluoride				
2×10^{-4} mol % FeF_3 in H_2O	1 min.		Gilman	[86]
Magnesium Ferrite				
$SnCl_2$-HCl			Carter	[87]
Magnesium Oxide				
30% HCl, 10% sat'd sol'n of NH_4Cl, 60% water	5-20 min.		Gorum	[88]
HNO_3 in H_2O 1:1	1-5 min		Houle	[62]
H_2SO_4 (dilute)			Daniels	[77]
H_3PO_4 (Dilute)			Daniels	[77]
Magnesium - Manganese Ferrites (Thermal etch)			Palmer	[89]
Mullite - Glass				
10% HF	3 sec.		Studt	[90]
Porcelain				
HF			Lundin	[91]
Plutonium-Carbon System				
Acetic acid-HNO_3-H_2O, equal parts	80 ma./cm^2 30 sec. (electrolytic etch)		Kruger	[92]
Plutonium Monocarbide				
H_2O			Lied	[93]
Strontium Titanate				
5 parts HF, 10 parts HNO_3, 10 parts H_2O	8 min.		Waugh	[94]
Titanium Carbide-Molybdenum				
Alkaline Ferricyanide			Parikh	[83]
Titanium Carbide-Nickel				
Alkaline Ferricyanide			Parikh	[83]
Titanium Dioxide (Rutile)				
KOH	400°C. 20 min.		Hirthe	[96]
85% H_3PO_4	Boiling 2½-3 min.		Hirthe	[96]
H_2SO_4	hot 10-30 min.(preferred)		Hirthe	[96]
Tungsten Carbide-Cobalt				
Alkaline Ferricyanide			Parikh	[82,95]
Tungsten Carbide-Copper				
Alkaline Ferricyanide			Parikh	[82,95]
Uranium - Uranium Nitride (Electrolytic)			Accary	[97]
Uranium Carbide-Plutonium Carbide				
HNO_3			Lied	[93]
Uranium Dioxide				
HNO_3: Water 1:1	1-5 min.		Houle	[62]
30% H_2O_2 - 9 Parts				
H_2SO_4 - 1 Part			Fuhrman	[98]
Uranium Dioxide - Lanthanum Oxide				
H_3PO_4	Boiling		Hill	[99]
Uranium Sulfide				
10% H_2SO_4			Shalek	[100]
Yttrium Iron Garnet				
HCl	Boiling 1 hr.		Rudness	[101]
HCl	4½ hr.		Lefever	[102]
20% HCl	2½ hr.		Lefever	[102]
Zirconium Dioxide				
HF (48%)	1-5 min.		Houle	[62]

Table 2. Universal Etch Techniques

Material and Technique	Conditions	Comments	Reference	
RELIEF POLISH				
Aluminum Oxide	0.1 micron Al_2O_3 on Microcloth		Angelides	[104]
Glass-metal Seals	0.2 micron Al_2O_3		Cole	[105]
THERMAL ETCH				
Aluminum Oxide	1700°C. in dry H_2 1-2 min. 1900°C. oxyacetylene torch 2-5 sec.		Beauchamp	[106]
Uranium Dioxide-Lanthanum Oxide	Incipient fusion in arc image furnace		Evans	[107]
ION BOMBARDMENT				
Aluminum Oxide			Bierlein	[108]
Porcelain			Bierlein	[108]
Uranium oxide			Bierlein	[108]
Aluminum - aluminum oxide			Bierlein	[108]
Titanium carbide - nickel			Bierlein	[108]
Cobalt silicide - titanium carbide			Bierlein	[108]
Titanium diboride			Bierlein	[108]
PUO_2 - UO_2			Keig	[109]
Pyrolytic graphite			Coy	[110]

Thermal etching may develop surface detail by at least three processes [111] . It may involve transfer of material by surface diffusion from high surface energy to low surface energy regions and,therefore, away from grain boundaries. It may involve loss of material by sublimation, and it may involve evaporation-condensation, developing growth figures.

Relief polishing, involving a polishing step with a softer abrasive, develops a surface relief indicative of the abrasion resistance of the constituents at the surface. Like the chemical etch, this is sensitive to grain orientation as well as to the differences in hardness among phases and at grain boundaries.

Ion bombardment of the polished specimen surface is also promising as a universal etch [108] . The specimen is placed in a chamber evacuated to 30-50 microns krypton pressure and is made the cathode with respect to a potential drop of about 4000 volts across the chamber. Exceptionally fine etches have been obtained on a variety of materials by this method, but experimentation is necessary in every case to find the appropriate gas pressure, voltage, and time for best results.

The decorating of surfaces before or after an etching treatment has not been sufficiently explored. Important results with decoration by sodium vapor to reveal cracks in glasses [112, 113] , decoration of sodium chloride with gold particles [114] resulting from the decomposition of gold chloride, decoration of magnetic materials with Fe_2O_3 and the use of small charged particles in crack location and polarity determinations [115, 116] all suggest that decoration is well worth exploring further.

The study of fracture-exposed surfaces [117-120] to disclose fracture origins, grain orientation through cleavage traces and negative crystals and the path of fracture, whether through grain boundaries or through the grains themselves, has proved rewarding and shows great usefulness in connection with materials testing, trouble shooting of fabrication problems and service failures,as well as micro-structural details on which recent revisions of glass atomic arrangement have been partly based [127-132] .

7. Replication

In order to preserve the advantages of the polished section or fracture surface without the difficulty of reflecting type instruments the surface in question may be replicated as a thin film which preserves its topographical details. The process may be as simple as the technique of pressing a plastic tape, softened with an appropriate solvent,against the surface and stripping if off [133] . The result is a negative replica, i.e., high points in the sample correspond to hollows in the replica. This method has been valuable in examing surface damage in enamels with the optical microscope [134] . The replicating process for electron microscopy usually involves several stages [21, 26, 28; 135-150] . The high resolution technique of Bradley [136] will serve as an example. A film of Formvar is first coated on the specimen as a 1 or 2% solution in chloroform. This is backed with a 7% solution of a soluble resin, Bedacryl, in benzene. The replica is then stripped from the surface. In vacuum carbon is coated on the surface from a carbon arc. The Bedacryl backing resin is then dissolved with acetone and the Formar removed with chloroform. The film is then ready for examination.

To enhance contrast in such replicas and to provide a relief effect giving three dimensional information, the replicas are generally shadowed by evaporation of a metal such as platinum, palladium, gold or chromium at a glancing angle so that the metal accumulates on the near side of positive details, while the far sides are sheltered. The appearance of such shadowed replicas in the electron microscope gives the impression of illumination at a glancing angle and throws details into strong relief.

8. Conclusion

Of the many instruments and techniques discussed, none should be considered "best" but each has its own particular applications. Most dangerous of all would be the temptation to rely on one technique alone, for each has its "blind spots" and areas of confusion where spurious effects can lead to error. Most problems profit from complementary observations with two or more methods and in almost every case optical microscopy, not neglecting the stereoscopic microscope at lower magnifications, should be one of these.

References

1 M. Françon, Progress in Microscopy, Row, Peterson & Co. (Evanston, Ill., 1961).

2 E. M. Chamot and C. W. Mason, Handbook of Chemical Microscopy Vol. I, John Wiley & Sons (New York, 3rd ed., 1958).

3 Handbuch der Mikroskopie in der Technik, Hugo Freund, ed., Umschau Verlag (Frankfurt/Main) Band I Die Optischen Grundlagen die Instrumente und Nebenapparate für die Mikroskopie in der Technik. Teil I Durchlichtmikroskopie(1957;)Teil II Auflichtmikroskopie(1960).

4 Encyclopedia of Microscopy,G.L. Clark,ed., Reinhold (New York, 1961).

5 E.E. Wahlstrom, Optical Crystallography, John Wiley & Sons (New York, 3rd ed., 1960).

6 F. Donald Bloss, An Introduction to the Methods of Optical Crystallography, Holt, Rinehart and Winston (New York, 1961).

7 F. Rinne and M. Berek, Anleitung zu optischen Untersuchungen mit dem Polarisationsmikroskop, E. Schweizerbartsche Verlagsbuchhandlung (Stuttgart, 1953).

8 E. N. Cameron, "The Study of Opaque Minerals in Reflected Light" in Symposium on Microscopy, ASTM Special Tech. Pub. No. 257 (1959) pp. 39-75.

9 A.H. Bennett, H. Jupnik, H, Osterberg and O. W. Richards, Phase Microscopy: Principles and Applications, John Wiley & Sons (New York, 1951).

10 S. Tolansky, Multiple Beam Interferometry of Surfaces and Films, Clarendon Press (Oxford, 1948).

11 S. Tolansky and M. Omar, "Thin Film Interferometric Techniques for High Magnification" Topographical Studies, Nature 170,81-82 (1952).

12 J. B. Wachtman, Jr. and L. H. Maxwell, "Plastic Deformation of Ceramic Oxide Single Crystals II" J. Am. Ceram. Soc. 40, 377-85 (1957).

13 Guy Erwin, Jr. "Oxidation Behavior of Silicon Carbide" J. Am. Ceram. Soc. 41, 347-52 (1958).

14 F. M. Ernsberger, "Attack of Glass by Chelating Agents" J.Am.Ceram.Soc. 42, 373-75 (1959).

15 O.W. Richards, "Measurement with Phase and Interference Microscopy" in ASTM Special Tech. Pub. No. 257 (1959) pp. 6-18.

16 S. Tolansky, Surface Microtopography Longmans, Green & Co. (London, 1960).

17 Louis Navias, "Preparation and Properties of Spinel Made by Vapor Transport and Diffusion in the System $MgO-Al_2O_3$" J. Am. Ceram. Soc. 44, 434-46 (1961).

18 S.S. Kistler, "Stresses in Glass Produced by Nonuniform Exchange of Monovalent Ions" J. Am. Ceram. Soc. 45, 59-68 (1962).

19 Eugene W. Sucov, "Elastic Stresses Produced by Indentation of Plane Surface of a Semi-infinite Elastic Solid by an Elastic Spherical Punch" J. Am. Ceram. Soc. 45, 575-579 (1962).

20 G. R. Rigby, Thin-Section Mineralogy of Ceramic Materials, British Ceramic Research Association (Stoke-on-Trent, 2nd ed., 1953).

21 H. Insley and V.D. Frechette, Microscopy of Ceramics and Cements Academic Press (New York, 1955).

22 D.S. Beljankin, B.W. Ivanow and W.W. Lipin, Technische Petrographie VEB Verlag Technik (Berlin, 1960).

23 Symposium on Light Microscopy, ASTM Spec. Pub. No. 143 (1953).

24 W. D. Kingery, Introduction to Ceramics, John Wiley & Sons (New York, 1960) pp. 402-458.

25 W. C. McCrone, Light Microscopy Ind. Research (June 1963), pp.43-46.

26 V.K. Zworykin, G. A. Morton, E. G. Ramberg, J. Hillier and A. W. Vance, Electron Optics and the Electron Microscope John Wiley & Sons Inc. (New York, 1945).

27 E. F. Burton and W. H. Kohl, The Electron Microscope, Reinhold (New York, 2nd ed., 1946).

28 Ralph W. G. Wyckoff, Electron Microscopy Techniques and Applications, Interscience Publishers, Inc. (New York, 1949)

29 C.E. Hall, Introduction to Electron Microscopy, McGraw-Hill Book Co., Inc.(New York, 1953).

30 Robert B. Fischer, Applied Electron Microscopy, Indiana Univ. Press (Bloomington, Indiana, 1954).

31 Ralph W.G. Wyckoff, The World of the Electron Microscope, Yale Univ. Press (New Haven, 1958).

32 J. J. Comer, "Electron Microscope in the Study of Minerals and Ceramics" in Symposium on Microscopy, ASTM Special Tech. Pub. No. 257 (1959) 94-120.

33 International Bibliography of Electron Microscopy Vol. I 1950-1955, K. T. Morse and Dan H. Moore editors (1959) Vol. II 1956-61, Dan H. Moore editor (1962) New York Soc. of Electron Microscopists (New York).

34 Claude Magnan, Traite de Microscopie Electronique (2 volumes) Hermann (Paris, 1961).

35 S. N. Ruddlesden, "Application of the Electron Microscope to Ceramics" in Science of Ceramics Vol. I, G. H. Stewart, ed., Academic Press (New York, 1962), p. 107.

36 M. J. Whelan, "Outline of the Theory of Diffraction Contrast Observed at Dislocations and Other Defects in Thin Crystals Examined by Transmission Electron Microscopy", J. Inst. Metals 87, 392-405 (1958-59).

37 D. Kay, ed., Techniques for Electron Microscopy Blackwell (Oxford, 1961).

38 Direct Observation of Imperfections in Crystals, J. B. Newkirk and J. H. Wernick, editors, Interscience (New York, 1962).

39 H.G.G. Wilsdorf, "Observations of Dislocations" in Mechanical Behavior of Crystalline Solids, Nat. Bur. Stds. Monograph 59 (1963) 35-62.

40 R.F.M. Thornley and L. Cartz, "Direct Examination of Ceramic Surfaces with the Scanning Electron Microscope", J. Am. Ceram. Soc. 45, 425-28 (1962).

41 L. S. Birks "The Electron Probe: An Added Dimension in Chemical Analysis" Anal. Chem. 32, 19A (1960).

42 W. F. Ford, A. Hayhurst and J. White, "Effect of Bond Structure on the High Temperature Tensile Behaviour of Basic Bricks" Trans. Brit. Ceram. Soc. 60, 581-601 (1961).

43 B. R. Eichbaum, "Effect of Boron on Square-Loop Cadmium Manganese Ferrites", J. Am. Ceram. Soc. 44, 51-54 (1961).

44 L. Cartz, G. Mollendtedt and A. Septier, "Emission Electron Microscope Studies of Ceramic Materials", Trans. 8th Ceram. Congr. (1962) 21.

45 V. E. Cosslett, A. Engstrom, H. H. Pattee, Jr., X-ray Microscopy and Microradiography, Academic Press (New York, 1957).

46 V. E. Cosslett, "Comparison of the Practical Limits of X-ray and Electron Microscopy", Proceedings of the Third International Conference on Electron Microscopy, London, 1954. V. E. Cosslett and R. Ross, editors, Royal Microscopical Society (London, 1956) 311-17.

47 J. Schmitt, "Application of Contact Microradiography by Means of Fluorescent Radiation" 88-99; Verres et Refract. 16, 11-19; 88-99; 168-174 (1962).

48 H. Kallmann, "Neutron Radiography" Research 1, 254-60 (1948).

49 J. Thewlis, "Neutron Radiography" British J. App. Physics 1, 345-50 (1956).

50 H. Berger, "Neutron Radiography" Scientific American Vol. 207, (November 1962) p. 107.

51 E. E. Wahlstrom, Petrographic Mineralogy, John Wiley & Sons, Inc. (New York, 1955).

52 J. S. Kahn, N. Houlding and A. Regoli, "Method of Preparing Thin Sections of Fine-Grained Materials" J. Am. Ceram. Soc. 45, 50 (1962).

53 C. B. Clark, "Laboratory Investigation of Glass Defects. Part II. Methods for Preparing Sections" Harbison-Carborundum Report, (1963).

54 G. Pfefferkorn and H. Urban, "Elektronmikroskopische Mikrotomschnittuntersuchungen als Kontrollmöglichkeit bei Röntgenographischen Texturaufnahmen" Naturwiss. 43, 513 (1956).

55 G. Pfefferkorn, H. Theman and H. Urban, "Anwendungen der Mikrotomschnitt-Technik auf Elektronmikroskopische Mineraluntersuchungen" Proceedings of the Stockholm Conference on Electron Microscopy, F. S. Sjostrand and J. Rhodin, editors, Almquist and Wiksell (Stockholm, 1957) p. 333

56 S. Kienow, G. Pfefferkorn and H. Urban, "Elektronmikroskopische Untersuchungen an Ultramikrotomschnitten von Mullit mit Einlagerung von Eisenoxyden" Naturwiss. 47, 322 (1960).

57 G. Pfefferkorn, W. Ohnemüller and H. Urban, "Elekronmikroskopische Ultramikrotomischnitt Untersuchungen an Ziegeln", Naturwiss. 47, 332 (1960).

58 R. A. Lefever, A. B. Chase and Juanita W. Torpy, "Characteristic Imperfections in Flux Grown Crystals of Yttrium Iron Garnet", J. Am. Ceram. Soc. 44,141-44 (1961).

59 Tin Boo Yee and A. I. Andrews, "The Relation of Viscosity, Nuclei Formation and Crystal Growth in Titania-opacified Enamel", J. Am. Ceram. Soc. 39, 188-95 (1952).

60 J. S. Kahn and J. B. Cahoon, Jr., "Thin Films of BeO and other Sinterable Materials", Univ. of Calif., Lawrence Radiation Lab. Report 7178, (1963)

61 M. N. Short, Microscopic Determination of the Ore Minerals U. S. Geol. Survey Bulletin 914, (1940).

62 M. C. Houle and R. L. Coble, "Ceramographic Techniques.I Single-Phase Polycrystalline Materials", General Electric Research Laboratory Report No. 61-RL-2898M (1961).

63 R. E. Gardner and G. W. Robinson, Jr., "Improved Method for Polishing Ultrahigh-Density MgO", J. Am. Ceram. Soc. 45,46 (1962).

64 R. C. McVickers, S. D. Ford, R. A. Dugdale, "Polishing and Etching Techniques for Dense Alumina", J. Am. Ceram. Soc. 45, 199 (1962).

65 G. M. Fryer and J. P. Roberts, "Some Techniques for Microscopical Examination of Ceramic Materials", Trans. Brit. Ceram. Soc. 62, 537-48 (1963).

66 Stanley I. Warshaw and Frederick H. Norton, "Deformation Behavior of Polycrystalline Aluminum Oxide" J. Am. Ceram. Soc. 45, 479-86 (1962).

67 W. J. Alford and D. L. Stephens, "Chemical Polishing and Etching Techniques for Al_2O_3 Single Crystals", J. Am. Ceram. Soc. 46, 193-194 (1963).

68 Y. Goto and Toshio Takada, "Phase Diagram of the System BaO-Fe_2O_3" J. Am. Ceram. Soc. 43,150-53 (1960).

69 Frank Kulcsar, "Electromechanical Properties of Lead Titanate Zirconate Ceramics Modified with Certain Three or Five Valent Additions", J. Am. Ceram. Soc. 42, 343-49 (1959).

70 R. C. DeVries and J. E. Burke, "Microstructure of Barium Titanate", J. Am. Ceram. Soc. 40, 200-206 (1957).

71 V. J. Tenney and F. R. Anderson, "Examination of the Surface and Domain Structure in Ceramic Barium Titanate", J. Appl. Phys. 29, 755-58 (1958).

72 R. C. DeVries,"Lowering of Curie Temperature of $BaTiO_3$ by Chemical Reduction", J. Am. Ceram. Soc. 43, 226 (1960).

73 R. K. Belitz, "Differential Etching of $BaTiO_3$ by H_3PO_4", J. Am. Ceram. Soc. 45, 617-618 (1962).

74 R. Burn and G. T. Murray, "Plasticity and Dislocation Etch Pits in CaF_2", J. Am. Ceram. Soc. 45, 251-2 (1962).

75 W. L. Phillips, Jr., "Deformation and Fracture Processes in Calcium Fluoride Single Crystals", J. Am. Ceram. Soc. 44, 499-506 (1961).

76 W. D. Kingery, E. Niki and M. D. Narasimhan, "Sintering of Oxide and Carbide-Metal Compositions in the Presence of a Liquid Phase", J. Am. Ceram. Soc. 44, 29-35 (1961).

77 A. U. Daniels Jr., R. C. Lowrie, R. L. Gibby and Ivan B. Cutler, "Observations on Normal Grain Growth of Magnesia and Calcia", J. Am. Ceram. Soc. 45,282-85 (1963).

78 B. R. Eichbaum, "Effect of Boron of Square-Loop Cadmium Manganese Ferrites", J. Am. Ceram. Soc. 44, 51-54 (1961).

79 A. de Bretteville, Jr., F. A. Halden, T. Vasilos and L. Reed, "Dielectric Studies in the System CdO-Nb_2O_5",J. Am. Ceram. Soc. 40, 86-89 (1957).

80 F. C. Frank et al, "Etch Pits and Trigons on Diamond", Phil. Mag. 3, 1262-79 (1958).

81 J. G. Gualtieri, M. J. Katz and G. A. Wolff, "Gas Etching and its Effect on Semiconductor Surfaces", Z.f.Krist. 114, 9-22 (1960).

82 N. M. Parikh and M. Humenik, "Cermets: II Wettability and Microstructure Studies in Liquid Phase Sintering", J. Am. Ceram. Soc. 40,315-20 (1957)

83 A. S. Argon, Y. Hori and E. Orowan, "Indentation Strength of Glass", J. Am. Ceram. Soc. 43, 86-96 (1960).

84 R. J. Jaccodini, "Study of Devitrification of Lithium Glass", J. Am. Ceram. Soc. 44, 472-75 (1961).

85 G. E. Rindone, "Further Studies of Crystallization of a Lithium Silicate Glass", J. Am. Ceram. Soc. 45, 7-12 (1962).

86 J. J. Gilman, W. G. Johnston and G. W. Sears, "Dislocation Etch Pit Formation in Lithium Fluoride", J. Appl. Phys. 29, 747-54 (1958).

87 R. E. Carter, "Effect of Oxygen Pressure on Microstructure and Coercive Force of Magnesium Ferrite", J. Am. Ceram. Soc. 41, 545-50 (1958).

88 A. E. Gorum, W. J. Luhman and J. A. Pask, "Effect of Impurities and Heat Treatment on Ductility of MgO", J. Am. Ceram. Soc. 43, 241-45 (1960)

89 G. G. Palmer, R. W. Johnston, and R. E. Schultz, "Magnetic Properties and Associated Microstructure of Zinc-Bearing Square-Loop Ferrites", J. Am. Ceram. Soc. 40, 256-62, (1957).

90 Perry L. Studt and Richard M. Fulrath, "Mechanical Properties and Chemical Reactivity in Mullite Glass Systems", J. Am. Ceram. Soc. 45, 182-88 (1962).

91 S. T. Lundin, Studies on Triaxial Whiteware Bodies, Almquist & Wiksell (Stockholm, 1959).

92 Owen L. Kruger, "Phase Studies on Arc-Melted Plutonium Carbon Alloys Near the Monocarbide Composition", J. Am. Ceram. Soc. 46, 80-85 (1963).

93 R. C. Lied and G. D. White, "Preliminary Studies in the System UC-PuC", J. Am. Ceram. Soc. 45, 148-151 (1962).

94 J. S. Waugh, A. E. Paladino, B. diBenedetto and R. Wantman, "Effect of Dislocations on Oxidation and Reduction of Single Crystal $SrTiO_3$", J. Am. Ceram. Soc. 46, 60 (1963).

95 N. M. Parikh, "Cermets: III Modes of Fracture and Slip in Cemented Carbides", J. Am. Ceram. Soc. 40, 335-39 (1957)

96 W. M. Hirthe and J. O. Brittain, "Dislocations in Rutile as Revealed by the Etch-Pit Techniques", J. Am. Ceram. Soc. 45, 347-51 (1962).

97 A. Accary and R. Caillat, "Study of Mechanism of Reaction Hot Pressing", J. Am. Ceram. Soc. 45, 347-51 (1962).

98 N. Fuhrman, L. D. Hower Jr., and R. B. Holden, "Low Temperature Sintering of Uranium Dioxide", J. Am. Ceram. Soc. 46,114-121 (1963).

99 David C. Hill, "Volatility Behavior of Urania-Lanthana Solid Solutions", J. Am. Ceram. Soc. 45, 143-44 (1962).

100 P. D. Shalek, "Preparation and Properties of Uranium and Thorium Monosulfides", J. Am. Ceram. Soc. 46, 155-61 (1963).

101 R. G. Rudness and R. W. Kebler, "Growth of Single Crystals of Incongruently Melting Yttrium Iron Garnet by Flame Fusion Process", J. Am. Ceram. Soc. 43, 17-22 (1960).

102 R. A. Lefever and A. B. Chase, "Analysis of Surface Fractures on Single Crystals of Synthetic Garnets", J. Am. Ceram. Soc. 45, 32-36 (1962).

103 F. Trojer, "Mineralogische Untersuchungsverfahren auf dem Gebiete des Hüttenwesens mit Beispielen über Verschleissvorgänge an Gitterstein", Ber. deut. keram. Ges. 38, 557-69 (1961).

104 Peter Angelides, "Relief Polishing of High-Alumina Ceramics for Metallographic Study", J. Am. Ceram. Soc. 44, 145 (1961).

105 S. S. Cole, Jr., and G. Sommer, "Glass-Migration Mechanism of Ceramic-to-Metal Seal Adherence", J. Am. Ceram. Soc. 44, 265-271 (1961).

106 Edwin K. Beauchamp, "The Etching of Al_2O_3 Grain Boundaries", J. Am. Ceram. Soc. 43, 224 (1960).

107 P. E. Evans, "Interpretation of the System UO_2-ZrO_2", J. Am. Ceram. Soc. 44, 631 (1961).

108 T. K. Bierlein, H. W. Newkirk, Jr., and B. Matel, "Etching of Refractories and Cermets by Ion Bombbardment", J. Am. Ceram. Soc. 41, 196-200 (1958).

109 G. A. Keig and H. R. Haines, "The Cathodic Etching of Plutonium Ceramics", Trans. Brit. Ceram. Soc. 62, 363-73 (1963).

110 W. J. Coy, "Electron Microscope Study of Pyrolytic Graphite", J. Am. Ceram. Soc. 45, 223-25 (1962).

111 Hayne Palmour III, John Duplessis and W. Wurth Kriegel, "Microstructural Features and Dislocations on Thermally Etched Sapphire Surfaces", J. Am. Ceram. Soc. 44, 400-404 (1961).

112 E. N. Andrade and L. C. Tsien, "Surface Cracks in Glasses", Proc. Royal Soc. (London) A 159, 346-55 (1937).

113 W. C. Levengood and E. B. Butler, "Relationship of Surface Structure of Glass to Residual Laminar Stresses", J. Am. Ceram. Soc. 36, 257-62 (1953).

114 S. Amelinckx, "Dislocations in Ionic Crystals. I. Geometry of Dislocations" in Mechanical Properties of Engineering Ceramics, W. W. Kriegel and H. Palmour III, ed., Interscience (New York, 1961).

115 F. A. Petersen, R. A. Jones and A. W. Allen, " A New Method for Studying Fractures of Porcelain Enameled Specimens", J. Am. Ceram. Soc. 31, 186-93 (1948).

116 J. H. Lauchner and D. G. Bennett, "Thermal Fracture Resistance of Ceramic Coatings Applied to Metal: I Elastic Deformation", J. Am. Ceram. Soc. 42, 146-50 (1959).

117 W. L. Phillips, Jr., "Effect of Environment and Surface Condition on Strength of Lithium Fluoride Single Crystals", J. Am. Ceram. Soc. 44, 395-400 (1961).

118 V. K. Zworykin and E. G. Ramberg, "Surface Studies with the Electron Microscope", J. Appl. Physics 12, 692-5 (1941).

119 Robert Scheuplein and Peter Gibbs, "Surface Structure in Corundum: II Dislocation Structure and Fracture of Deformed Single Crystals", J. Am. Ceram. Soc. 45, 439 (1962).

120 W. Schatt and D. Schulze, "Einige Elektronenmikroskopische Beobachtungen an Freien Sinterkorundoberflächen", Ber deut. keram. Ges. 36, 364-67 (1959).

121 A. F. Prebus and J. W. Michener, "Electron Microscope Investigation of Glass", Ind. Eng. Chem. 46, 147-53 (1954).

122 K. H. Kim and F. A. Hummel, "Studies in Lithium Oxide Systems: VI Progress Report on the System Li_2O-SiO_2-TiO_2", J. Am. Ceram. Soc. 42, 286-91, (1959).

123 B.S.R. Sastry and F.A. Hummel, "Studies in Lithium Oxide Systems VII Li_2O-B_2O_3-SiO_2", J. Am. Ceram. Soc. 43, 23-33 (1960).

124 F. A. Hummel, T.Y. Tien and K. H. Kim, "Studies in Lithium Oxide Systems. VIII Application of Silicate Liquid Immiscibility to Development of Opaque Glazes", J. Am. Ceram. Soc. 43,192-97(1960).

125 T. Y. Tien and F. A. Hummel, "Studies in Lithium Oxide Systems XI Li_2O-B_2O_3-P_2O_5", J. Am. Ceram. Soc. 44, 390-94 (1961).

126 M. Krishna Murthy, "Influence of Platinum Nucleation on Constitution of and Phase Separation in Sodium Phosphate Glasses", J. Am. Ceram. Soc. 44, 412-417 (1961).

127 T. F. Bates and M. V. Black, "Electron Microscope Investigation of Opal Glass", Glass Ind. 29, 487-92, 516, 518 (1948).

128 Muneo Watanabe, Haruo Noake and Takeshi Aiba, "Electron Micrographs of Some Borosilicate Glasses and Their Internal Structure", J. Am. Ceram. Soc. 42, 593-99 (1959).

129 I. Warshaw, "Structural Implications of the Electron Microscopy of Glass Surfaces", J. Am. Ceram. Soc. 43, 4-9 (1960).

130 Stanley M. Ohlberg, Helen R. Golob, and Charles M. Hollabough, "Fractography of Glasses Evidencing Liquid in Liquid Colloidal Immiscibility", J. Am. Ceram. Soc. 45, 1-4 (1962).

131 Georges Zarzycki and Rene Mezard, "Etude de la Structure Fine du Verre", Compt. Rend. 254, 1755-56 (1962).

132 V. J. Moran, "Structure in the Fracture Surface of Silicate Glass", J. Am. Ceram. Soc. 46, 102-103 (1963).

133 A. W. Allen and A. L. Friedberg, "Application of Replica Techniques to the Study of Ceramic Surfaces with the Optical Microscope", J. Am. Ceram. Soc. 31, 83-88 (1948).

134 J. C. Richmond and A. C. Francisco, "Use of Plastic Replicas in Evaluating Surface Texture of Enamels", J. Res. Nat. Bur. Stds. 42, 449-460 (1949).

135 R. D. Heidenreich, "Methods in Electron Microscopy of Solids", Rev. of Scientific Instruments 23, 583-95 (1952).

136 D. E. Bradley, "High Resolution Evaporated Carbon Replica Technique for the Electron Microscope",J. Inst. Metals 83, 35-38 (1954).

137 D. E. Bradley, "An Evaporated Carbon Replica Technique for Use with the Electron Microscope and its Application to the Study of Photographic Grains", Brit. J. Appl. Phys. 5, 96-98 (1954).

138 Yoshio, Iida, "Sintering of High-Purity Nickel Oxide", J. Am. Ceram. Soc. 41, 397-406 (1958).

139 R. Dallendorfer, "Licht-und Elektronenmikroskopische Oberflächenuntersuchungen an Keramischen Werkstoffen", Silikattechn. 9, 510-13 (1958).

140 V. J. Tennery and F. F. Anderson, "Examination of Surface and Domain Structure in Ceramic Barium Titanate", J. Appl. Phys. 29,755-758 (1958).

141 H. E. Simpson, "Study of Surface Structure of Glass as Related to its Durability", J. Am. Ceram. Soc. 41, 43-40 (1958).

142 W. Heister, "Einfluss der Sintertemperatur auf die Magnetischen Eigenschaften and das Kristallgefüge von Mn-Zn Ferrites", Ber. deut. keram. Ges. 35, 249-258 (1958).

143 J. Kainz, "Die Dielektrischen Eigenschaften des Systems Barium-Strontium_Lanthanum Titanate", Ber. deut. keram. Ges. 35, 69-77 (1958).

144 B.S.R. Sastry and F. A. Hummel, "Studies in Lithium Oxide Systems III Liquid Immiscibility in the System Li_2O-$B_2O_3SiO_2$", J. Am. Ceram. Soc. 42, 81-88 (1959).

145 Joseph Comer, "Electron Microscope Studies of Mullite Development in Fired Kaolins", J. Am. Ceram. Soc. 43, 378-84, (1960).

146 K. Schüller, "Untersuchungen uber die Gefügeausbildung im Porzellan", Ber.deut. keram. Ges. 38, 150-157; 208-11; 241-46 (1961).

147 J. Drobek, W. C. Bigelow and R. G. Wells, "Electron Microscopic Studies of Growth Structures in Hexagonal Ferrites", J. Am. Ceram. Soc. 45,262-64 (1961).

148 M. Navey, C. Sella, H. Gervais and J. J. Trillat, "Appareillage pour La Realisation Sous Vide de Repliques et d'Empreintes pour la Microscopie Electronque", Vide 6,91-97 (1961).

149 J. J. Comer, "New Electron-Optical Data on the Kaolinite-Mullite Transformation", J. Am. Ceram. Soc. 44, 561-63 (1961).

150 T.Y. Tien and W. G. Carlson, "Effect of Additives on Properties of Lead Titanate", J. Am. Ceram. Soc. 45, 567-571 (1962).

The Effect of Heat Treatment on Microstructure

J. E. Burke

1. Introduction

At some stage during processing, most ceramics are heated to an elevated temperature, held for a time and then cooled. During this heat treatment, many profound changes in structure may occur and the final microstructure is established. For example, the identity, amount, composition, perfection, size, geometrical arrangement or crystallographic orientation of the phases initially present may change. The composition of the whole body may change if volatile species evaporate or are picked up from the heat treating atmosphere. Our goal in this paper is to set down some simple general principles governing the effect of heat treatment on microstructure. Some of the principles are concerned with establishing, from phase stability studies, what phases are stable at the heat-treating temperatures. Some are concerned with the influence of forces such as surface tension upon the geometry of phases. These aspects have been well covered by other speakers in this series, and I should like to concern myself with the problem of relating temperature to the rate at which the approach to equilibrium is made. This is not a new branch of science, although it has developed rapidly over the past 20 years. Furthermore, this is not intended as an elegant treatment, but rather as a practical one, to provide a way of thinking about reactions in solids, with enough information so that semiquantitative calculations can be made. For more quantitative treatment, the reader is referred to the standard texts.

2. Diffusion

Undoubtedly the most important single reaction which may occur during heat treatment is the diffusional transport of individual atoms through the solid from their initial positions to new positions of greater thermodynamic stability. It is by such transport that concentration gradients are smoothed out, that phases form and disappear, and that shrinkage and pore elimination during sintering is accomplished.

The elementary mathematics of the diffusion process was first formulated over 100 years ago, and during the ensuing period many measurements of diffusion rates of certain atomic species in various solids have been made, and quite detailed knowledge of the mechanisms by which diffusion occurs now exists. There are many review papers on the subject, particularly in metals, and many textbooks of metallurgy and ceramics have extensive treatments of the subject [1].[1] In spite of all this work, it should be mentioned that a complete understanding of diffusion does not yet exist, particularly in ceramic materials, and it is an active field of research at the present time. In this section an attempt is made to establish only the most elementary concepts so they can be used in later discussions.

[1] Figures in brackets indicate the literature references at the end of this paper.

Let us consider a system in which there is a sudden change in composition with distance, such as might exist if a piece of pure aluminum oxide were to be welded to a ruby which contains a small amount of dissolved Cr_2O_3 replacing some of the Al_2O_3. It has been established that in Al_2O_3 the oxygen ions form a relatively rigid framework, so that upon heating, some of the Cr^{+3} ions will diffuse into the sapphire and this diffusion will be compensated by a counter-diffusion of Al^{+3} ions into the ruby. The situation is presented schematically in Fig. 1, where the solid line shows the concentration gradient assumed to exist initially and the two dotted lines show the concentration gradients after two successive times of heat treatment.

The general law governing this process, and the law from which the shape of these penetration curves can be explained, at least in principle, was formulated by Fick in 1855. In its simplest form it states:

$$J = -D \frac{\partial C}{\partial X} \qquad (1)$$

the quantity J of diffusion substance which passes per unit time through a unit area of a plane at right angles to the direction of diffusion is proportional to the concentration gradient of the diffusing substance $\partial C/\partial X$. The negative sign appears to compensate for the fact that the slope of concentration versus distance curve which favors diffusion is negative. The proportionality constant, D, is called the diffusion coefficient, and its absolute value serves to characterize the diffusion rate of the diffusing species in that substance. Commonly it is stated in units of cm^2 per second. The larger is the value, the shorter will be the heat-treating times necessary to accomplish a given amount of diffusion. The value of D can be measured in many ways, typically from measurements of concentration - distance curves of the type presented in Fig. 1.

It will be immediately evident from an examination of the literature that the above description is greatly over-simplified. In particular, the value of D is not independent of composition, and if a phase boundary is involved, it is possible for diffusion of an atomic species to occur from one phase where its concentration is low (but its thermodynamic activity is high) to another phase where its absolute concentration is higher (but its thermodynamic activity is lower). In spite of this, we shall consider here that the diffusion constant has a single value for a given diffusing species in a given material, at constant temperature.

Darken [1] has pointed out a simple relationship which can be very roughly used to compute minimum heat treating times, and which permits a feeling to be obtained for the absolute values of diffusion coefficients.

Diffusion is substantially complete when

$$t = \ell^2/D \qquad (2)$$

where t is the diffusion time in seconds and ℓ is the radius (or minimum dimension of the particle concerned) in centimeters. Thus, if one were concerned with determining the minimum heat-treating time necessary to cause homogenization in an aggregate of 2μ radius particles at a temperature where the diffusion coefficient for the diffusing species is 1×10^{-10} cm^2 sec^{-1} he would find

$$t = \frac{(2 \times 10^{-4})^2}{1 \times 10^{-10}} = 4 \times 10^2 \text{ seconds}$$

If the particle size were doubled, the time would be increased by a factor of 4. In practice, the actual times might be very much longer than those computed in this way because pores and imperfect contacts between particles reduce the effective inter-

diffusion area and increase the diffusion distance. On the other hand, if the necessary time for one particle size is known, the increase in time for an increase in particle size should be given reasonably well by this relationship, assuming that the two systems are geometrically similar.

3. Factors Influence the Diffusion Rate

There are many factors which may influence the diffusion rate in ceramics. Undoubtedly the most important one is temperature, and this is discussed in some detail in a following section.

Most theories of diffusion assume that the atoms move by utilizing crystallographic defects, particularly unoccupied lattice sites, to accomplish the rearrangement. A major effect of increasing the temperature is to increase this number of defects, so that diffusion is speeded up. The addition of impurity atoms, particularly those of a different valence, may also cause the formation of unoccupied lattice sites. For example, if Ca^{+2} ions are substituted for Zr^{+4} ions in ZrO_2, one unoccupied oxygen site is formed for each such substitution. With large substitutions many such sites are formed and the diffusion coefficient for oxygen ions is tremendously increased.

Many impurity additions may operate in a similar way to increase diffusion coefficients and thus to increase the rate of heat-treating reactions, but it is not assured that increasing the diffusion rate of one ionic species in a compound will necessarily increase the reaction-rate.

Two categories of diffusion reactions may be considered -

1) In the example cited above, the oxygen framework remains fixed, and the chromium and aluminum ions interchange. Any factors influencing the diffusivity of these ions will influence the velocity of the homogenization of the two crystals.

2) In reactions such as sintering, both atomic species must move. If the objective of the heat-treatment were to cause sintering of aluminum oxide particles, the diffusion rate of the oxygen ion would be all-important since it is slower moving and rate controlling. Any factor, such as an impurity, that would modify the oxygen ion mobility, would greatly speed up the sintering rate. If the rate of aluminum ion diffusion alone were affected, the sintering rate would be unchanged.

It is commonly observed also that diffusion at grain boundaries in polycrystalline solids is greatly enhanced. There is presently some obscurity in determining whether or not this is universally true, or whether only the slower moving species are speeded up. More work needs to be done, but at the present time there are strong indications that the behavior of ceramics does not parallel that of metals.

4. Effect of Temperature on Reaction Rates

Most chemical reactions are observed to increase rapidly in rate as the temperature is increased. The so-called Arrhenius relationship is that:

$$\text{Rate} = K\, e^{-Q/RT} \qquad (3)$$

or $$\ln \text{Rate} = \ln K - Q/RT$$

or $$\log \text{Rate} = \log K - \frac{Q}{2.3\,RT}$$

where the pre-exponential proportionality constant and the exponent Q (the activation energy) are characteristic of the reaction concerned. R is the gas laws' constant, and T the absolute temperature.

In chemical usage, quantities are expressed in moles, or gram formula weights of the reacting substances, R, the gas laws' constant, is expressed in calories per degree (1.986 ≈ 2.0), and Q has the dimensions of calories per gram formula weight. Frequently, the computation is done on a per atom basis. Then the Boltzman gas constant k is used in place of R, and it is commonly expressed in electron volts per degree C (8.6×10^{-4}). Q has the dimension of electron volts per atom. Approximately, 1 ev per atom = 23,000 cal per gram atom.

The diffusion coefficient D is a measure of the rate of the diffusion reaction. Its temperature dependence is commonly determined, and presented in the form

$$D = D_o e^{-Q/RT} \qquad (4)$$

If the value of D_o and Q are given, the value of the diffusion coefficient at any temperature may be computed. A typical value of D_o is unity and reported values range at least from 10^{-4} to 10^{4} cm^2 per second. Occasionally very much larger or smaller values for D_o are published, but these should be viewed with caution. Values for Q are not so variable. They range typically from 10,000 calories per mole for rapid reactions which will occur at an appreciable rate at room temperature to 150,000 or even 200,000 calories per mole for reactions in refractory materials that are observable only at temperatures above 1000°C. A few typical values are listed in Table 1.

TABLE 1. Typical values for some diffusion coefficients

Matrix Substance	Diffusing Ion	D_o cm^2/sec	Q KCal/Mole	Remarks	Reference
Al_2O_3	$O^{=}$	1.9×10^{3}	152	Single Crystal	[3]
Al_2O_3	$O^{=}$	2×10^{0}	110	Polycrystal	[3]
Al_2O_3	Al^{+3}	2.8×10^{1}	114	Polycrystal	[4]
UO_2	U^{+4}	4.3×10^{-4}	88	Stoichiometric UO_2	[5]
UO_2	$O^{=}$	1.2×10^{3}	65	Stoichiometric UO_2	[5]
UO_2	$O^{=}$	2.7×10^{-3}	29.7	Non-Stoichiometric $UO_{2.06}$	[5]
CaO-Stabilized ZrO_2	Ca^{++}	4.1×10^{-1}	100	12 and 16 mol % CaO	[6]
	Zr^{+4}	2.1×10^{-1}	100	12 and 16 mol % CaO	[6]
	$O^{=}$	1×10^{-2}	28.1	15 mol % CaO	[7]

4a. Isothermal Reaction Rates

We have just seen that the use of the Arrhenius relationship relating reaction rate to temperature provides a compact means of describing the diffusion rate of one substance in another. The same approach may also be used to predict the effect of a change of temperature upon the time necessary for a given amount of reaction if the value of the activation energy, Q, is known or can be determined. This approach works well only in those cases where the driving force for the reaction is not strongly influenced by temperature, as is commonly the case in sintering, viscous flow, homogenization by diffusion or grain growth. If a phase change is involved in the reaction the situation may be more complicated, as is discussed below.

It is common, for development purposes, to determine a proper firing temperature for a ceramic by conducting a series of ISOCHRONAL observations, firing for a given time at a series of temperatures, and presenting the results, for example, as a plot of density, or grain size versus firing temperature. Fig. 2 presents such a plot, in which for purposes of illustration, an arbitrary parameter V, having the dimensions of length and representing a phenomenon such as a length change, has been plotted against firing temperature.

Such an approach assumes that temperature is of primary importance in characterizing the heat-treatment, and that changing the time of heat-treatment has little effect. It is apparently justified if one plots, on ordinary graph paper, the results of measurements of the property concerned as a function of time. As is shown in Fig. 3, the properties appear to reach more or less stable values at each temperature.

In Fig. 4, log V has been plotted versus log time, and it can be seen that the reaction is continuing at each temperature in the same way. Only the time scale has been shifted. Figure 3 incorrectly implies that the amount of reaction is controlled by the temperature. It is controlled by temperature only if the same annealing time is used at each temperature.

If one is concerned with commercial processing, and is limited to a period such as an hour for heat treating, then such conclusions are correct. In those cases, heating a specimen to an elevated temperature will effectively stabilize it against change with respect to short time heat-treatments at lower temperatures. On the other hand, if one is concerned with long term stability, as in creep, then comprehension of the fact that reaction may continue indefinitely even at low temperatures is of great importance.

The curves in Figures 2 - 4 were computed from the relationship

$$V = kt^{1/2}$$

and k was assumed to vary with temperature as

$$k = k_o \exp\left(\frac{-100{,}000}{RT}\right)$$

This equation is reasonably representative of many of the structure-controlling reactions in ceramics.

In diffusion-controlled reactions, the thickness of a diffusion layer or the thickness of an oxide film or reaction product formed by diffusion will be given, at least approximately, by the relationship

$$\text{Thickness} = kt^{1/2} \qquad (5)$$

which gives rise to the so-called parabolic rate law for most tarnishing reactions. The rate constant k is characteristic of that of a thermally activated process, and increases exponentially with increasing temperature.

The rate of grain growth in most materials is found roughly to be inversely proportional to the grain size S, thus:

$$\frac{dS}{dt} = \frac{k}{S} \qquad (6)$$

and $$S^2 - S_o^2 = kt$$

where S_o is the grain size at $t = 0$. Assuming it to be much smaller than S, one can deduce the commonly used grain growth equation

$$S = kt^{1/2} \qquad (7)$$

where k varies with temperature according to the Arrhenius relationship.

Sintering in many systems is observed to obey a similar law. The fractional shrinkage in the initial stages can commonly be approximated by

$$\frac{\Delta L}{L_o} = kt^{2/5} \qquad (8)$$

where again the rate constant k varies exponentially with temperature.

Many of the reactions tend to be self-limiting in this way. If the concern is with having a reaction go to completion for processing reasons, times at low temperatures may become excessively long, and the only practical way to attain more complete reaction is to use higher processing temperatures. On the other hand, if the concern is with long term stability, say resistance to plastic deformation by creep, lowering the temperature will lower the rate, but deformation will continue.

4b. The Effect of Heating Rate

It is obvious that many different reactions may go on simultaneously during heat treatment. The question sometimes arises: can one of these be favored over the other by changing the heating rate or the heat-treating temperature? For example, can shrinkage be accomplished with less grain growth by raising the temperature to speed up sintering and keeping the time short so that not much grain growth occurs? The answer in general must be "no". The precise answer is shown by the relative values of the activation energy, Q in equation 3 for the two competitive processes concerned. If the Q for each process is about the same, (as it usually is) than raising the reaction temperature or changing the heating rate will affect each of the processes equally, and the only effect will be to change the time necessary for reaction. If, however, for example, the activation energy for grain growth were to be higher than the activation energy for sintering, then indeed, raising the temperature would increase the rate of grain growth faster than it would increase the rate of sintering. A fine grained body would be obtained in that case by firing at the lowest temperature consistent with the available heat treatment time.

Usually, the activation energies for the independent processes are not known, and the effect of temperature on the relative rates of two identifiable competing reactions is best determined by examining microstructures of specimens heated at two different temperatures for times which are adjusted to cause comparable amounts of reaction at each temperature.

5. Determination of Activation Energies

It is conventional to determine activation energies by evaluating some specific rate constant in the reaction law, such as the diffusion coefficient D in equation 1, at several temperatures. Then, a plot of the logarithm of the rate constant versus the reciprocal of the absolute temperature should give a straight line whose slope is $Q/2.3R$.

This is readily seen from the rearrangement

$$D = D_o e^{-Q/RT} \qquad (9)$$

$$\ln D = 2.3 \log D = \frac{-Q}{R}\left(\frac{1}{T}\right) + \ln D_o$$

Rigorously speaking, this method is valid only if it can be independently demonstrated that the sole effect of changing the temperature has been to change atomic mobility. In practice, the existence of a straight line relationship on such a plot is usually taken as evidence that the procedure is valid.

In Fig. 5, the data from Fig. 4 have been replotted to permit a determination of the value of Q. A measure of the reaction rate, the reciprocal of the time necessary to produce a given amount of reaction, has been plotted against the reciprocal of the absolute temperature. The activation energy can be determined from the slope as indicated

$$\text{slope} = \frac{-1}{5.64 \times 10^{-4} - 5.18 \times 10^{-4}} = \frac{-1}{4.6 \times 10^{-5}} = \frac{-Q}{2.3R}$$

$Q = 100{,}000$ cal/gram formula weight.

It will be noticed that the value of the activation energy does not depend upon the stage in the reaction at which the temperature dependence of the rate is determined.

When the law governing the process at hand is complex, it is sometimes difficult to evaluate a rate constant with precision. Under these conditions the following relationship will be found useful:

$$2.3 \log \left(\frac{t_1}{t_2}\right) = \frac{Q}{R}\left(\frac{1}{T_1} - \frac{1}{T_2}\right) \qquad (10)$$

where t_1 and t_2 are the times at Kelvin temperatures T_1 and T_2. If the reaction occurring at different temperatures is essentially the same one, all of the curves on a plot of the type shown in Fig. 4 should be parallel (although they may not be straight lines) and it should be possible to superimpose them by the use of an appropriate multiplying factor computed with the aid of equation 10. Such techniques provide an approach to the selection of heat-treating times which should produce comparable amounts of reaction if the temperature is changed.

In determining activation energies, proper selectivity must be exercised in determining the value of the rate. It is not permissible to state a shrinkage rate as a certain percentage shrinkage per unit time, because the value of this rate will depend upon the time period considered, and upon the shrinkage which has previously been accomplished. On the other hand, it is permissible to measure the time necessary for a reaction to cause a property to change from a given initial value to a given final value as a function of temperature, as was done for Fig. 5, and to plot the reciprocal of this time versus 1/T to obtain a value for the activation energy. For example, one might measure the time necessary to produce 5% shrinkage and plot its reciprocal versus 1/T.

6. Phase Transformation

The discussions presented above assumed that the driving force for the reaction was not profoundly altered by temperature, so the rate would depend almost entirely

upon atomic mobility. When a phase transformation occurs, there are problems in forming nuclei of the new phase, and the driving force for the reaction increases with supercooling while atomic mobility decreases. It is therefore sometimes difficult to predict whether a change in temperature will increase or decrease the rate of the reaction.

6a. Nucleation

The problem of nucleation of a new phase is well understood, and the kinetics of the process have been studied in great detail. Discussions of the phenomenon may be found in several reviews [2].

In these theories, the driving force for the transformation is the free energy decrease associated with the transformation of a volume of the phase $4/3\pi r^3$ to the more stable modification. When this new phase forms, an interface of area $4\pi r^2$ is formed. Thus the total energy change associated with the process is

$$\Delta F = -\frac{4}{3}\pi r^3 \Delta F_v + 4\pi r^2 \gamma \qquad (11)$$

where ΔF_v is the decrease in free energy per unit volume associated with the transformation and γ is the surface free energy of the interface per unit area.

The important geometrical parameters are set forth in Fig. 6 and a plot of this behavior is shown in Fig. 7.

Most of the theoretical studies of nucleation and phase transformation have dealt with the problem of describing the factors influencing the rate of nucleation. We shall not attempt to reproduce these here, but shall merely qualitatively describe the conclusions. The stable nucleus must grow by the addition of atoms in the stable configuration. In a pure system this is an energetically unfavorable process at temperatures close to the transformation temperature, so considerable undercooling may be required, and the rate of nucleation increases with increasing undercooling.

The need to supply an interface of energy $4\pi r^2\gamma$, eq. (11), when a new phase forms constitutes a nucleation barrier which can be greatly modified by impurities. If impurities are in solid solution they may adsorb at the new interface, decrease the interfacial energy γ, and thus facilitate nucleation. If they are present as second phase inclusions, they may serve as nucleation catalysts since the interfacial energy between the inclusion and the new phase may be less than between the new phase and the original matrix.

6b. Rate of Phase Transformations

Once nucleation is established, the rate of the phase transformation will be controlled by two parameters, the driving force, which increases with the supercooling below the transformation temperature, and the atomic mobility, measured for example by the diffusion coefficient. Thus

$$\text{Rate} = \text{Const.}\ f\left(\frac{\Delta T}{T_e}\right) \cdot D_o e^{-Q/RT} \qquad (12)$$

At the transformation temperature, Te, $\Delta T = 0$ and the reaction rate is low. As ΔT increases the reaction rate will increase until it begins to be limited by the decreasing atomic mobility at lower temperatures, when the rate will again fall. A schematic presentation of such behavior is given in Fig. 8.

Reactions of this type are well known in the heat treatment of metals, where their understanding provides the basis for the control of the heat-treatment of steel. Probably the most striking example in ceramics is the devitrification or controlled crystallization of glass. At both high and low temperatures the transformation rate is low, and at intermediate temperatures it is high. It is self-evident that although reactions of this type are indeed thermally activated, one cannot compute activation energies in the conventional way, nor can he without additional information predict the effect of temperature on reaction rate.

7. Applications

Examples of the applications of these principles might be given almost without end. In practically no case can they be applied without thought, however. This will be illustrated by reference to the factors controlling the rate of sintering in an essentially pure single phase oxide.

It is reasonably well demonstrated that sintering is accomplished by the diffusional transport of atoms from grain boundaries to pores. The pores are filled, and the space left at the grain boundaries is closed by moving the grains closer together and thus accomplishing shrinkage. What factors may influence the sintering rate?

1) The sintering temperature, because with other conditions constant it will control the rate at which the atoms move.

2) The initial particle size, because it will control the distance atoms must move to accomplish shrinkage, and thus the time required for movement.

3) The possible occurrence of grain growth during sintering. This can be detected only by microscopic examination, but it will alter the necessary diffusion distance just as certainly as changing the particle size. In either case, doubling the particle size will quadruple the sintering time.

4) The presence of an impurity in the starting material - it may do at least three different things:

a) Modify the diffusion rate of the slower moving species, and thus modify the sintering rate.

b) Inhibit grain growth, and thus control the diffusion distance and hence the sintering time.

c) Cause the appearance of a liquid phase which can completely modify the shrinkage mechanism.

5) Reaction with the atmosphere. This may modify the stoichiometry of the sintering material, and thus diffusion coefficients and reaction rates. Or the atmosphere may become entrapped in pores and mechanically prevent shrinkage.

There is no simple road to understanding the effect of heat-treatment on microstructure. To understand what is going on, and to be able to predict what effect changes in processing conditions will have on structure and properties, the experimentalist will however find it helpful to follow the process by measuring the changes in some sensitive parameter in a series of isothermal heat treatments made at a sequence of times at a variety of temperatures and at the same time, follow the changes in microstructure which occur as a consequence of these heat treatments. In this way, he should be able to at least describe the process in quantitative terms, and under favorable conditions he should be able to understand what is going on in a fundamental way.

References

[1] See for example:

L. S. Darken and others, in Atom Movements, A.S.M. (Cleveland, Ohio, 1951).

W. D. Kingery, Introduction to Ceramics, p. 217, John Wiley & Sons, Inc. (New York, 1960).

Ling Yang, and M. T. Simnad, in Physicochemical Measurements at High Temperatures, edited by J. O'M. Bockris, J. L. White, and J. D. Mackenzie, Butterworths Scientific Publications, p. 295 (London, 1951).

[2] S. D. Stookey and R. D. Maurer, Progr. Ceram. Sci. 2, 77 (1961).

J. E. Burke and D. Turnbull, Progr. in Metal Phys. 3, 254 (1952).

J. H. Hollomon and D. Turnbull, Progr. in Metal Phys. 4, 336 (1953).

W. D. Kingery, Introduction to Ceramics, p. 296, John Wiley & Sons, Inc. (New York, 1960).

[3] Y. Oishi and W. D. Kingery, J. Chem. Phys. 33, 480 (1960).

[4] A. E. Paladino and W. D. Kingery, J. Chem. Phys. 37, 957 (1962).

[5] A. B. Auskern and J. Belle, in Uranium Dioxide: Properties and Nuclear Applications, edited by J. Belle, USAEC, p. 309, U. S. Government Printing Office, Washington, D. C. (1961).

[6] W. H. Rhodes and R. E. Carter, Bull. Am. Ceram. Soc. 41, 283 (1962).

[7] W. D. Kingery, J. Pappis, M. E. Doty, and D. C. Hill, J. Am. Ceram. Soc. 42, 393 (1959).

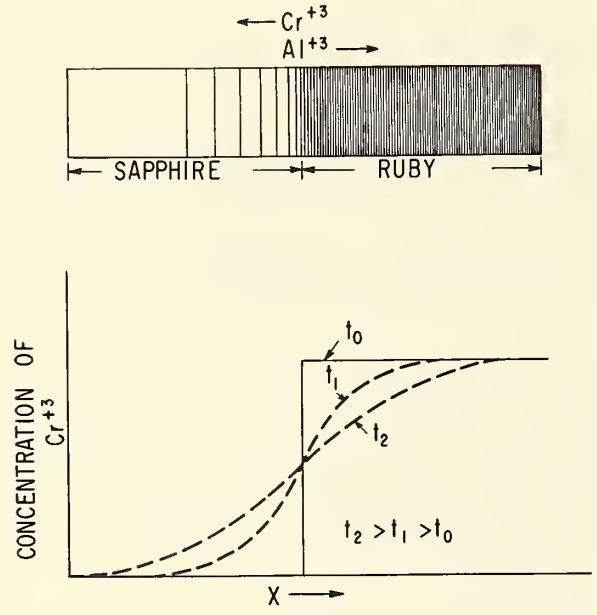

FIGURE 1. Schematic representation of diffusion. Upper diagram represents exchange of Cr^{+3} and Al^{+3} ions between ruby and sapphire. Lower diagram shows Cr^{+3} concentration gradient at various times.

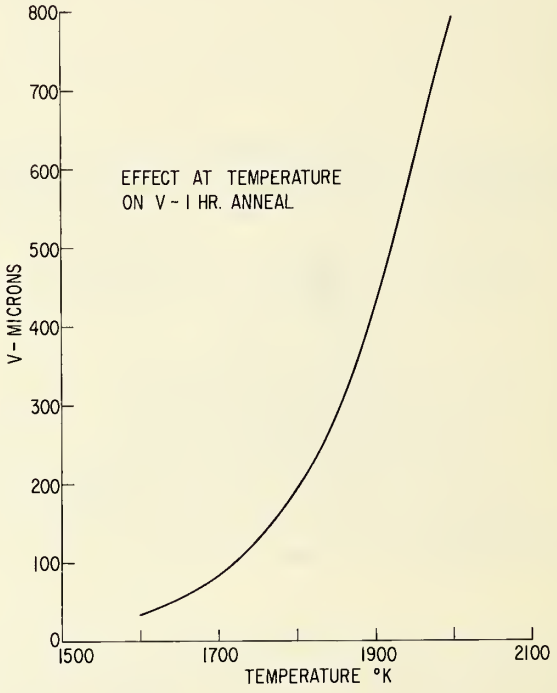

FIGURE 2. Isochronal reaction curve showing variation of extent of reaction, V, with temperature at constant annealing time.

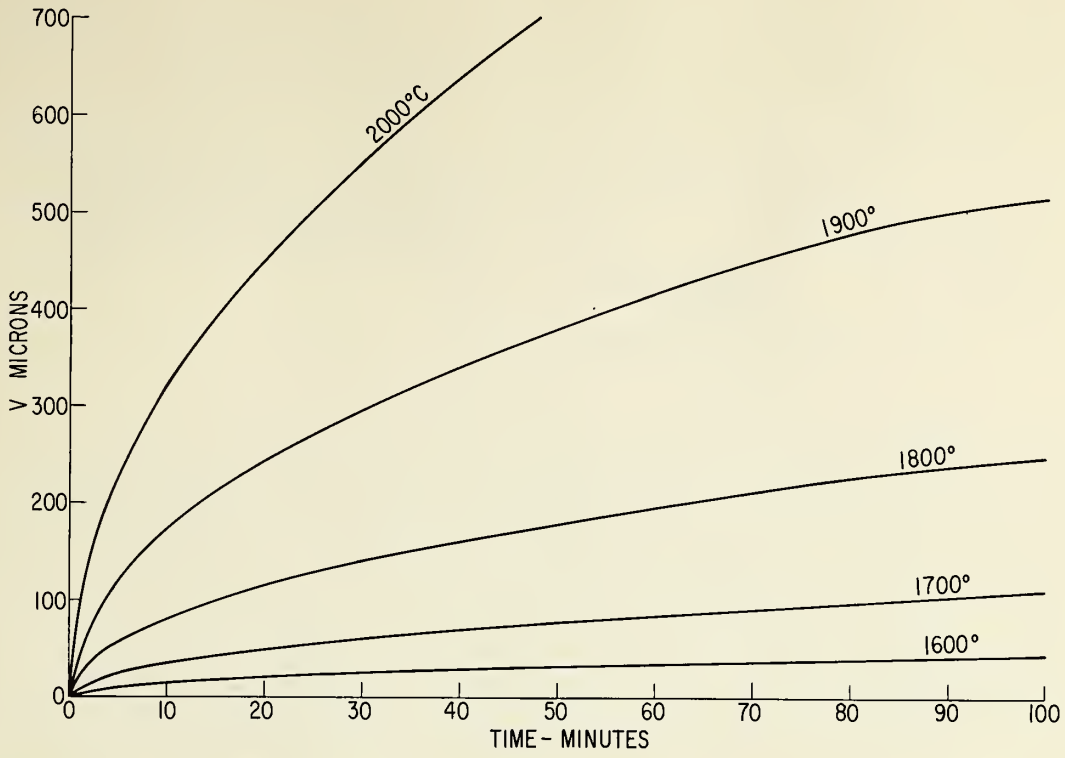

FIGURE 3. Arithmetic plot of isothermal reaction data. Apparent cessation of reaction at each temperature is misleading, and consequence of reaction law.

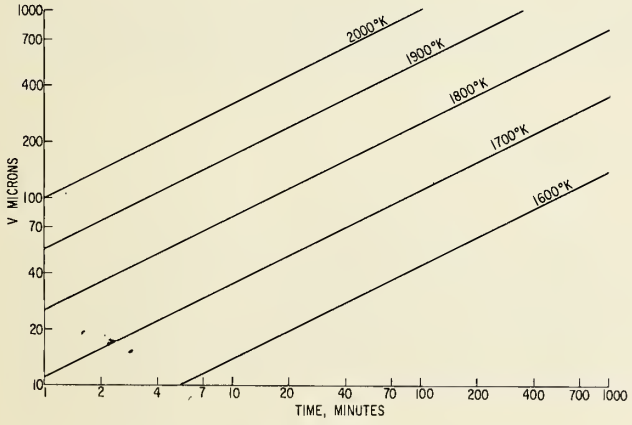

FIGURE 4. Logarithmic plot of isothermal reaction data. Parallel curves indicate that reaction law is the same at all temperatures.

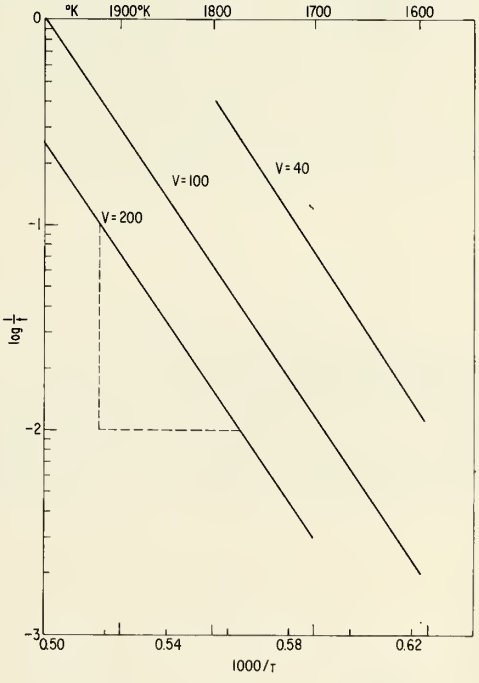

FIGURE 5. Method of computing activation energy,

$$\log \text{rate} \quad \log 1/t = \frac{-Q}{2.3R}\left(\frac{1}{T}\right)$$

so slope is $-Q/2.3R$.

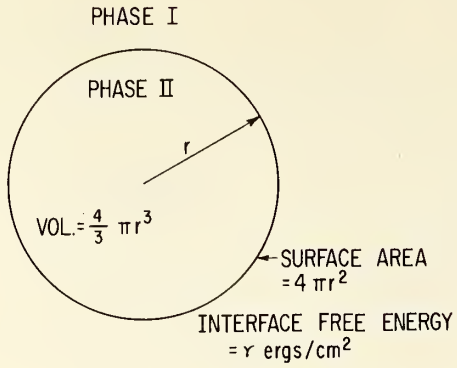

FIGURE 6. Geometrical parameters in nucleation, see eq. (11).

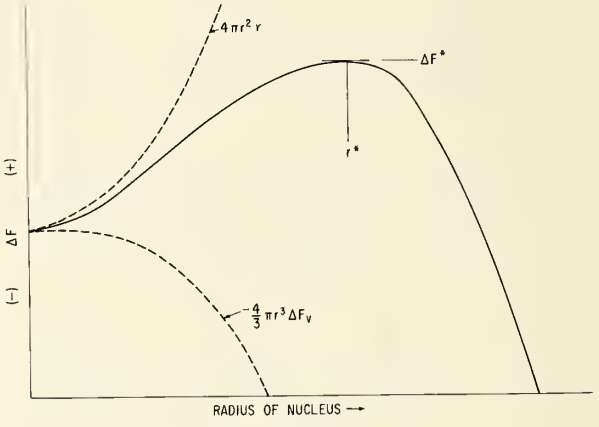

FIGURE 7. Plot of conditions for formation of stable nucleus of radius r*.

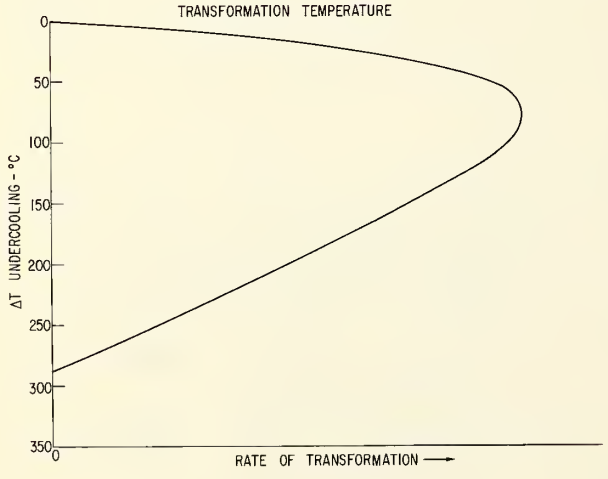

FIGURE 8. Rate of transformation versus undercooling, see eq. (12).

Correlation of Mechanical Properties with Microstructure

Robert J. Stokes

1. Introduction

The last review article on this subject was prepared by Coble in 1956 and was subsequently published in 1958 [1][1]. Since that time, a number of conferences on allied topics have been held and the proceedings published but no review specifically on the effects of microstructure has appeared. The period 1956 to the present has been particularly productive since it corresponded at the start with the beautiful etching experiments on dislocations in lithium fluoride by Gilman and Johnston [2] and the demonstration by Gorum et al. [3] that single crystals of magnesium oxide could be deformed plastically at room temperature. The implication from this latter work that certain ceramic materials might possess ductility led to increased research activity in the field of the mechanical behavior of ceramics. Most of the early effort concentrated on the behavior of dislocations in single crystals of a relatively few substances, particularly those having the cubic rock salt structure. More recently the field has broadened considerably to include a wider range of single crystal ceramic materials and the earlier work on the rock salt structure has been extended to include the effects of microstructure.

In this paper the influence of microstructure on the following aspects of mechanical behavior will be considered in turn, (1) elastic deformation, (2) anelastic behavior, (3) plastic deformation, (4) brittle fracture, (5) high temperature deformation and creep. In addition to the familiar variables such as grain size and the presence and distribution of porosity or a second phase, the term microstructure will be considered broadly enough to allow discussion of the role that fundamental variables such as crystal structure, bond character and crystalline defects such as impurities, vacancies and dislocations play in determining mechanical behavior. By necessity the paper is concerned almost exclusively with the simple oxide ceramics since these materials have been the most extensively studied.

2. Elastic Deformation

Purely elastic deformation of a single crystal corresponds to the variation in spacing between atoms under stress. Thus, elastic extension is directly related to the forces between atoms and the binding energy of the structure. Similarly the elastic modulus, the ratio of stress to the extension it produces, is related to bond strength and character. A simple way in which this correlation may be appreciated is to consider the elastic moduli of a number of materials as a function of their melting temperature. The points all fall within a fairly narrow band for which the elastic modulus increases as the melting point increases [4]. Materials of similar type and structure fall in a much narrower band.

[1] Figures in brackets indicate the literature references at the end of this paper.

The principal effects of microstructure on elastic modulus arise through the presence of a second phase. There are a considerable number of theoretical analyses relating the elastic modulus of heterogeneous systems to the amount of second phase. Each calculation leads to a slightly different relationship enjoying a different degree of success in describing the experimental results. In the simplest case, where the bond between the matrix (the continuous phase) and the inclusions remains continuous and the two phases have the same value for Poisson's ratio, the resultant modulus (E) is given by the simple relationship:

$$E = E_o(1-c) + E_1 c.$$

or

$$E = E_o - c\,(E_o - E_1) \tag{1}$$

where E_o is the modulus for the matrix, E_1 is the modulus for the included second phase, and c is the volume fraction of the second phase. This gives a linear relationship between the modulus of the two end components as indicated in figure 1.

In general the elastic modulus of a two-phase solid does not vary linearly and the value is always less than that predicted by the linear relationship. Probably the most successful analyses for predicting the modulus of heterogeneous solids are the recent ones by Paul [5] and Hashin [6] and the modification to Hashin's analysis by Hasselman and Shaffer [7]. These authors consider the more general case where values for Poisson's ratio of the two phases are not the same and examine the influence of particle shape. Both Paul [5] and Hashin [6] used the system tungsten carbide-cobalt investigated by Nishimatsui and Gurland [8] and others for verification of their equations, obtaining good agreement with experiment. In later work, Hasselman and Shaffer [7] and Hasselman [9] applied these equations to their measurements on the variation of elastic modulus for zirconium carbide containing graphite. These results are reproduced in figure 1, where it appears that Hashin's equation, in particular the lower boundary, shows the best agreement. The equations for shear or bulk modulus derived by Hashin [6] can be written in the general form:

$$E = E_o - c(E_o - E_1)\,\frac{A\,E_o}{E_o + B[E_1 + (E_o - E_1)c]} \tag{2}$$

where $A = B + 1$ is a numerical constant.

For the case where the second phase is porosity, i.e., $E_1 = 0$, equation (2) reduces to

$$E = E_o\left[1 - \frac{PA}{1+BP}\right] \tag{3}$$

where P is the porosity. Other simplified theoretical relationships for the dependence of modulus on porosity are

$$E = E_o\left[1 - 1.9P + 0.9P^2\right] \tag{4}$$

when γ (Poisson's ratio) = 0.3 derived by MacKenzie [10] for an elastic solid containing spherical holes and

$$E = E_o\left[\frac{1 - P^{2/3}}{1 + P - P^{2/3}}\right] \tag{5}$$

derived by Paul [5] for a solid containing holes of cubic shape. Pores of both shapes can be seen in a ceramic body depending upon their location and the crystal structure. The equation due to MacKenzie has been applied by Coble and Kingery [11] to their measurements on sintered alumina with excellent agreement.

In addition, the relationship:

$$E = E_o e^{-kp} \qquad (6)$$

where k is a numerical constant, has been devised on a purely empirical basis by Murray et al.[12], to describe experimental results on the effect of porosity on the modulus of beryllium oxide. A similar relationship for alumina was suggested by Spriggs[13], and investigated by Knudsen[14] who accumulated all the available data on this material and showed that the exponential relationship gave a very adequate representation out to 40% porosity with k = 4. Spriggs et al.[15] have also used it for magnesia containing up to 25% porosity; their results are reproduced in figure 2. Use of the empirical exponential relationship in equation (6) has been criticized by Hasselmann[16] on the grounds that it does not have any fundamental basis and does not satisfy the boundary condition E = 0 when P = 1, he suggests that equation (3) due to Hashin[6] can be used with equal success and is more flexible.

In fact the exponential function when expanded takes on a form similar to equation (4) apart from the numerical factor which depends on k. All of the equations (3) through (6) give a fairly adequate representation of the modulus dependence on porosity and it is difficult to make a critical choice among them. Obviously the microstructural variables from specimen to specimen make it virtually impossible to define a practical ceramic in terms of a mathematical model. It is highly probable that the size, shape and location of the pores as well as the total porosity governs the success of any particular equation.

Other microstructural parameters such as grain size or texture have little or no effect on the elastic modulus. In their studies on alumina and magnesia, Spriggs and Vasilos[17] found the dynamic modulus to be relatively insensitive to variations in grain size for specimens having the same porosity. Although no specific studies have been made, the major effects of texture (alignment of the grains in an extruded body for example) are to be expected in those materials of non-cubic crystal structure possessing strongly anisotropic elastic constants.

In conclusion, it may be stated that for purposes of mechanical strength and rigidity the maximum elastic modulus is generally desirable and this is obtained in material of the highest density, in structures where the solid phase is continuous and the pores are closed and spherical.

3. Anelastic Behavior

When a stress is applied to a body in the elastic region it does not necessarily come to equilibrium immediately but approaches the total strain value asymptotically with time. This so-called "anelastic" effect[18] becomes particularly important when a periodic stress is applied since the resulting hysteresis loop causes energy to be dissipated by the solid.

The magnitude of the energy dissipated at a particular temperature, generally referred to as the internal friction, depends on the strain amplitude and frequency of the imposed vibrations. With the amplitude constant, the internal friction goes through a maximum when the frequency is varied, as shown in figure 3. The time interval at this critical frequency corresponds to the relaxation time for the particular process responsible for the peak. At the same frequency, the dynamic elastic modulus changes discontinuously, increasing as the frequency is raised through the critical range because the relaxation process then has insufficient time to contribute to the "elastic" strain. This is also illustrated in figure 3. For experimental purposes it is generally more convenient to use the natural frequency of a specimen and to vary its temperature. In this case the internal friction goes through a peak at a characteristic temperature and there is usually an accompanying inflexion in the dynamic modulus versus temperature curve. By studying the displacement of the peak along the temperature scale for different specimen frequencies it is possible to estimate the activation energy for the relaxation process.

Studies of the internal friction spectrum as a function of temperature, strain amplitude and microstructure have provided powerful research tools for understanding internal structure and atomic movements in solids. But internal friction is also important from a practical viewpoint in that it constitutes the damping capacity of a freely vibrating solid; depending on the particular application, one may desire either a very high or a very low rate of damping. In the remainder of this section we will review briefly the effect of microstructure on the internal friction, or damping capacity, of ceramics.

The most important microstructural effect is that associated with the presence of grain boundaries. Figure 4 due to Chang [19] shows the difference in internal friction between monocrystalline and polycrystalline alumina as a function of temperature. The internal friction peak at 1100°C is observed only in the polycrystalline material and has been attributed to grain boundary sliding by Wachtman and Maxwell [20] and Chang [19]. Correspondingly Wachtman and Maxwell [20] have shown that the dynamic elastic modulus drops off in value very rapidly at this temperature due also to intergranular relaxation. By measuring the shift in the peak for different frequencies, Chang [19] was able to measure the activation energy for this relaxation process. The value, 200 K cals/mole, agreed fairly well with other measurements obtained from creep studies (see later) and the activation energy for self-diffusion of aluminum or oxygen ions in alumina. The implication was that the internal friction peak corresponded to diffusion controlled grain boundary sliding.

The grain boundary relaxation peak in alumina has been the subject of extensive investigation, particularly into the effect of purity. Conventional alumina shows the peak around 1100°C, but for high purity alumina it has been reported as high as 1400°C [21]. The deliberate addition of impurity lowers the temperature of the internal friction peak at a given frequency considerably. Figure 5, taken from the work of Crandall et al. [22], shows how the addition of just 1% SiO_2 introduces a new peak around 700°C. Similarly, the addition of small amounts of Cr_2O_3 or La_2O_3 result in the appearance of internal friction peaks at lower temperatures [19,23]. Also, the addition of 1% MgO has been shown to increase the damping capacity of beryllium oxide at low temperatures [23]. The general interpretation is that impurities tend to enhance grain boundary sliding in ceramic materials, a phenomenon the opposite to that normally observed in metals. The reason for the lower viscosity is not fully understood, it may be associated with the precipitation of a complex or glassy phase in the grain boundaries or it may be associated with the introduction of a non-equilibrium concentration of vacancies necessary to maintain electrical neutrality when impurity ions of a different valence are added. Obviously, the damping capacity of ceramics at low temperature is exceedingly sensitive to purity.

Other microstructural features are known to be responsible for internal friction peaks in solids. These include, stress induced phase tranformations, stress induced ordering, and relaxation phenomena associated with the presence of incoherent interfaces (inclusions) and the motion of twin interfaces [24]. While these processes have been studied extensively in metallic solids there has been little research in this area on ceramic systems. Chang [23] has suggested that an internal friction peak observed in zirconium hydride around 100°C may be due to twin interface motion.

Another microstructural effect on internal friction at low temperatures is that associated with defects introduced by plastic deformation. Again this is a field which has been investigated primarily in metals [24] and internal friction peaks due to dislocation motion (the so-called Bordoni peak) have been identified. Of the ceramic materials, sodium chloride has been studied in most detail [25,26], although a limited amount of work has been done on lithium fluoride [27], magnesia [28,29] and alumina [29]. In general the damping increases with the amount of plastic deformation and is observed so long as the dislocations are mobile. Thus procedures to lock dislocations by heat treatment or X-irradiation [25] result in a decrease in the damping capacity. The effect of plastic deformation on the internal friction spectrum of magnesium oxide is illustrated in figure 6. In this material plastic deformation enhances the damping capacity around room temperature. The equivalent dislocation damping peak is not observed in alumina until around 1500°C and, as Chang [29] has pointed out, this difference in behavior is a reflection of the relative dislocation mobility in these two solids (see later). In this respect the damping capacity of a single crystal at a certain temperature is influenced by its crystal structure, and similarly the damping capacity may be regarded as a useful indicator as to whether dislocations are mobile in a particular solid at a given temperature or not.

4. Plastic Deformation

Plastic deformation in crystalline solids at low temperatures (ie. $<0.5T_m$) is due to the generation, motion, and multiplication of dislocations. The previous seminar in this series [30] has dealt with some of the more sophisticated aspects of dislocation theory and dislocation interactions in crystalline solids. However, it is important to emphasize here that the properties of dislocations in ceramics are quite different from those in metals. The reasons for this are the short range nature of the bonding forces, the presence of two or more ion species of different size and a more complicated crystal structure. Furthermore, the behavior of dislocations differs from one ceramic material to another and it is dangerous to generalize between them. In this section we shall be concerned with the influence of structural and microstructural elements on the availability and mobility of dislocations and thus on the plastic properties of ceramic materials.

4.1. Single Crystals

4.1.1. Crystal Structure and Bond Character

A dislocation line represents the boundary line between slipped and unslipped portions of a crystal plane. The direction in which slip occurs and the plane selected depend on crystallographic factors, the primary factor being that the slip (or Burgers) vector should correspond to the shortest displacement resulting in crystalline identity. The slip plane is generally the closest packed plane. However, in purely ionic solids there is the additional restriction that displacement should occur in a direction or over a plane which does not cause like ions to be forced into juxtaposition at any stage of the displacement. It is for this reason that magnesium oxide slips in the [110] direction over {110} planes rather than the more densely packed {001} planes [31]. For similar reasons the slip direction of caesium chloride type crystals changes from [111] to [100] as the bonding changes from metallic to ionic in nature [32]. Thus bond character is important in determining the slip elements.

Crystal structure also plays a very important role in determining the dislocation configuration, in general the more complex the crystal structure, the more complex the dislocation configuration. Consider alumina for example: the shortest direction of crystalline identity is a $[11\bar{2}0]$, but as Kronberg [33] has shown, it is energetically favorable for this displacement to be achieved in a series of four shorter displacements where the ions ride through the saddle points in the structure. The passage of one of these shorter displacements, or partial dislocations, results in the formation of a planar stacking fault. Thus dislocations in alumina should consist of four partial dislocations linked by three stacking fault layers. Dislocations in the basal plane of the layer silicates similarly dissociate into four partials and this has been observed directly in talc by the electron transmission technique [34,35]. Stacking faults linking partial dislocations have been observed directly in a number of other layer structures [34,35], and in rutile [36]. In magnesium oxide the structure is relatively simple and the dislocations can be thought of as being made by the insertion of two supplementary (110) surfaces of positive and negative ions. The two surfaces are necessary to maintain charge balance and they must remain adjacent to maintain continuity. Any tendency for them to dissociate would force like ions into juxtaposition and consequently form a very high energy stacking fault.

The combined influences of bond character and crystal structure have their greatest effect on the relative mobility of dislocations in various ceramic materials. When a dislocation moves, bonds, ionic and covalent, must be broken and remade and in the case of dissociated dislocations the partials must also be moved along together. While the breaking of bonds due to the movement of dislocations is a relatively low energy process in metals, in covalent solids it can be very high. The situation is further complicated in alumina, for example, by the fact that when the dislocation moves the aluminum ions and oxygen ions in the dislocation core must move in different directions, referred to by Kronberg [33] as "synchro-shear". Only at high temperatures where ion mobility is high and the motions easy to synchronize can dislocations move easily in alumina. It is for this reason that it is necessary to go to extremely high stresses or high temperatures [37,38,39] (greater than 1000°C) to observe plastic deformation in single crystals of this material. It also explains the strong temperature dependence of the yield strength of alumina [39]. In the case of rutile the movement of dislocations requires the rupture of predominantly covalent bonds and this probably explains the inability of this material to deform plastically below 600°C [36]. By contrast the predominantly ionic nature of the bond and the relative simplicity of the dislocation configuration in magnesium oxide makes it possible to deform this material even at liquid nitrogen temperature.

As mentioned earlier, the difference in dislocation mobility between alumina and magnesia is reflected by their relative damping capacity [29], it is also responsible for many of the other contrasting features of their mechanical behavior as we shall discuss in the following sections. Similarly, the effects of microstructure on the mechanical properties of other ceramic materials at a given temperature are conditioned by the relative ease with which dislocations can move.

It is important to realize that the conventional yield strength of a solid corresponds to a stress level at which large numbers of dislocations are moving with quite a high velocity. The plastic strain rate of a crystal may be written as:

$$\dot{\varepsilon} = n\, b\, v \qquad (7)$$

where n is the number of mobile dislocations per unit area, a factor which increases rapidly due to dislocation multiplication [40]; b is the Burgers vector; v is the average velocity of the dislocations, a factor which is very sensitive to the local stress. Direct measurements of the velocity-stress dependence by Johnston and Gilman [41] have shown that the velocity of dislocations in lithium fluoride increases approximately as the twenty-fifth power of the stress. Macroscopic yielding occurs when $\dot{\varepsilon}$, equation (7), is approximately equal to the imposed strain rate of the testing machine. With sensitive techniques however, it is possible to detect plastic deformation well below the conventional yield strength in the so-called microstrain region. In particular etch pit techniques [42] can be used to measure the stress required to get dislocations moving. This stress is defined as the microscopic yield stress.

Thus, to summarize, the plastic properties of a solid depend critically upon the number of dislocation sources (n) and the mobility of dislocations (v). Dislocation mobility is influenced fundamentally by bond character and crystal structure. All of these parameters must be borne in mind when considering the extra effects due to microstructure.

4.1.2. Solid Solution and Precipitation Hardening

First, we discuss the effects due to impurities. Impurities can be present either in solid solution or in the form of precipitate particles and can act in two main ways to change the plastic properties of a crystal. First, they can lock dislocations in place, preventing them from participating in plastic flow and thus reducing the initial value of n in equation (7); and second, they can impede the motion of dislocations through the crystal lattice and thus reduce v in equation (7). Either way the crystal increases in strength.

The most direct example of dislocation locking by impurity is that demonstrated by Stokes [43] on magnesium oxide single crystals. He showed that crystals specially treated to contain only "aged" or "grown in" dislocations supported stresses as high as 140,000 psi in a purely elastic manner without yielding. In this case all of the dislocations were immobilized and n in equation (7) was zero at all stress levels. On the other hand, crystals containing "fresh" dislocations (ie. dislocations generated at the surface at room temperature and therefore free from any contamination by impurity) deformed plastically at a yield stress of approximately 10,000 psi. The "fresh" dislocations could move and multiply fast enough at this stress level for the plastic strain rate ($\dot{\varepsilon}$) to keep up with the testing machine. Similar differences in mechanical behavior between crystals containing "fresh" and "aged" dislocations, although on a less spectacular scale, have been noted in lithium fluoride by Gilman and Johnston [2].

"Grown in" dislocations in magnesium oxide have been observed directly by the electron transmission technique and are found to have precipitate particles strung all along their length [44] as illustrated in figure 7. The particles have been identified as zirconium dioxide [45], although considering the purity of the crystals there are likely to be other oxides precipitated on the dislocations too. The mechanism by which these particles lock the dislocations is not entirely understood, but it probably involves an elastic interaction between the impurity ions and the stress field of the dislocations.

One of the characteristic features of impurity locking is that it represents a metastable condition. As soon as a single dislocation escapes from its impurity environment it can move and multiply rapidly and the stress level needed to sustain the imposed strain rate falls. Such catastrophic drops in strength at the onset of yielding have been observed in magnesium oxide [43].

The great difference in mechanical behavior between these two conditions in magnesium oxide has proved to be extremely useful in understanding the origin of brittle fracture in polycrystalline material. We shall return to this point later in connection with table 2.

It is now generally agreed that the permanent strengthening associated with impurities must arise from an increased resistance to dislocation motion through the lattice, ie., by decreasing the velocity v for a given stress [46]. Local fluctuations in the internal stress field due to the presence of impurity ions impede the dislocations and cause the strengthening. Although the exact differences between solid solution and precipitation hardening are by no means well understood, the stresses due to a coherent precipitate are generally regarded as a much more effective impediment than those due to impurities in solid solution. However, the situation is further complicated in ionic solids by the requirement that electrical neutrality must be maintained at all times and the valency of impurity ions going into solid solution must be taken into consideration. There are, therefore, at least three conditions to be considered, (i) simple solid solution with ions of the same valency, (ii) simple solid solution with ions of different valency, (iii) precipitation.

When the valency of the added impurity ion is the same as that of the ion it is replacing, simple solid solution strengthening is observed. This has been observed in silver chloride, for example, hardened by the addition of silver bromide [47] and in potassium chloride hardened by the addition of potassium bromide [48]. The stress strain characteristics of silver chloride-sodium chloride alloys [49] are compared with the phase diagram in figure 8 and simple solid solution strengthening is observed at the two extreme ends (i.e., up to 10 mole percent and above 85 mole percent sodium chloride) of the composition scale.

When the valency of the added impurity ion going into solution is different from the ion it is replacing, then an equivalent number of vacancies must be introduced into the host lattice to maintain electrical neutrality. This condition has a remarkable strengthening effect. The influence of divalent alloying elements on the mechanical properties of sodium chloride was studied extensively in Germany in the early 1930's and this work is reviewed in the book by Schmid and Boas [50]. While the solubility of divalent cations is very restricted, marked hardening is observed for additions in the range 10^{-6} to 10^{-4} mole fractions. Thus, 0.02% calcium chloride in sodium chloride raises the strength fivefold. Similarly, the addition of minute quantities of magnesium fluoride to lithium fluoride result in a tenfold increase in strength [51]. Eshelby et al [52] have proposed a mechanism to account for this strengthening in which they take into consideration the electrostatic attraction between charged dislocations and the charged vacancies, so that the dislocation lines become surrounded by a vacancy cloud which restricts their motion. Other evidence concerning the role of vacancies and point defects in the strengthening of ionic solids is reviewed in the paper by Pratt [53].

There are very few clear cut examples of precipitation hardening in ceramic systems. The best example to date is that observed in the middle composition range of the sodium chloride-silver chloride system illustrated in figure 8. Sodium chloride-silver chloride alloys show a miscibility gap between 10% and 80% sodium chloride at room temperature and in this same range the strength increases by 50 to 100-fold over that of the end components [49]. However, even in this system rules of precipitation hardening are not strictly followed in that solution heat-treated crystals are equally as strong as fully precipitated crystals, and it is not certain whether internal stresses due to co-precipitation of the two equilibrium phases are the true source of hardening or not.

As a result of their studies on the effect of heat treatment and temperature on the strength of commercial magnesium oxide crystals, Gorum et al. [54], May and Kronberg [55] and Stokes [56] concluded that a precipitation hardening type of mechanism was occurring. Crystals in the as-received (fully precipitated) condition containing many "fresh" dislocation sources were approximately twice as strong as those annealed above 1200°C, as shown in figure 9 curve A; however, the higher strength could be restored by a subsequent anneal around 800°C, figure 9 curve B. Presumably the anneal above 1200°C dissolved the precipitate particles initially present into solid solution making it easier for the dislocations to move at room temperature. The subsequent anneal at 800°C forced them to reprecipitate again. Unfortunately, this work is currently lacking direct experimental evidence concerning the nature and distribution of the second phase.

Deliberate alloying of magnesium oxide single crystals with small quantities of impurity can lead to remarkable changes in strength, although the strengthening mechanism, i.e., whether due to solid solution, precipitation or point defect hardening, has not yet been identified. Satkiewicz [57] showed that single crystals doped with 0.5% Cr_2O_3 raised the compressive strength fivefold to 80,000 psi, a value which dropped by one-half on subsequent vacuum annealing. Liu et al [58] have found a similar strength (80,000 psi) for magnesia containing a few mole percent of MnO, and a strength of 40,000 psi for alloys containing only five mole percent NiO. In the latter case microscopic studies indicate that the nickel ions are in solid solution. There is a need for further work in this area with emphasis on the control of stoichiometry, and the manipulation of microstructure through heat treatment based on complete phase diagrams.

4.2. Polycrystals

Next, we consider the effect of grain boundaries on the plastic deformation of ceramic materials. As was pointed out many years ago by von Mises [59] and by Taylor [60], for a fine grained polycrystalline solid to undergo plastic deformation each of the individual grains must be capable of a perfectly general change in shape. To satisfy this condition, each of the crystalline grains must possess five <u>independent</u> slip systems. If not, then voids are likely to develop within the solid where the individual grains cannot conform to the change in shape of their neighbors. Groves and Kelly [61] have recently examined the observed crystallographic slip systems for a number of common ceramic materials to determine whether they allow the required general change in shape or not. Their results, reproduced in Table 1, are most interesting. They find that <u>none</u> of the common ceramic materials is capable of a great amount of plastic deformation at low temperatures (we shall discuss the high temperature case later).

TABLE 1. <u>The number of independent slip systems for some common ceramic crystal structures</u>

Structure	Crystallographic Slip Systems	Number of Independent Systems
NaCl (Low Temperatures) (eg. MgO)	$\{110\}\ \langle 1\bar{1}0\rangle$	2
NaCl (High Temperatures) (eg. MgO)	$\{110\}\ \langle 1\bar{1}0\rangle$ and $\{001\}\ \langle 1\bar{1}0\rangle$	5
Hexagonal (eg. Graphite, Al_2O_3)	$\{0001\}\ \langle 11\bar{2}0\rangle$	2
CsCl	$\{100\}\ \langle 010\rangle$	3
CaF_2 (Low Temperatures) (eg. UO_2)	$\{001\}\ \langle 110\rangle$	3
CaF_2 (High Temperatures)	$\{001\}\ \langle 110\rangle$ and $\{110\}\ \langle 1\bar{1}0\rangle$	5
TiO_2	$\{101\}\ \langle 10\bar{1}\rangle$ and $\{110\}\ \langle 001\rangle$	4

One of the consequences of this failure to satisfy the von Mises criterion is demonstrated by the marked effect of grain size on the plastic properties of ionic solids at low temperatures. Figure 10 reproduces stress strain curves obtained on polycrystalline sodium chloride at room temperature [62]. As can be seen, decreasing the grain size has a comparatively small effect on the proportional limit, but a very large effect on the rate of work hardening. By the time there are three to five grains in the cross-section, the rate of work hardening has increased tenfold over that of the cubic orientation single crystal and for the finest grain size tested (.035 mm) it has increased thirtyfold over the single crystal. Similar effects have been found in polycrystalline silver chloride [63] and lithium fluoride [64] at low temperatures.

These observations may be interpreted as follows:

(i) Since "grown in" sources are not completely immobilized in these ionic solids there are plenty of sources for slip over $\{110\}$ planes. The stress to start these dislocations moving is relatively insensitive to grain size. In fact the slight dependence noted in figure 10 would probably disappear with the use of higher sensitivity microstrain techniques.

(ii) As slip propagates and the whole polycrystalline matrix attempts to deform plastically, constraints develop at the grain boundaries due to the fact that there are only two independent slip systems (table 1). Consequently the material as a whole cannot deform plastically and hardens at a rate almost determined by the elastic constants.

(iii) As the stress increases the constraints can be relaxed somewhat by local slip on additional systems. In particular slip on $\{001\}\langle 1\bar{1}0\rangle$ has been observed in the vicinity of grain boundaries in polycrystalline lithium fluoride at room temperature as shown in figure 11. This additional slip permits the small amount of plastic deformation observed in the stress strain curves of figure 10. Unfortunately the applied stress required to promote general slip throughout a grain on this $\{001\}\langle 1\bar{1}0\rangle$ system is far too high, for example in sodium chloride it is four times [65] and in lithium fluoride at least eight times [66] the stress to promote slip on the $\{110\}\langle 1\bar{1}0\rangle$ system at room temperature. Consequently the material as a whole cannot deform plastically by any great amount at least until the applied stress reaches this level.

(iv) The actual rate at which the stress increases, i.e. the rate of work hardening, is dependent on the grain size since the smaller the grain size the greater the grain boundary surface area and the greater the volume of constrained material wherein shear cannot take place. The exact relationship between grain size and the rate of work hardening under these conditions has neither been considered theoretically nor determined experimentally.

The situation in magnesium oxide is even worse than in the simple halides. The stress to promote slip on the $\{001\}\langle 1\bar{1}0\rangle$ system at room temperature is approximately one hundred times higher than that to cause slip on the $\{110\}\langle 1\bar{1}0\rangle$ system [67] so that even local deformation of the kind illustrated in figure 11 cannot be expected until extremely high stresses are reached. Thus, polycrystalline magnesium oxide shows virtually no plastic deformation at room temperature even though dislocations are quite mobile and the equivalent single crystals ductile. At higher temperatures the difference in stress level for slip on the two systems is reduced and at 1000°C is down to a factor of ten, equivalent to the situation in lithium fluoride at room temperature. A slight amount of plastic deformation has been observed in compression in this temperature range [67].

Again it must be emphasized that this discussion does not really apply to the low temperature mechanical behavior of ceramic materials in which dislocations are immobile (eg. Al_2O_3, TiO_2, TiC, etc. at room temperature). In these materials the lattice resistance to dislocation motion is so high that the cohesive strength of the crystalline planes is exceeded before any plastic deformation is possible. The extent to which it may apply at high temperatures when these materials become plastic will be considered later in section 6.

5. Brittle Fracture

In most of the preceding sections attention has been drawn to the plastic properties of ceramic materials, yet the fact remains that the most notorious mechanical property of a ceramic, particularly at low temperatures, is its brittleness. The strength of a ceramic is always limited by brittle fracture. In this section we shall examine some of the aspects of brittle fracture in ceramics and shall show that in many instances the fracture strength can be related to the plastic properties described so far.

It is well known that the fracture strength of a brittle material falls far short of the theoretical strength (E/10) expected from simple estimates of interatomic forces. Equally familiar is the work of Griffith [68] who showed that the critical tensile stress (σ) to propagate a crack of length c is given by;

$$\sigma = \sqrt{\frac{E\gamma}{c}} \tag{8}$$

where E is Young's modulus and γ the surface energy of the fractured faces. It is important to realize that equation (8) applies specifically to propagation in a purely elastic medium and assumes the pre-existance of cracks. It was for these reasons that Griffith was so successful in applying equation (8) to the strength of glass fibers, since, in glass, surface flaws are nucleated spontaneously by chemical reaction with the environment.

The nucleation, growth, and propagation of brittle fracture in crystalline solids is a vastly more complicated phenomenon. In the absence of pre-existing surface or internal defects a crack nucleus must be generated in some way and it has now been clearly demonstrated in a number of ceramic materials that crack nucleation can occur as a direct consequence of the limited amount of plastic deformation which precedes fracture [30,69]. However, the cracks nucleated by these various mechanisms are often too small to propagate catastrophically under the existing applied tensile stress and either the stress must increase or the cracks must grow to reach the critical dimension. Again it has been found that crack growth is assisted by local plastic deformation [70,71]. When finally the crack reaches the critical dimension the condition for propagation is dictated by a modified form of the Griffith equation due to Orowan [72];

$$\sigma = \sqrt{\frac{E(\gamma+\gamma_p)}{c}} \tag{9}$$

where γ_p represents the energy consumed by plastic deformation in the highly stressed region ahead of the propagating crack. This term γ_p is particularly important since its magnitude determines whether the solid is ultimately brittle or not. When γ_p is large a crack may be stalled for an indefinite period but when γ_p is small propagation may proceed without resistance. The value of γ_p is strongly dependent on the plastic properties of the solid. For most ceramic materials γ_p is inherently small and they are naturally brittle materials. Since much cannot be done to remedy this latter situation most of the attention in ceramics has been focussed on the early stages of fracture. In particular fracture nucleation has been studied intensively and is probably the stage where improvements in the fracture characteristics are most likely to be implemented. Next, we shall discuss the role of structure and microstructure in the nucleation of brittle fracture in ceramics.

5.1. Crack Nucleation Due to Slip at Grain Boundaries

Crack nucleation has been studied most extensively in magnesium oxide. The essential feature is that cracks nucleate wherever groups of dislocations are obstructed either by other slip bands [73,74] or by grain boundaries [75,76,77,78]. The primary reason why these observations can be made so readily in magnesium oxide is that shear occurs at room temperature over flat {110} planar surfaces in discreet slip bands. Thus the deformation is distributed very inhomogeneously and when a slip band is blocked by a microstructural barrier, such as a grain boundary, the stress concentration due to the dislocation pile up [79,80] cannot be dissipated by secondary slip in the surrounding material. Instead a crack forms. Figure 12 shows a cleavage crack generated where a slip band intercepts the grain boundary in a magnesium oxide bi-crystal under compression. Under tension such a cleavage crack switches into the intergranular surface and propagates immediately for fracture [78].

There are two possible ways to prevent the crack nucleation event recorded in figure 12. Either slip within the grains should be made more homogeneous to relax the local stress concentration at the tip of the dislocation pile up or slip should be avoided altogether.

Efforts to make shear homogeneous have indeed resulted in a considerable improvement in the ductility of magnesium oxide single crystals [74] but similar attempts with bi-crystals and polycrystalline material have not been successful [78]. There are a number of reasons for this but the most general and important one for the present discussion arises from the fact that there are only two independent slip systems as indicated in table 1 [61]. Even when homogeneous slip does occur the high stresses developed in the boundary regions due to the incompatability of the grains eventually exceeds the intergranular strength at certain points causing cracks to open up and the specimens to fracture. It is significant that the source of fracture under these conditions is always intergranular [62]. Thus in polycrystalline sodium chloride and lithium fluoride at room temperature, where slip is homogeneous and there is some measurable plastic deformation (see figure 10) brittle fracture always originates from an intergranular source.

On the basis of these observations Stokes and Li [62,78] have concluded that the ability of magnesium oxide, or any other ceramic material for that matter, to slip at low temperatures is in fact an undesirable feature, and they have shown how the fracture strength of fully dense magnesia may be improved when steps are taken to eliminate slip.

Table 2 summarizes recent results comparing the strength of polycrystalline magnesia in the presence and absence of active slip sources [78]. The tensile fracture strengths quoted in the right hand column represent the strength when "fresh" dislocation sources (introduced by the simple expedient of sprinkling the surface with fine silicon carbide powder [42]) are known to be present; the left hand column represents the strength when all possible precautions have been taken to remove surface dislocations by a chemical polish. It is instructive first to compare the fracture strength of bi-crystals with the yield strength of single crystals under the two extreme conditions discussed earlier in connection with dislocation locking (section 4.1). The extremely high fracture strength of the bi-crystal obtained in the absence of slip (compare results 1 and 3) and the close agreement between the fracture strength and yield strength when slip sources are present (compare results 2 and 4) indicate that it is not the presence of the grain boundary per se but the interaction of slip with it which is responsible for the low fracture strength of the bi-crystal in result 4.

TABLE 2. Tensile strength of magnesium oxide in the absence and presence of "fresh" surface dislocations

Result	Material	Tensile Strength	
		"Fresh" Dislocations ABSENT	"Fresh" Dislocations PRESENT
1	Single Crystal	140,000 psi	
2	"		10,000 psi
3	Bi-Crystal	110,000 psi	
4	"		8,000 psi
5	Fully Dense (100%), As-received Hot Pressed Polycrystalline (Grain size 20μ)	28,000 psi	
6	"		18,500 psi
7	Fully Dense (100%), Annealed, Hot Pressed Polycrystalline (Grain size 75μ)	19,500 psi	
8	"		15,000 psi
9	99.7% Dense, As-received, Hot Pressed Polycrystalline (Grain size 30μ)	12,000 psi	
10	"		9,000 psi
11	99.7% Dense, Annealed, Hot Pressed Polycrystalline (Grain size 50μ)	11,500 psi	
12	"		12,500 psi

When similar care is taken to eliminate "fresh" dislocations from the surface of fully dense (100%) fine grained polycrystalline magnesia the tensile strength can be increased markedly, exceeding 30,000 psi in some cases. Again the average value (28,000 psi, result 5) for such specimens drops down to 18,500 psi when dislocations are reintroduced into the surface. It is believed that this remarkable surface sensitivity is due to the fact that fracture originates in these fully dense polycrystalline magnesia specimens by the slip dislocation mechanism of figure 12.

Obviously this discussion of slip interaction with grain boundaries applies only to those solids in which dislocations can move easily at low temperatures. The extreme sensitivity to surface condition described in the previous paragraph is not likely to be found in materials such as alumina or rutile. The effect of surface damage on these materials will be discussed later.

5.2. Effect of Porosity and Grain Size

When just a slight amount of porosity is present the magnitude of the difference in strength in Table 2 due to the presence or absence of surface dislocation sources is much less. For example, annealing the fully dense hot pressed material at 2000°C causes grain growth and the appearance of slight residual porosity in the grain boundary interface. The strength of polished material is then reduced to 19,500 psi (result 7) and drops further only by one quarter (to 15,000 psi, result 8) when surface dislocations are introduced [78]. In more conventional material of lower density (99.7%) the tensile fracture strength is much lower (12,000 psi) and the value is then apparently independent of surface treatment (results 9 through 12). These observations have been interpreted by assuming that the pores themselves provide stress concentrations which either initiate slip or nucleate intergranular failure directly. Thus, porosity in excess of 0.1 to 0.2% tends to override any effects due to surface dislocations and the brittle fracture strength is more dependent on the amount and distribution of porosity.

It has long been realized that the strength of ceramics is sensitive to porosity and that the greatest changes occur following small departures from theoretical density. Ryshkewitch [81] and Duckworth [82] first demonstrated that the transverse bend strength (S) of alumina, zirconia, and silicate porcelain decreased exponentially with porosity as in equation (10);

$$S = S_o e^{-bp} \tag{10}$$

The form of this equation should be compared with equation (6). It is found experimentally that the value of k is generally one half the value found for b. A similar dependence has been established for thoria [83], uranium dioxide [84], and magnesia [85]. While the empirical relationship holds quite well when the porosity exceeds 0.3%, for values less than this the strength is determined by other variables. In particular equation (10) makes no allowance for the distribution and location of pores. It is to be expected that the stress concentration effect will depend critically upon whether the pores are interconnected (open) or isolated (closed) in any particular intergranular region at low porosity.

Similarly it is well known that decreasing the grain size increases the strength of a ceramic material. Knudsen [83] has suggested that the combined effects of grain size (d) and porosity (p) can be represented by equation (11);

$$S = S_o d^{-a} e^{-bp} \tag{11}$$

The value of a varies from 1/2 to 1/3 for a variety of materials and the equation has been found adequate to describe results of thoria [83], uranium dioxide [84], magnesia [85] and alumina [22,85,86] and for beryllium oxide [87] with a = 1.

Unfortunately most of this data on the transverse bend strength of ceramics as a function of grain size and porosity has been obtained on specimens of variable surface perfection. By surface perfection here we do not necessarily mean the presence or absence of surface dislocations considered earlier with respect to magnesia, but gross imperfections in the form of intergranular or cleavage ruptures generated by mechanical preparation techniques. Surface perfection is extremely important, for the presence or absence of flaws determines to a great extent the subsequent mechanical behavior and certainly contributes to the statistical nature of the strength of ceramics [88]. Harrison [89] has emphasized how surface flaws and damage introduced during grinding and lapping operations can lower the strength of polycrystalline magnesia. It follows that the empirical relationship of equation (11) may well represent the stress required to propagate existing surface defects through the microstructure rather than the stress to initiate cracks. In this case when $a = 1/2$, equation (11) corresponds to the Griffith equation (8) with the condition that c is related to the grain size d in some simple manner. In order to determine the effects of porosity and grain size systematically much more attention should be paid in the future to surface condition.

It is not easy to anticipate what the fracture strength dependence on grain size will be in the absence of surface flaws. Certainly it will depend on whether dislocations are mobile or not. When dislocations are mobile then the grain boundary interactions discussed in the previous section are important and the fracture strength dependence on grain size may follow a $d^{\frac{1}{2}}$ relationship of the type developed by Petch and Cottrell [90] for brittle metals. When dislocations cannot move the fracture strength will be limited by internal stresses developed during firing and heat treatment. The internal stresses may be added to the applied stress and will be particularly severe in the boundary regions of anisotropic materials. All in all it seems reasonable to anticipate that the greatest low temperature fracture strengths will be obtained in materials of high density, fine grain size, perfect surface condition, in which dislocations cannot move. It is encouraging to note that transverse strengths in alumina in excess of 100,000 psi can be obtained under these conditions.

6. High Temperature Deformation and Creep

At elevated temperatures, two factors become important to change the dependence of mechanical properties on microstructure. First, dislocations become more mobile on existing slip systems and new slip systems become possible, and second, the diffusion of point defects is enhanced to the point where they begin to contribute to the deformation.

6.1. Plastic Deformation and Ductile Fracture

The increased mobility of dislocations at high temperatures is reflected by a further drop in strength of single crystals of materials such as magnesium oxide [67] which are already plastic at low temperatures. It is also responsible for the onset of plasticity at reasonable stress levels in single crystals of materials like alumina [37,38,39], rutile [36,91], and titanium carbide [92] which are not plastic at low temperatures. For the most part these newly plastic ceramic materials slip on simple systems and the restrictions on polycrystalline ductility discussed earlier still apply.

The possibility of slip on multiple systems has more interesting consequences particularly for materials having the rock salt structure. As indicated in Table 1, slip becomes possible over {100} planes in addition to the {110} planes at high temperatures. The occurrence of {100} slip contributes an additional three independent slip systems, making a total of five, thereby satisfying the condition for polycrystalline ductility. Stokes and Li [62] have shown that polycrystalline sodium chloride undergoes appreciable extension above 150°C, the temperature at which "wavy" or multiple slip is first observed. Under these conditions constraints do not develop in the grain boundary region and brittle fracture does not occur, instead the specimens extend continuously and neck right down to a point, giving a type of ductile fracture. The influence of grain size and porosity on ductile fracture has not been studied in sufficient detail yet to allow any conclusions to be drawn from the behavior of sodium chloride. However, similar work on silver chloride [63] in the temperature range where it exhibits wavy slip has shown that grain size has little or no effect on the rate of work hardening, again consistent with the fact that grain boundary constraints have been completely relaxed.

6.2. Creep and High Temperature Fracture

Unfortunately, the temperature range where a multiplicity of slip systems becomes available in most oxide ceramics is so high that additional complications come into play and the occurrence of plastic deformation by the simple movement of dislocations is never observed. Deformation at elevated temperatures is always enhanced by the diffusion of point defects and by the onset of viscous sliding at grain boundaries. The diffusion of vacancies or interstitial ions contributes to each of the three basic processes considered responsible for creep; dislocation climb, vacancy migration under stress, and grain boundary sliding. These will be described briefly in turn.

Dislocation climb occurs when vacant lattice sites condense on or escape from edge dislocations causing them to be displaced vertically in a direction perpendicular to the slip plane. The climb process permits unlike dislocations to move together and annihilate and it also permits dislocations to detour around obstacles in the slip plane. Thus, dislocations trapped in a pile-up against obstacles such as sub-grain or grain boundaries can escape by climb and rearrange themselves, the relaxation of the back stress enables the dislocation source to resume operation and deformation continues. When the rate of dispersion of the dislocations is approximately equal to the rate at which they are pumped into the pile-up a steady state creep rate is established. The rate controlling step in this process is vacancy diffusion, a fact which has been well-established for all metals for which accurate data is available [93]. In a detailed analysis of the climb mechanism, Weertman [94] has shown that the creep rate ($\dot{\varepsilon}$) varies with the applied stress (σ) and temperature (T) according to the following relationship;

$$\dot{\varepsilon} \propto \sigma^{(9/2)} \frac{e^{-U/KT}}{T} \tag{12}$$

where U is generally the activation energy for self diffusion. In ceramics the presence of two ion species having different activation energies for self diffusion and the possibility that diffusion may occur in pairs makes the interpretation of U more difficult.

The remaining creep processes do not involve the motion of dislocations and apply specifically to polycrystalline material. In vacancy migration under stress, deformation results from diffusional flow within each crystal away from those boundaries where there is a high local compressive stress towards those boundaries having a high local tensile stress. This is generally referred to as Nabarro-Herring type creep and it has been estimated by these authors [95,96] that the creep rate is related to the stress, temperature and grain size (d) by;

$$\dot{\varepsilon} \propto \frac{\sigma D}{d^2 T} \tag{13}$$

where D is the diffusion coefficient and

$$D = D_o e^{-U/KT} \tag{14}$$

It should be noted that the relationship for $\dot{\varepsilon}$ in (13) differs from that in (12) by the power of the stress dependence and by the appearance of a grain size term. The linear relationship of $\dot{\varepsilon}$ and σ in equation (13) gives rise to a viscous type of flow, at a rate determined by vacancy diffusion.

The exact mechanism of the third contributor to high temperature creep, grain boundary sliding, is not known. It has been shown that the shear strength of grain boundaries in ionic materials can fall off catastrophically at high temperatures [97,98]. Whether this increased viscosity in the grain boundary region is due to the presence of an impure glassy phase or whether it is controlled by vacancy diffusion or dislocation motion through the disordered boundary region has not been determined. It is important to note that the creep rate due to this process is also roughly proportional to the applied stress but since it is dependent on the grain boundary surface area per unit volume it varies inversely as the grain size, i.e.

$$\dot{\varepsilon} \propto \frac{\sigma}{d} \tag{15}$$

Obviously, all three of these mechanisms occur together, to a certain extent, during high temperature creep. It is possible to distinguish which is the controlling mechanism by measuring the dependence of the creep rate on temperature, stress and grain size as may be appreciated by comparing equations (12) (13) and (15). This procedure is generally followed by workers in the field. There is comparatively little systematic work on the effect of structure and microstructure on the creep of ceramics. Probably the earliest work on this subject is that by Wygant [99] who compared the creep rates of different ceramic materials. Data for materials of similar grain size or porosity at the same temperature and stress level are almost impossible to obtain, but Table 3, compiled by Kingery [4] gives some indication of the effect of crystal structure when most of these other variables have been fixed.

TABLE 3
Comparison of torsional creep rate
for different polycrystalline ceramic materials

Material	Creep Rate at 1300°C 1800 psi (in/in/hr.)
Al_2O_3	0.13×10^{-5}
ZrO_2	3.0×10^{-5}
MgO (hydrostatic pressed, 2% Porosity)	3.3×10^{-5}
MgO (slip cast, 12% porosity)	33.0×10^{-5}
BeO	30.0×10^{-5}
ThO_2	100.0×10^{-5}

The most detailed studies of the effect of microstructure have been conducted on alumina, although even here the agreement amongst workers is varied. Tests have been performed on materials of different purity, porosity and grain size with different methods of loading. However, an attempt to interpret the results in a logical manner will be made with the help of Table 4. First, we compare the work of Rogers et al [100] and Kronberg [39] on single crystals in the temperature range 900-1700°C, (results 1 and 2 in Table 4). Although these tests were performed under different loading conditions, the activation energy for flow in both cases is approximately the same, 85 Kcal/mole. Since in Kronberg's tests the specimens were known to be deforming by simple slip on the basal plane, this may be regarded as the activation energy to initiate dislocation motion, i.e., to operate the synchro-shear mechanism [33] in single crystals.

At higher temperatures (above 1800°C) Chang [101] found single crystals to exhibit steady state creep at a rate dependent upon stress to the power 4.5 as in equation (12), indicating that it was controlled by the dislocation climb mechanism (result 3). The activation energy, 180 Kcal/mole, for dislocation climb, compares fairly well with the activation energy for diffusion of either the aluminum or oxygen ion determined by other means. The steady state creep rate of the alumina crystals was reduced by four orders of magnitude with the addition of 2% Cr_2O_3 as shown in figure 13, but the activation energy for the process remained unchanged. The interpretation here is that the impurity is restricting motion of the dislocations over the slip plane, but does not change the rate at which they can climb.

With the introduction of grain boundaries there is an increase in the creep rate and a change in the creep mechanism from one controlled by dislocation climb to vacancy migration under stress. Studies on high density, fine grained alumina (Lucalox) by Warshaw and Norton [102] and Folweiler [103] illustrate this point. Both find the creep rate to vary linearly with the stress between 1500°C and 1800°C and the activation energy has been measured to be 130 Kcal/mole (results 4 and 5). Similarly Chang [19] has also found a viscous behavior although with a higher activation energy (result 8) in this temperature range. Paladino and Coble [105] have taken these results and estimated the diffusion coefficients (D in equation (13)) using the exact form of the Nabarro-Herring [96] equation. They have then compared them with the self-diffusion coefficient for the aluminum ion determined by independent means. The excellent agreement illustrated in figure 14 confirms that the Nabarro-Herring mechanism is operating and indicates that the diffusion of aluminum ions is the rate controlling process. A similar correlation has now been established between the beryllium ion diffusion coefficient and the creep diffusion coefficient for beryllia [105,106], and between the magnesium ion diffusion coefficient and the creep diffusion coefficient for magnesia at low stresses [107].

Folweiler [103] studied the effect of grain size on the creep rate of Lucalox alumina and found a dependence inversely proportional to the square of the grain diameter, again consistent with the Nabarro-Herring theory as can be seen from equation (13). Thus, large grained material has a higher creep resistance than fine grained material.

At higher temperatures (1800°C-1900°C) and larger grain sizes the creep rate of alumina was found to increase at a rate more rapid than predicted by the vacancy migration theory (results 6 and 7). Warshaw and Norton [102] studied the stress dependence and found it to vary as the fourth power and on this basis suggested that a dislocation climb mechanism was rate controlling; however, in a more recent examination of this accelerated creep, Coble and Guerard [104] have suggested that grain boundary sliding has taken over. Their reasoning is based on the fact that an addition of Cr_2O_3 increases the creep rate even further; an observation also reported by Chang [19] for polycrystalline material (result 8). If dislocation climb is the controlling mechanism, then an addition of Cr_2O_3 should lower the creep rate as observed on alumina single crystals [101] and reproduced in figure 13. If grain boundary sliding is the controlling mechanism then, as is known from anelasticity studies [19,22] (figure 6), the viscosity is lowered by the addition of impurities, and the creep rate should increase consistent with the experimental observations.

These observations on alumina may be summarized briefly as follows; single crystals creep by the dislocation climb mechanism and impurities lower the creep rate; polycrystals creep in the range 1200-1800°C by the migration of vacancies under a stress gradient and above 1800°C by grain boundary sliding, in both cases impurities raise the creep rate. There is a need for further experiments on bi-crystals to determine the stress dependence of grain boundary sliding and the effect of impurities on grain boundary viscosity.

TABLE 4. High temperature deformation and creep of single and polycrystalline alumina

Result No.	Material	Temperature Range	Rate Controlling Deformation Mechanism	Activation Energy Kcal/mole	Author
1	Single Crystal	900-1300°C	Basal Slip	85	Rogers et al. [100]
2	Single Crystal	1200-1700°C	Basal Slip	85	Kronberg [39]
3(a)	Single Crystal	1800°C	Dislocation Climb	180	Chang [101]
3(b)	Single Crystal plus 2% Cr_2O_3	1800°C	Dislocation Climb	180	Chang [101]
4	Polycrystalline Lucalox, High Density, 5-15μ grain size	1600-1800°C	Vacancy Migration	130	Warshaw and Norton [102]
5	Polycrystalline Lucalox, High Density, 5-35μ grain size	1600-1800°C	Vacancy Migration	130	Folweiler [103]
6	Polycrystalline 97% Density, 50-100μ grain size	1600-1800°C	Grain Boundary Sliding	185	Warshaw and Norton [102]
7(a)	Polycrystalline High Density, 100μ grain size	1750-1900°C	Grain Boundary Sliding	280	Coble and Guerard [104]
7(b)	Same as 7(a), plus Cr_2O_3	1750-1900°C	Grain Boundary Sliding	280	Coble and Guerard [104]
8(a)	Polycrystalline	1400-1700°C	Vacancy Migration and Grain Boundary Sliding	200	Chang [19]
8(b)	Same as 8(a), plus 1% Cr_2O_3	1400-1700°C	Vacancy Migration and Grain Boundary Sliding	200	Chang [19]
8(c)	Same as 8(a), plus 0.25% La_2O_3	1400-1700°C	Vacancy Migration and Grain Boundary Sliding	200	Chang [19]

Probably the reason why polycrystalline alumina creeps by the diffusion controlled mechanism rather than by dislocation climb is a consequence of the number of independent slip systems available. There are only two independent slip systems in alumina so long as basal slip predominates (Table 1) and, even taking into account the additional flexibility afforded by climb, polycrystalline material cannot deform by slip without the generation of intergranular constraints. The constraints can be relieved somewhat at high temperatures by the migration of vacancies but will eventually result in the appearance of intergranular voids in the regions of locally high tensile stress. Figure 15 shows the occurrence of grain boundary voids and sliding in polycrystalline alumina deformed at 1600°C. In magnesia, on the other hand, at a sufficiently high temperature and a high enough stress level, wavy slip occurs and recent tests in our laboratory [108] have shown that high density polycrystalline magnesia can be deformed substantially at 2000°C without the formation of intergranular voids. Under these conditions the creep rate might be determined by dislocation climb although this remains to be confirmed. At lower stress levels or slightly lower temperatures, slip in magnesia remains confined to {110} planes and the two independent slip systems are not then sufficient for creep to proceed by slip alone. Coble [107] has recently shown that under these conditions creep is controlled by vacancy migration under stress, although whether intergranular voids then open up remains to be determined. Certainly the high temperature behavior of magnesia as a function of stress, temperature and microstructural variables is a subject for more systematic and detailed investigation. The fact that fully dense material deforms without intergranular separation may make it superior to alumina for certain high temperature applications.

An increase in creep rate with porosity has long been recognized. Wygant [99] showed that the creep rate of a 2% porosity hydrostatically pressed magnesia was approximately one-tenth the creep rate of a 12% porosity slip cast material as shown in Table 3. Coble and Kingery [109] studied the effect of porosity on the creep rate of sintered alumina up to almost 50% porosity; their results are reproduced in figure 16.

At temperatures where the deformation process is controlled by the migration of point defects, it is to be expected that stoichiometry will play an important role. Scott et al [110] showed that stoichiometric uranium dioxide (UO_2) could not be deformed until the temperature reached 1600°C, whereas a deviation in stoichiometry to $UO_{2.06}$ allowed plastic deformation around 800°C. The non-equilibrium cation vacancies are considered to contribute to creep at the lower temperatures. Similarly, Hirthe and Brittain [111] have shown that the activation energy for steady state creep in rutile changes gradually from 63 Kcal/mole at stoichiometric composition to 33 Kcal/mole for reduced material.

7. Conclusions

This paper has attempted to correlate the mechanical properties of ceramics with fundamental microstructural variables. By necessity the discussion is limited to the simple alkali halide and pure oxide ceramics, but from this fundamental background it is to be hoped that a better appreciation of the mechanical behavior of more conventional ceramics can ultimately be attained. The salient points may be summarized as follows.

1) The maximum elastic modulus is obtained in material of highest density, in structures where the solid phase is continuous and the pores closed and spherical. The addition of a second phase of higher modulus causes the resultant modulus of the heterogeneous mixture to be increased.

2) The damping capacity of a ceramic single crystal at a particular temperature depends on the density and mobility of dislocations. The introduction of grain boundaries raises the damping capacity in a certain characteristic temperature range, this range can be broadened and extended to lower temperatures by the addition of impurity.

3) Ceramic materials deform plastically at the stress level and temperature at which dislocations are sufficiently mobile. The mobility of a dislocation can be reduced by impurities in a number of ways, (a) direct elastic interaction with impurity ions to lock the dislocation line, (b) indirect elastic interaction of the moving dislocation line with internal stress fields due to impurity ions in solid solution or precipitate particles, (c) electrostatic interaction of the dislocation line with charged point defects introduced to maintain neutrality. Each of these mechanisms leads to an increase in strength.

4) Plastic deformation of polycrystalline ceramics at low temperatures is prohibited by the lack of sufficient independent slip systems. At high temperatures some ceramic materials (eg. MgO) slip on additional systems and macroscopic polycrystalline ductility then becomes possible.

5) The tensile fracture strength at low temperatures is a maximum in fully dense, flaw free specimens of a ceramic material in which dislocations cannot move (eg. Al_2O_3). In the presence of porosity or surface damage the strength is determined by the critical stress to propagate a preexisting flaw. In the absence of porosity and surface damage brittle fracture occurs in those ceramics in which dislocations can move (eg. MgO) by the interaction of slip with grain boundaries, and in those ceramics in which dislocations cannot move the strength is limited by internal stresses developed in fabrication.

6) High temperature creep of ceramic single crystals occurs by dislocation motion and climb. Impurities hinder dislocation motion and thereby lower the creep rate of single crystals.

7) High temperature creep of polycrystalline ceramics generally occurs by vacancy migration under stress and grain boundary sliding. Impurities lower grain boundary viscosity and thereby increase the creep rate of polycrystals. Plastic deformation by dislocation motion and climb is generally restricted by lack of sufficient independent slip systems even at high temperatures.

Even with simple ceramic materials the above interpretations of mechanical behavior are still quite flexible and there remains a great need for critical theoretical and experimental work. Current developments of fully dense polycrystalline ceramics by novel fabrication techniques are providing the experimentalist with a good opportunity to perform quantitative experiments on well defined systems. The next few years should be particularly productive with respect to understanding the mechanical properties of polycrystalline material.

Acknowledgments

It is a pleasure to acknowledge the Office of Naval Research and Aeronautical Systems Division, U. S. Air Force for their sustained support of this work. The author has benefited from discussions with colleagues at Honeywell Research Center, in particular the criticism of Dr. C. H. Li has been very helpful in arranging the material for presentation. I am grateful to Drs. G. W. Groves and A. Kelly and Professor R. L. Coble for making their manuscripts available before publication.

References

[1] R. L. Coble, Ceramic Fabrication Processes, p. 213, M.I.T. and J. Wiley and Sons, Inc., New York (1958).

[2] J. J. Gilman and W. G. Johnston, Dislocations and Mechanical Properties of Crystals, p. 116, J. Wiley and Sons, Inc., New York (1957).

[3] A. E. Gorum, E. R. Parker, and J. A. Pask, J. Am. Ceram. Soc. 41, 161 (1958).

[4] W. D. Kingery, Introduction to Ceramics, p. 597, J. Wiley and Sons, Inc., New York (1960).

[5] B. Paul, Trans. A.I.M.E. 218, 37, (1960).

[6] Z. Hashin, J. Appl. Mechanics 29, 143 (1962).

[7] D. P. H. Hasselman and P. T. B. Shaffer, Factors Affecting Thermal Shock Resistance of Polyphase Ceramic Bodies, WADC Technical Report 60-749, Part II, April (1962).

[8] C. Nishimatsui and J. Gurland, Trans. Am. Soc. Metals 52, 469, (1960).

[9] D. P. H. Hasselman, J. Am. Ceram. Soc. 46, 103 (1963).

[10] J. K. Mackenzie, Proc. Phys. Soc. (London) (B), 63, 2 (1950).

[11] R. L. Coble and W. D. Kingery, J. Am. Ceram. Soc. 39, 377 (1956).

[12] P. Murray, D. T.Livey, and J. Williams, Ceramic Fabrication Processes, p. 147, M.I.T. and J. Wiley and Sons, Inc., New York (1958).

[13] R. M. Spriggs, J. Am. Ceram. Soc. 44, 628 (1961).

[14] F. P. Knudsen, J. Am. Ceram. Soc. 45, 94 (1962).

[15] R. M. Spriggs, L. A. Brisette, and T. Vasilos, J. Am. Ceram. Soc. 45, 400 (1962).

[16] D. P. H. Hasselman, J. Am. Ceram. Soc. 45, 452 (1962).

[17] R. M. Spriggs and T. Vasilos, Paper presented at 63rd Annual Meeting, Am. Ceram. Soc., Abstract in Am. Ceram. Soc. Bull. 40, 187 (1961).

[18] C. Zener, Elasticity and Anelasticity of Metals, University of Chicago Press, Chicago (1942).

[19] R. Chang, J. Nuclear Materials 1, 174 (1959).

[20] J. B. Wachtman and L. H. Maxwell, WADC Technical Report 57-526 (1957).

[21] J. E. Turnbaugh, Sc. D. Thesis, M.I.T. (1962).

[22] W. B. Crandall, D. H. Chung, and T. J. Gray, Mechanical Properties of Engineering Ceramics, p. 349, Interscience, New York (1961).

[23] R. Chang, Mechanical Properties of Engineering Ceramics, p. 209, Interscience, New York (1961).

[24] A. S. Nowick, Progress in Metal Physics 4, 1 (1956). See also Acta Metallurgica 10, 337 (1962).

[25] R. B. Gordon and A. S. Nowick, Acta Metallurgica 4, 514 (1956).

[26] R. W. Whitworth, Phil. Mag. 5, 425 (1960).

[27] A. Taylor, Acta Metallurgica 10, 489 (1962).

[28] P. Dahlberg, R. D. Carnahan, and J. D. Brittain, J. Appl. Phys. 33, 3493 (1962).

[29] R. Chang, J. Appl. Phys. 32, 1127 (1961).

[30] Mechanical Behavior of Crystalline Solids, Ceramic Educational Council Seminar, (1962), National Bureau of Standards Monograph 59 (1963).

[31] J. J. Gilman, Acta Metallurgica 7, 608 (1959).

[32] W. A. Rachinger and A. H. Cottrell, Acta Metallurgica 4, 109 (1956).

[33] M. L. Kronberg, Acta Metallurgica 5, 507 (1957).

[34] S. Amelinckx and P. Delavignette, Mechanical Properties of Engineering Ceramics, p. 105, Interscience, New York (1961).

[35] S. Amelinckx and P. Delavignette, Direct Observations of Imperfections in Crystals, p. 295, Interscience, New York (1962).

[36] K. H. G. Ashbee and R. E. Smallman, J. Am. Ceram. Soc. 46, 211 (1963).

[37] J. B. Wachtman and L. H. Maxwell, J. Am. Ceram. Soc. 37, 291 (1954).

[38] R. Scheuplein and P. Gibbs, J. Am. Ceram. Soc. 43, 458 (1960).

[39] M. L. Kronberg, J. Am. Ceram. Soc. 45, 274 (1962).

[40] W. G. Johnston and J. J. Gilman, J. Appl. Phys. 31, 632 (1960).

[41] W. G. Johnston and J. J. Gilman, J. Appl. Phys. 30, 129 (1959).

[42] R. J. Stokes, T. L. Johnston, and C. H. Li, Trans. A.I.M.E. 215, 437 (1959).

[43] R. J. Stokes, Trans. A.I.M.E. 224, 1227 (1962).

[44] J. D. Venables, Phys. Rev. 122, 1388 (1961).

[45] J. D. Venables, J. Appl. Phys. 34, 293 (1963).

[46] W. G. Johnston, J. Appl. Phys. 33, 2050 (1962).

[47] W. J. Luhman and A. E. Gorum, Acta Metallurgica 7, 685 (1959).

[48] N. S. Stoloff, D. K. Lezius, and T. L. Johnston, J. Metals 15, 84 (1963). J. Appl. Phys., to be published.

[49] R. J. Stokes and C. H. Li, Acta Metallurgica 10, 535 (1962).

[50] E. Schmid and W. Boas, Plasticity of Crystals, p. 236, Hughes and Co., Ltd., London (1950).

[51] E. R. Parker, Mechanical Properties of Engineering Ceramics, p. 65, Interscience, New York (1961).

[52] J. D. Eshelby, C. A. Newey, P. L. Pratt, and A. B. Lidiard, Phil. Mag. 3, 75 (1958).

[53] P. L. Pratt, Symposium on Vacancies and Other Point Defects in Metals and Alloys, p. 99, Institute of Metals, London (1957).

[54] A. E. Gorum, W. J. Luhman, and J. A. Pask, J. Am. Ceram. Soc. 43, 241 (1960).

[55] J. E. May and M. L. Kronberg, J. Am. Ceram. Soc. 43, 525 (1960).

[56] R. J. Stokes, Final Report on ASD Contract AF33(616)-7465, Nov. 1962.

[57] F. G. Satkiewicz, Mechanical Properties of Engineering Ceramics, p. 49, Interscience, New York (1961).

[58] T. S. Liu, R. J. Stokes, and C. H. Li, to be published.

[59] R. von Mises, Zeit. Angew. Math. und Mech. 8, 161 (1928).

[60] G. I. Taylor, J. Inst. Metals 62, 307 (1938).

[61] G. W. Groves and A. Kelly, Phil. Mag., to be published (1963).

[62] R. J. Stokes and C. H. Li, Paper presented at Conference on Structure and Properties of Engineering Materials, Raleigh (1962), to be published.

[63] R. D. Carnahan, T. L. Johnston, R. J. Stokes, and C. H. Li, Trans. A.I.M.E. 221, 45 (1961).

[64] W. D. Scott and J. A. Pask, Paper presented at 64th Annual Meeting, Am. Ceram. Soc., Abstract in Am. Ceram. Soc. Bull. 41, 309 (1962).

[65] S. Dommerich, Zeit. fur Physik 90, 189 (1934).

[66] J. J. Gilman, Acta Metallurgica 7, 608 (1959).

[67] C. O. Hulse, S. M. Copley, and J. A. Pask, Paper presented at 65th Annual Meeting, Am. Ceram. Soc., Abstract in Am. Ceram. Soc. Bull. 42, 187 (1963).

[68] A. A. Griffith, Phil. Trans. Roy. Soc. (London) (A), 221, 163 (1921).

[69] T. L. Johnston, C. H. Li, and R. J. Stokes, Strengthening Mechanisms in Solids, p. 341, American Society for Metals, Cleveland, Ohio (1962).

[70] F. J. P. Clarke, R. A. J. Sambell, and H. G. Tattersall, Phil. Mag. 7, 393 (1962).

[71] R. J. Stokes and C. H. Li, Fracture of Solids, Interscience, New York (1963).

[72] E. Orowan, Fatigue and Fracture of Metals, p. 135, J. Wiley and Sons, Inc., New York (1952).

[73] R. J. Stokes, T. L. Johnston, and C. H. Li, Phil. Mag. 4, 920 (1959).

[74] R. J. Stokes, T. L. Johnston, and C. H. Li, Phil. Mag. 6, 9 (1961).

[75] A. R. C. Westwood, Phil. Mag. 6, 195 (1961).

[76] T. L. Johnston, R. J. Stokes, and C. H. Li, Phil. Mag. 7, 23 (1962).

[77] F. J. P. Clarke, R. A. J. Sambell, and H. G. Tattersall, Trans. Brit. Ceram. Soc. 61, 61 (1962).

[78] R. J. Stokes and C. H. Li, J. Am. Ceram. Soc., to be published.

[79] C. Zener, Fracturing of Metals, p. 3, American Society for Metals, Cleveland, Ohio (1948).

[80] A. N. Stroh, Advances in Physics 6, 418 (1957).

[81] E. Ryshkewitch, J. Am. Ceram. Soc. 36, 65 (1953).

[82] W. Duckworth, J. Am. Ceram. Soc. 36, 68 (1953).

[83] F. P. Knudsen, J. Am. Ceram. Soc. 42, 376 (1959).

[84] F. P. Knudsen, H. S. Parker, and M. D. Burdick, J. Am. Ceram. Soc. 43, 641 (1960).

[85] R. M. Spriggs and T. Vasilos, J. Am. Ceram. Soc. 46, 224 (1963).

[86] I. B. Culter, J. Am. Ceram. Soc. 40, 20 (1957).

[87] C. Hyde, J. F. Quirk, and W. H. Duckworth, quoted in reference [22].

[88] W. Weibull, Proc. Ingen. Vetenskaps. Acad. 151, 1 (1939).

[89] W. B. Harrison, Paper presented at 64th Annual Meeting, Am. Ceram. Soc., see Am. Ceram. Soc. Bull. 41, 311 (1962), to be published.

[90] Fracture, John Wiley and Sons, Inc., New York (1959).

[91] W. M. Hirthe, N. R. Adsitt, and J. O. Brittain, Direct Observations of Imperfections in Crystals, p. 135, Interscience, New York (1962).

92 W. S. Williams and R. D. Schaal, J. Appl. Phys. 33, 955 (1962).

93 J. E. Dorn, Creep and Recovery, p. 255, American Society for Metals, Cleveland, Ohio (1957).

94 J. Weertman, J. Appl. Phys. 26, 1213 (1955): 28, 362 (1957).

95 F. R. N. Nabarro, Conference on Strength of Solids, p. 75, The Physical Society, London (1948).

96 C. Herring, J. Appl. Phys. 21, 437 (1950).

97 M. A. Adams and G. T. Murray, J. Appl. Phys. 33, 2126 (1962).

98 G. T. Murray, J. Silgailis, A. J. Mountvala, Report on Air Force Contract AF33(616)-7961. Report No. ASD-TDR-62-225.

99 J. F. Wygant, J. Am. Ceram. Soc. 34, 374 (1951).

100 W. A. Rogers, G. S. Baker, and P. Gibbs, Mechanical Properties of Engineering Ceramics, p. 303, Interscience, New York (1962).

101 R. Chang, J. Appl. Phys. 31, 484 (1960).

102 S. I. Warshaw and F. H. Norton, J. Am. Ceram. Soc. 45, 479 (1962).

103 R. C. Folweiler, J. Appl. Phys. 32, 773 (1961).

104 R. L. Coble and Y. H. Guerard, J. Am. Ceram. Soc., to be published.

105 A. E. Paladino and R. L. Coble, J. Am. Ceram. Soc. 46, 133 (1963).

106 R. R. Vandervoort and W. L. Barmore, J. Am. Ceram. Soc. 46, 180 (1963).

107 R. L. Coble, private communication.

108 R. B. Day and R. J. Stokes, to be published.

109 R. L. Coble and W. D. Kingery, J. Am. Ceram. Soc. 39, 377 (1956).

110 R. Scott, A. R. Hall, and J. Williams, J. Nuclear Materials 1, 39 (1959).

111 W. M. Hirthe and J. O. Brittain, paper presented at 64th Annual Meeting, Am. Ceram. Soc., see Am. Ceram. Soc. Bulletin 41, 311 (1962).

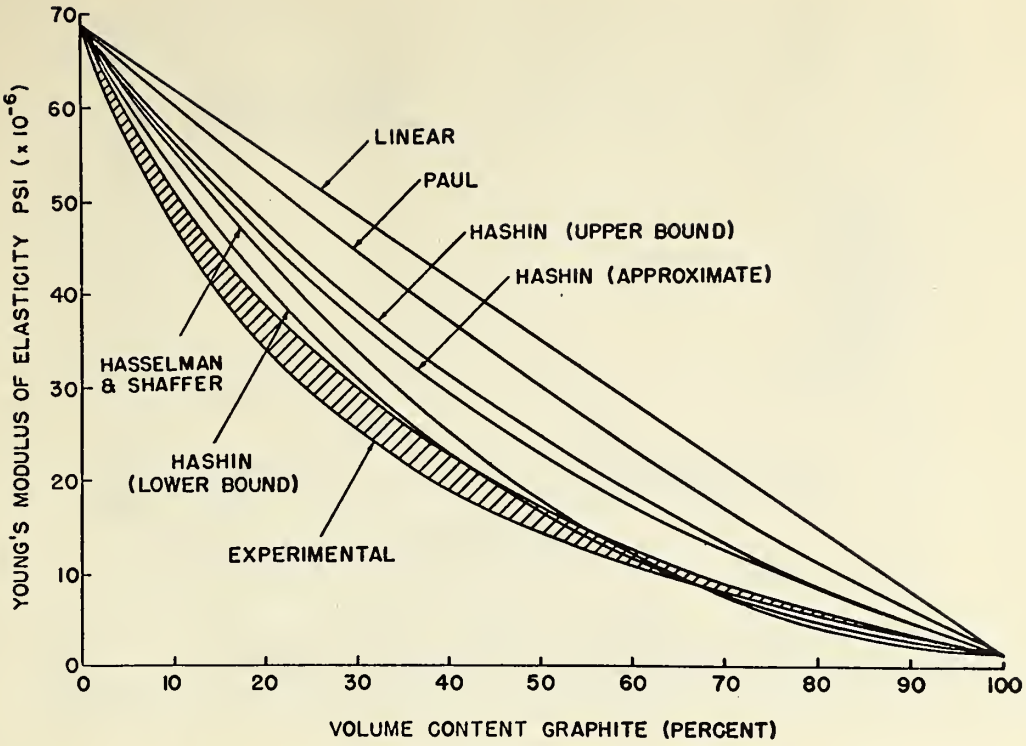

Figure 1. The variation in elastic modulus of a two phase solid. Comparison of theoretical and experimental relationships for the system zirconium carbide plus carbon. (After Hasselman and Shaffer [7]).

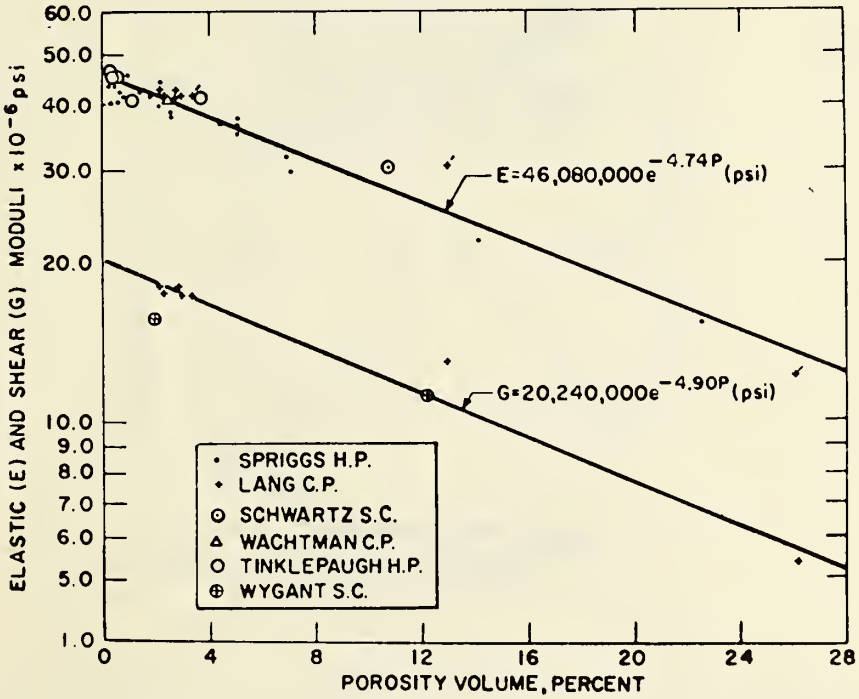

Figure 2. Effect of porosity on elastic (E) and shear (S) moduli of polycrystalline magnesia at room temperature. Letters after author names are fabrication codes, H.P. - hot pressed, C.P. - cold pressed and sintered, and S. C. - slip cast and sintered. (After Spriggs et al. [15]).

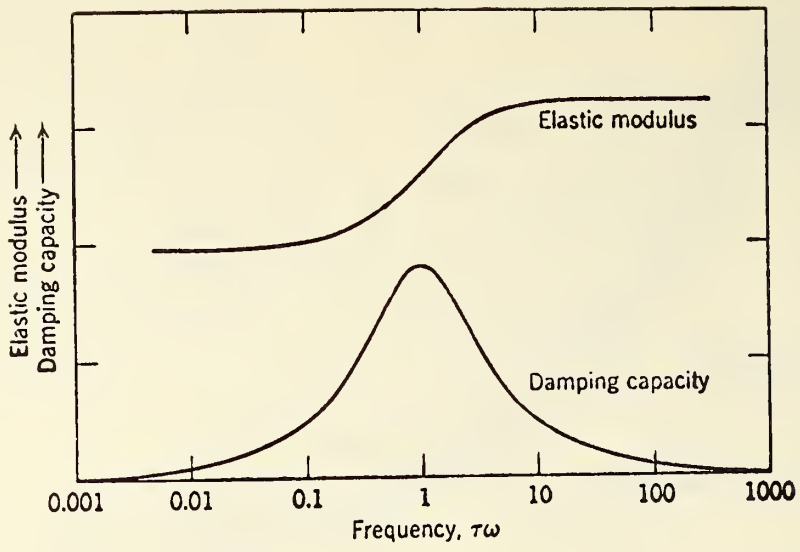

Figure 3. Change in damping capacity (internal friction) and dynamic elastic modulus with frequency. Amplitude and temperature constant.

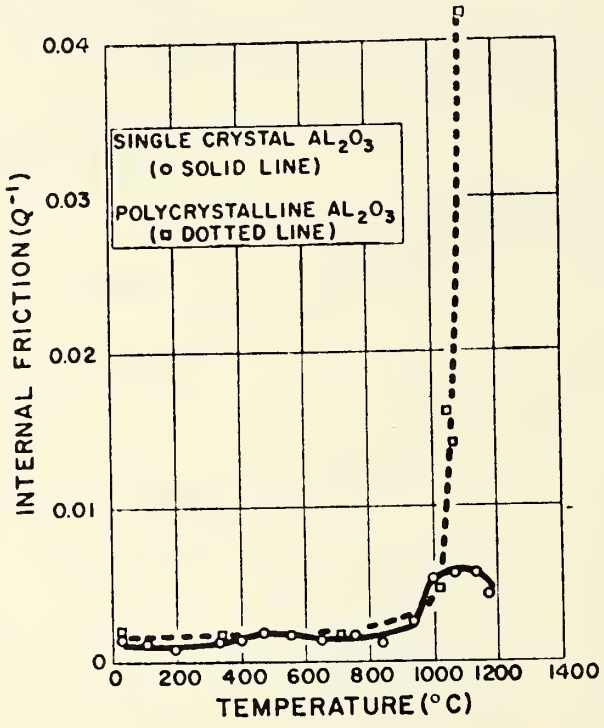

Figure 4. The internal friction spectrum for single crystal and polycrystalline alumina. (After Chang [19]).

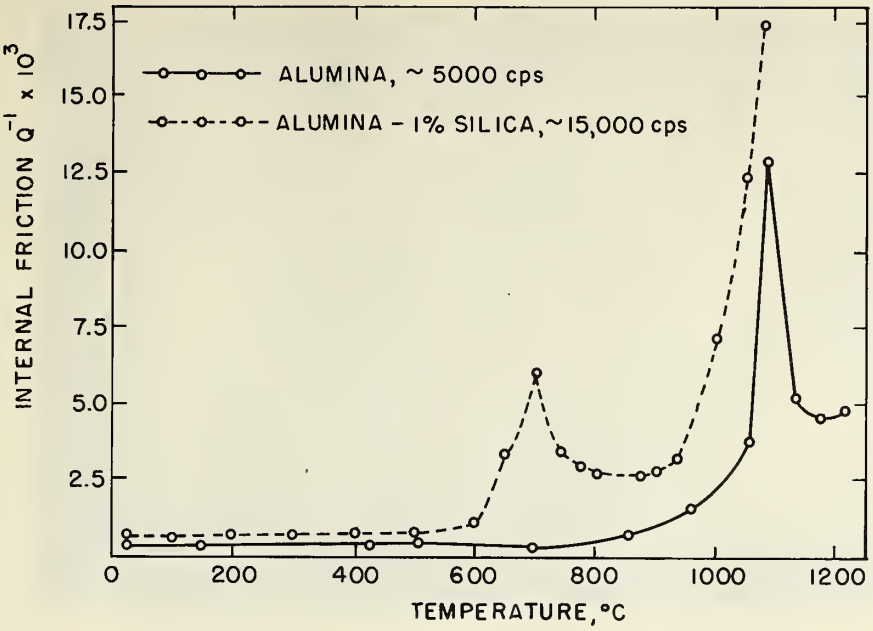

Figure 5. Effect of impurity on the internal friction spectrum of polycrystalline alumina. The addition of 1% SiO_2 introduces a new low temperature internal friction peak. (After Crandall et al. [22]).

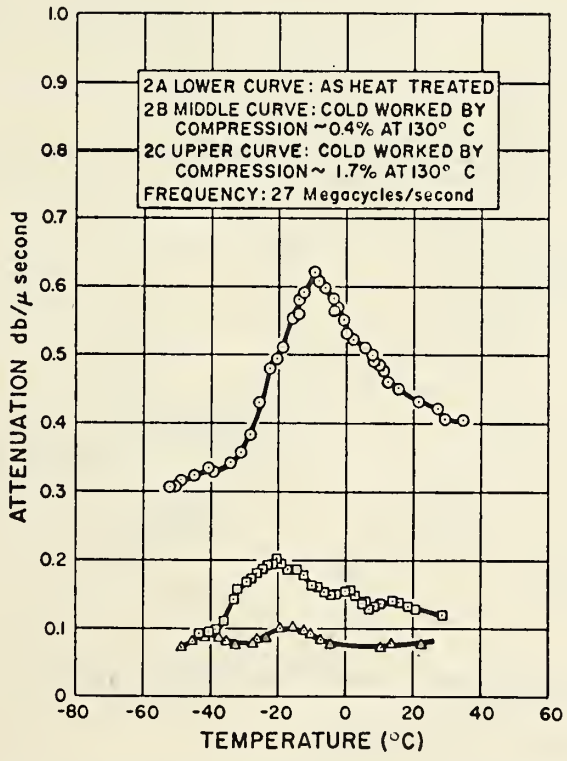

Figure 6. Effect of plastic deformation on the internal friction spectrum of magnesium oxide single crystals. (After Chang [29]).

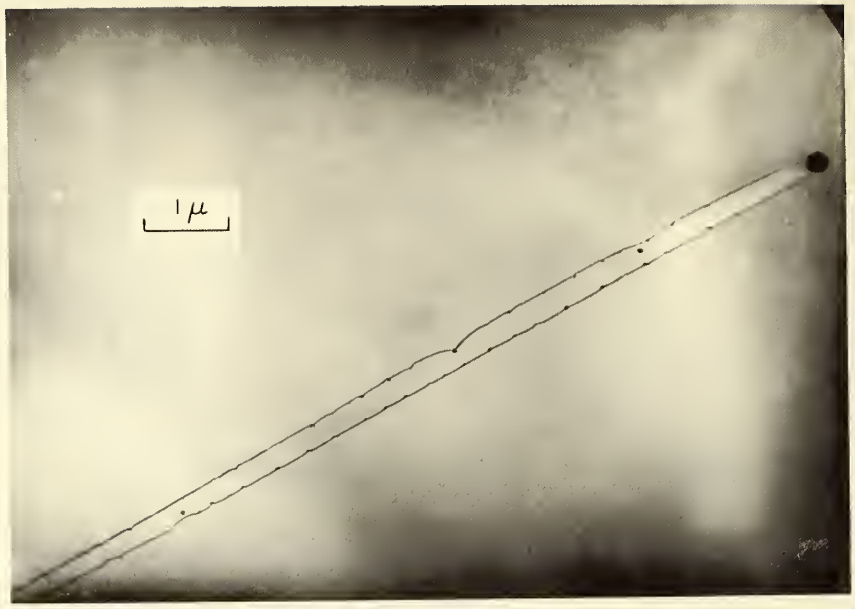

Figure 7. "Grown in" dislocations in magnesium oxide. Note the impurity precipitate particles spaced at fairly regular intervals. (Electron transmission micrograph courtesy G. W. Groves).

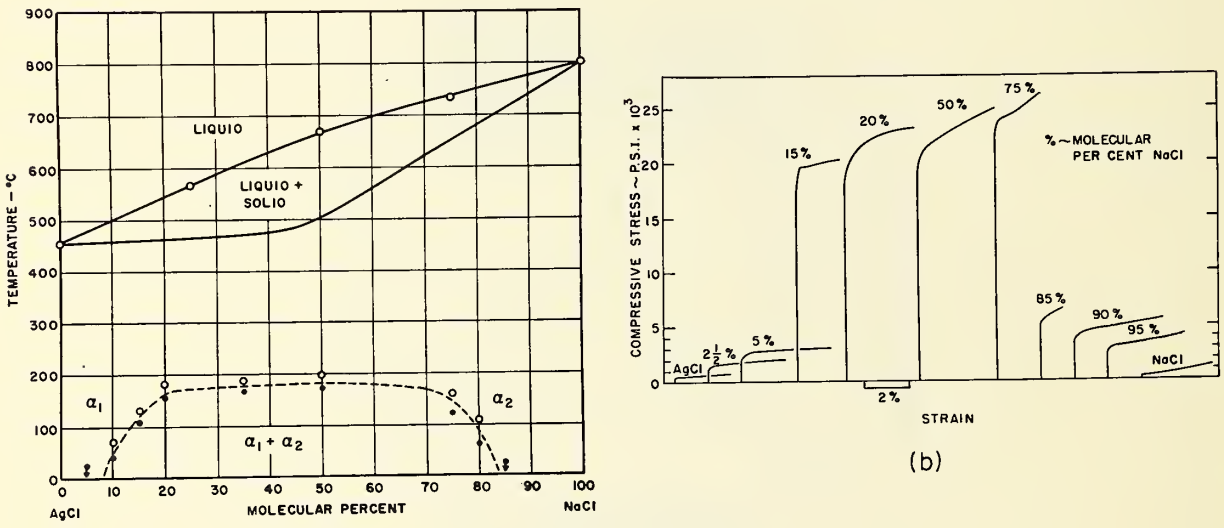

Figure 8 Solid solution and precipitation hardening in the silver chloride-sodium chloride alloy system.

(a) The AgCl-NaCl phase diagram

(b) Compression stress strain curves for AgCl-NaCl alloy single crystals.

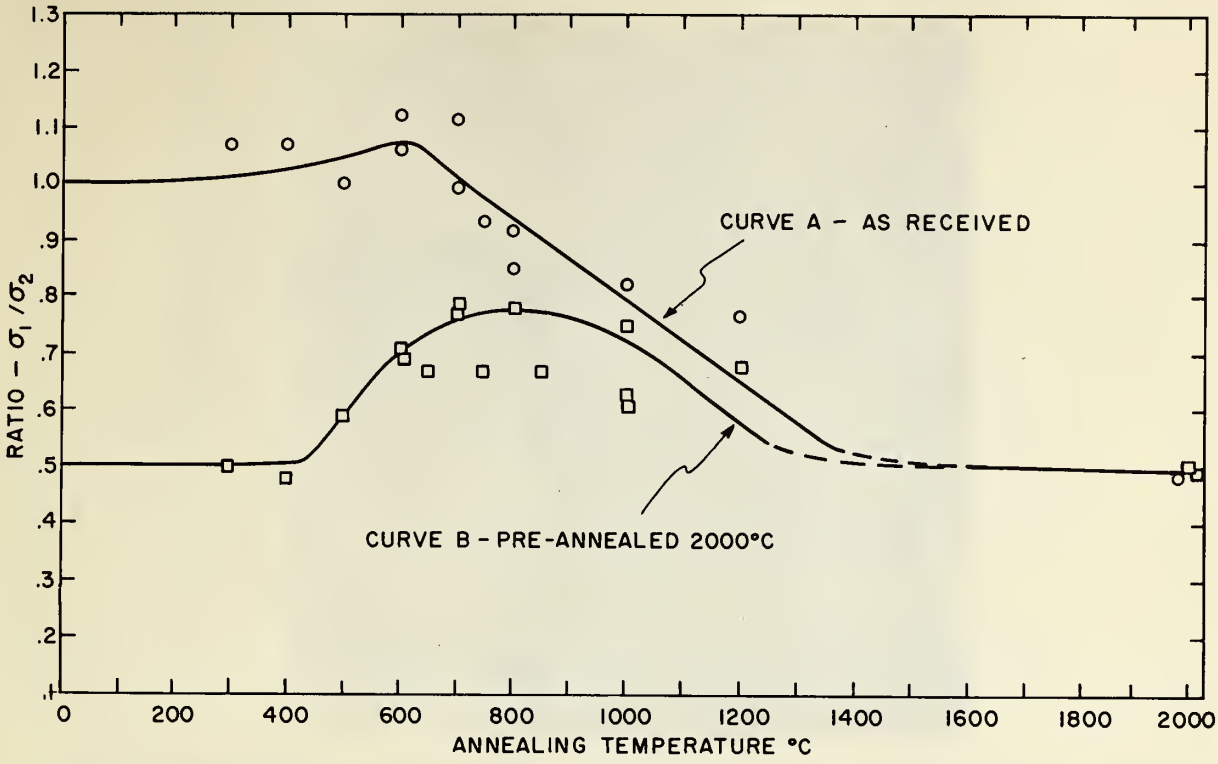

Figure 9. Effect of heat treatment on the room temperature yield strength of commercial purity magnesium oxide single crystals.

σ_1 - room temperature yield strength in as-received (fully precipitated) condition.

σ_2 - room temperature yield strength after annealing.

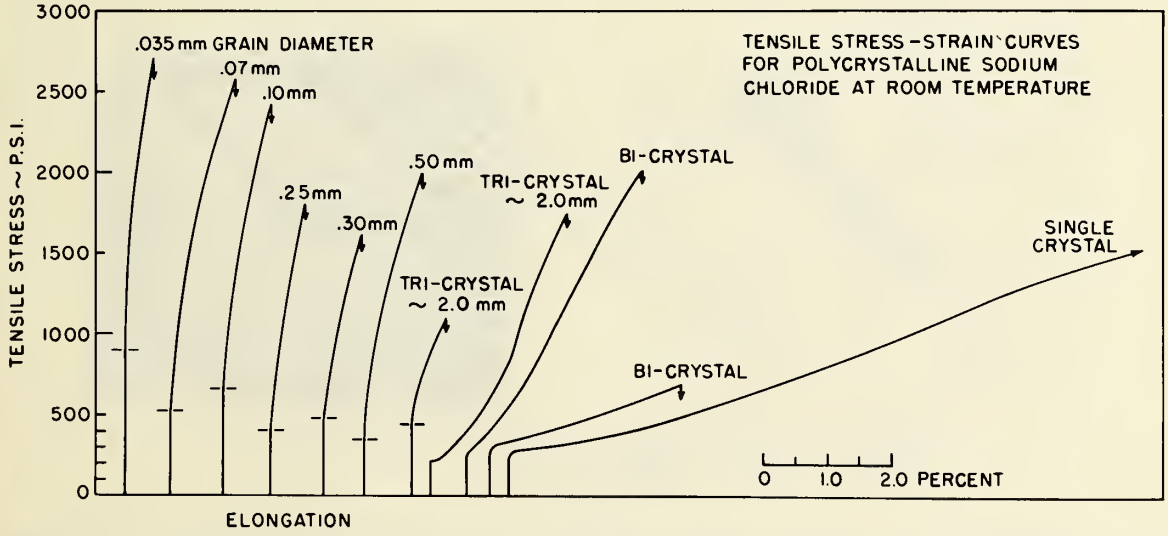

Figure 10. Tensile stress strain curves for polycrystalline sodium chloride at room temperature illustrating the effect of decreasing the grain size on the proportional limit and rate of work hardening.

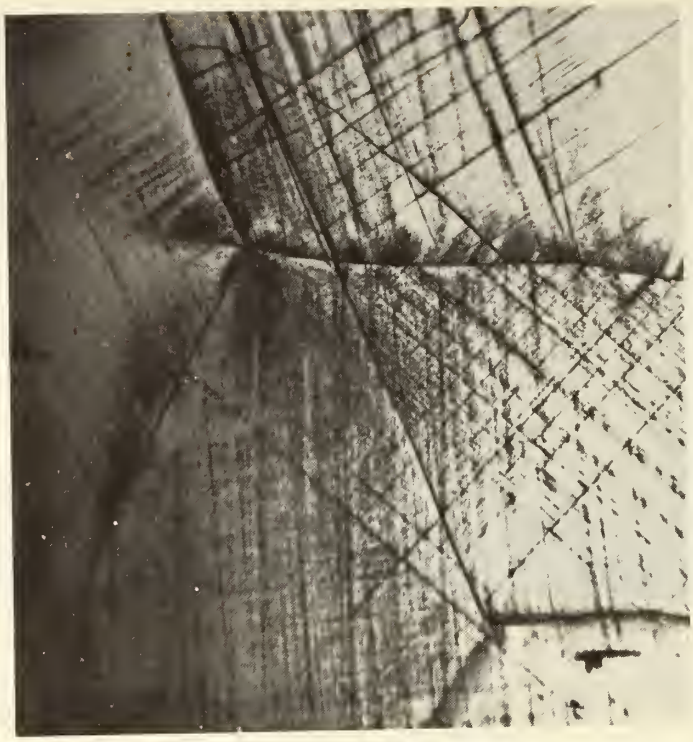

Figure 11. Slip distribution in the vicinity of grain boundaries in lithium fluoride deformed at room temperature. Note very local slip on {001} planes near triple point. Slip revealed by etch pit technique. (courtesy W. D. Scott and J. A. Pask).

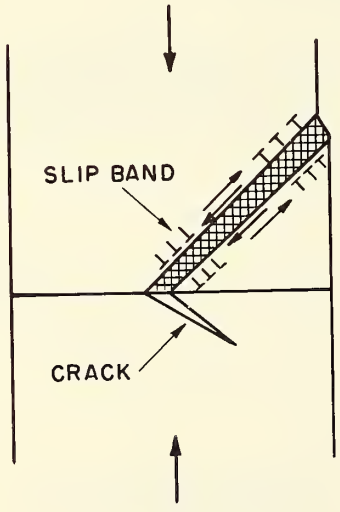

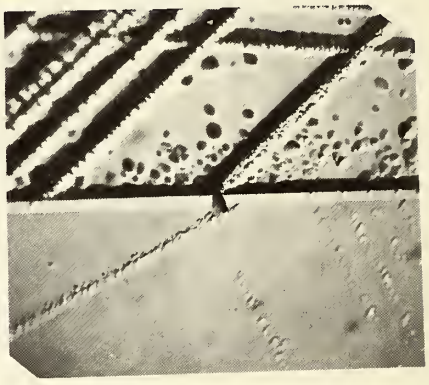

Figure 12. Nucleation of a cleavage crack due to dislocation pile up at a grain boundary. Magnesium oxide bi-crystal deformed in compression. Slip revealed by etch pit technique.

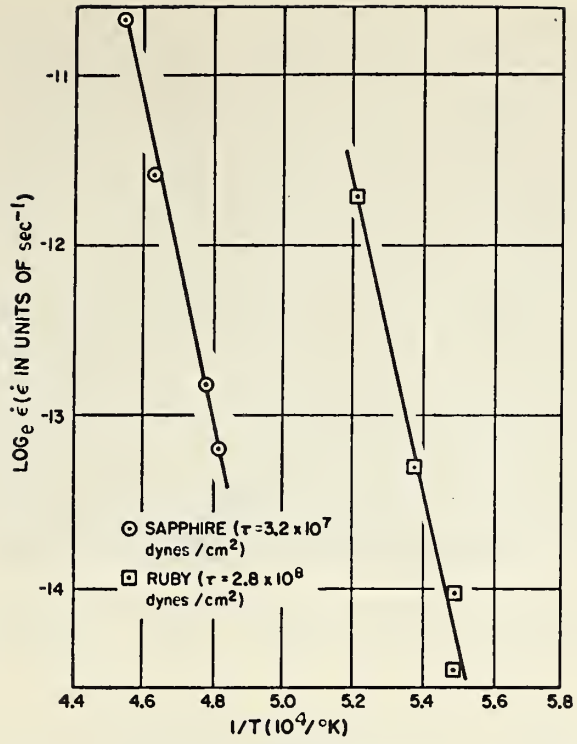

Figure 13. Effect of purity on the steady state creep rate of alumina. The addition of 2% Cr_2O_3 lowers the creep rate by 10^4. (After Chang [101]).

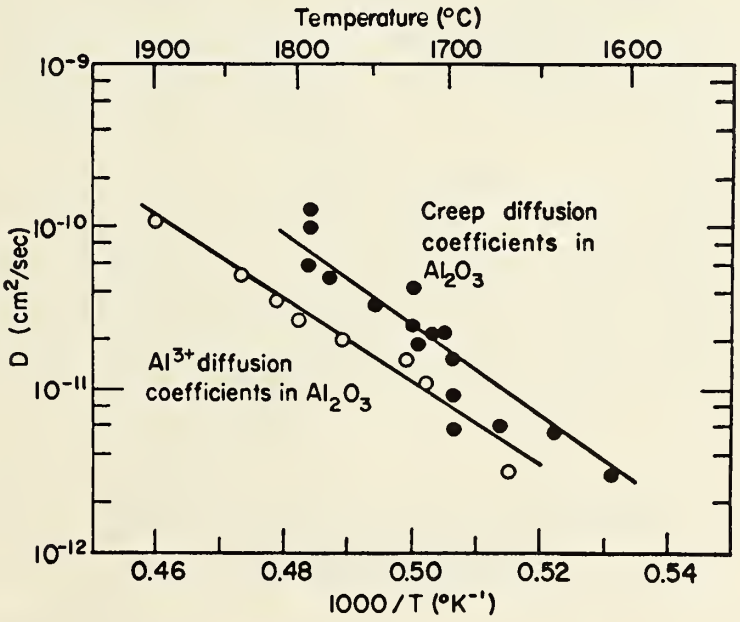

Figure 14. Comparison of the diffusion coefficient measured for self diffusion of the aluminum ion with the diffusion coefficient calculated from creep data of alumina using the Nabarro-Herring equation. (After Paladino and Coble [105]).

Figure 15. Generation of intergranular voids during torsional creep of high density alumina. (courtesy R. L. Coble).

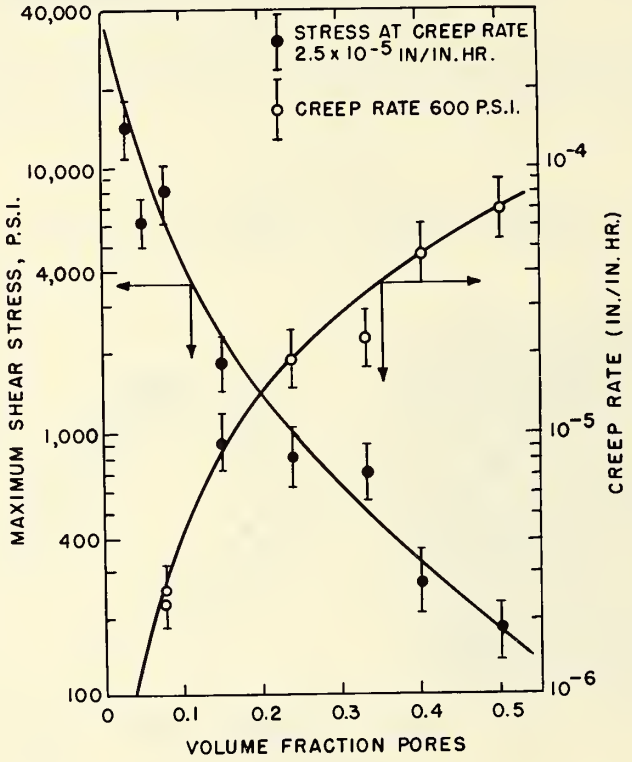

Figure 16. Effect of porosity on the torsional creep of sintered alumina at 1275°C.

The stress to promote a constant creep rate and the creep rate at a constant stress are both plotted as a function of the porosity. (After Coble and Kingery [109]).

Microstructure of Magnetic Ceramics

A.L. Stuijts

1. Introduction

Electrical engineering has made enormous strides since the beginning of this century. Advances in the field of telecommunication and high-frequency techniques have stimulated the development of the required high-frequency insulating, dielectric and magnetic materials.

Important developments in the field of magnetic oxides were started in our laboratories in the late thirties by J.L. Snoek [1] [1]. Although other investigators had realized the potential importance of ferrites for high-frequency applications, it was Snoek and his collaborators who took the fundamental step to obtain control of these materials so as to make their properties useful to the electrical engineer. They were also able to explain a number of fundamental aspects of the high-frequency behaviour of ferrites.

Simultaneously pioneering work was done to gain further knowledge of the ionic structure of these ferrites [2]. These studies made it possible to explain the semiconducting properties, and the basis was laid for a further interpretation of the magnetic behaviour.

The French scientist L. Néel succeeded in predicting the magnitude of the magnetic moment as well as its curious temperature dependence [3]. He introduced the name "uncompensated anti-ferromagnetism" or "ferrimagnetism", since, as opposed to the case in ordinary ferromagnetic alloys, the exchange forces orient the magnetization vectors of neighbouring spins antiparallel. The predictions of Néel have been confirmed by the experimental work of Guillaud and Gorter [4].

After 1950 a new period in the development of magnetic oxides set in. New systems of magnetic oxides were discovered and developed, such as the hexagonal permanent-magnet material $BaFe_{12}O_{19}$, the ferroxplana materials and the garnets. On the other hand new developments in electronics occurred, thanks to the application of such specific properties of magnetic oxides as their gyromagnetic effects and their ability to store information.

An essential feature of the magnetic ceramics is the combination of moderate magnetic permeability with high volume resistivity (from 10 up to 10^{10} ohm.cm). Thus eddy-current losses in an alternating field of high frequency can be very low.

The development of magnetic oxidic materials has many different aspects involving physicists, chemists and engineers. Most of the properties are very sensitive to variations in chemical composition, ionic distribution over different lattice sites, ionic ordering phenomena, etc. Furthermore the shape of the product is of importance for the application. Although magnetic oxides can be formed in any shape by ceramic techniques, there are considerable problems in combining an exact control of the chemistry with control of the microstructure of the shaped ceramic product. It is with these problems that the present paper is concerned.

Although considerable progress has been made in the last decade with respect to fundamental aspects of chemical reactions and sintering, we are still far from being able to control the microstructure even in simple oxides. There is, however, an overwhelming amount of information on the importance of such control. The main part of this paper will deal with a number of obvious examples of the importance of microstructure in the development of "tailor-made" magnetic ceramics.

[1] Figures in brackets indicate the literature references at the end of this paper

2. Crystal Structure and Intrinsic Magnetic Properties

The mineral magnetite, $Fe^{2+}Fe_2^{3+}O_4$, was already used in antiquity for its magnetic properties. The magnetic ceramic materials now used in electronics are found in a limited range of crystal structures. The cubic ferrites have the spinel structure with the general formula $MeFe_2O_4$, in which Me is Mn, Ni, Co, Fe^{2+}, Mg, Zn, or a combination as for instance $Li^{1+}+Fe^{3+}$. Moreover Fe^{3+} can be substituted by e.g. Al- or Cr-ions. Thus a great variety is possible in the chemical composition of ferrites with spinel structure [5] . The large oxygen ions form a close-packed structure, in which two kinds of interstitial sites are occupied, viz. tetragonal sites and twice as many octahedral sites. Some metal ions, like Zn and Cd, have a strong preference for the tetrahedrally-surrounded sites; others, like Fe^{2+} and Ni, for the octahedrally-surrounded ones. The spins of neighbouring ions in these oxides are oriented anti-parallel by the exchange forces. These forces, however, are strongest for the interaction between the magnetic ions in tetrahedral and octahedral sites mutually. When the sum of the magnetic moments at tetrahedral sites differs from that at octahedral sites, a net magnetic moment can result. In the case of ferrous ferrite, for example, in which Fe^{2+} contributes four Bohr magnetons and Fe^{3+} five:

$$\underset{5}{Fe^{3+}} \quad \underset{4}{Fe^{2+}} \quad \underset{5}{Fe^{3+}} \quad O_4$$

there is a net magnetic moment of four Bohr magnetons per formula unit.

The study of the distribution of the constituent metal ions over the different types of lattice sites is very important. The intrinsic magnetic properties, and to a large extent also the technologically important properties, are intimately related to detailed aspects of the crystal chemistry of these compounds.

The same holds for the ferrites based on the structure of the mineral garnet, for which the prototype is $Y_3Fe_5O_{12}$. In this case the ionic distribution over the tetrahedral and octahedral lattice sites has also been studied, but garnets are very often used unsubstituted.

Next there is a group of ferrites with closely related hexagonal crystal structures. These compounds are found in the diagram of figure 1, the corners of which represent the oxides BaO, MeO and Fe_2O_3. In the same way as in the spinel structure, a great number of ions can be introduced. One of the compounds, $BaFe_{12}O_{19}$ or barium hexaferrite, has become a technically important permanent-magnetic material. Some of the other hexagonal compounds, e.g. $Ba_3Co_2Fe_{24}O_{41}(Co_2Z)$ or $Ba_2Zn_2Fe_{12}O_{22}$ (Zn_2Y), have interesting high-frequency magnetic properties.

As for the chemistry of magnetic oxides, we will limit the description of the intrinsic magnetic properties to the most essential points. For further study reference may be made to the original literature in this field, which is readily accessible (see e.g. [6]).

A ferromagnetic material is characterized by its spontaneous magnetization, originating from the magnetic moments of the magnetic ions. The exchange interaction which aligns the magnetic moments of the electron spins parallel or antiparallel is opposed by thermal agitation. Thus the spontaneous magnetization has a characteristic temperature dependence, which disappears at the Curie point.

There are several factors binding the magnetization vectors to certain directions :

1. The crystalline anisotropy. The spin of the electron which causes the magnetic moment is coupled with the orbit of that electron; the electron orbit is in its turn fixed by the symmetry of the crystal lattice. As a result of this spin-orbit and orbit-lattice coupling, the magnetic moment has a preference to be directed along certain crystallographic directions. These directions are called directions of easy magnetization and are related to the symmetry of the crystal lattice. Work has to be supplied to rotate the magnetization into a difficult or hard direction, the energy being the crystalline anisotropy energy E_c.

In most spinels the easy direction is the cube diagonal. By the substitution of a sufficient amount of Co-ions it changes into a cube edge. Most of the hexagonal compounds have large crystalline anisotropy energies, with the preferential direction of magnetization either parallel to the c-direction, within the basal plane perpendicular to the c-axis, or on a cone lying in between the c-axis and the basal plane.

2. When a body of a ferromagnetic material is magnetized its length changes. The origin of this linear magnetostriction $\lambda = \frac{dl}{l}$ is closely related to that of the crystalline anisotropy. Conversely, external stresses act on the direction of magnetization by virtue of the presence of magnetostriction, and this strain anisotropy energy is proportional to the linear magnetostriction λ_s, and the external stress σ :

$$E_s \propto \lambda_s \sigma .$$

For the further considerations in our paper we shall assume the crystalline anisotropy to be predominant, since a similar treatment applies for both anisotropies. In many cases it is convenient to express the binding force to a certain direction as an anisotropy field H^A, proportional to K/M_s, where K is the absolute value of the anisotropy constant.

3. Permeability and Hysteresis Loop

An externally applied magnetic field will cause the magnetization to turn toward the field direction (see figure 2). The change in magnetic induction, ΔB, for an applied field, ΔH, is the permeability of the material:

$$\mu = \frac{\Delta B}{\Delta H}$$

The magnetic induction B is simply the sum of the magnetization $4\pi M$ and the external magnetizing field H:

$$B = 4\pi M + H$$

If there were no opposing forces, the permeability would be infinite. The forces which bind the magnetization vector to certain directions (the anisotropy field H^A) cause the external field necessary to obtain a given value of ΔB to have a definite value and thus the permeability to be finite.

The initial permeability, for a small value of ΔB, is proportional to the saturation magnetization M_s and inversely proportional to the anisotropy field H^A:

$$\mu \propto \frac{M_s}{H^A} \quad \text{or} \quad \mu_i \propto \frac{M_s^2}{K}$$

The presence of anisotropy, and thus a finite permeability gives rise to a hysteresis loop when the magnetic induction B is measured as a function of a magnetic field H, the field being varied from a large negative to a large positive value and back. The value of B for H = 0 is the remanence or retentivity B_r. A magnetic material has thus two equally large, but oppositely directed remanence values (see figure 3).

When a specimen is cycled around the hysteresis loop, energy is expended which is liberated as heat - the hysteresis losses. Ferromagnetic materials generally are divided into "hard" and "soft" magnetic materials. The basis of this division is the magnitude of the coercivity or coercive force H_c. This is the field necessary to bring the induction, in the direction of the field, to zero. One would expect the value of the coercive force to be closely related to the anisotropy field H^A. This is indeed the case in permanent or "hard" magnetic materials, where high coercivities are an essential property. For "soft" magnetic materials, with low coercive forces and narrow hysteresis loops, the magnetization changes direction in an external field which is generally much smaller than the anisotropy field H^A. Also the permeabilities found are several orders of magnitude higher than calculated with the formula given above. This has to be explained by a different magnetization process.

4. Domain Theory

Pierre Weiss introduced his domain theory at the beginning of this century [7] to explain e.g. the non-magnetic state of a ferromagnetic material. He postulated the existence of local regions in which the magnetization vectors are parallel. The different regions are magnetized in different directions, as shown in an oversimplified way in figure 4. The uniformly magnetized regions are called Weiss domains.

The basic reason for the formation of domains is the reduction of the magnetostatic energy which arises from the external surface of the specimen. See Figure 5a. Such a uniformly magnetized domain possesses induced magnetic poles at the surface.

The stray fields arising from these poles cause a high value of magnetic energy of this system. By division of this body into two domains, as shown in figure 5b, the magnitude of the magnetostatic energy arising from the poles is reduced to one half. It is even possible to eliminate the magnetostatic energy completely by the formation of closure domains, as shown in figures 5c and 5d. In these cases no magnetic flux leaves the structure.

The geometric configuration of the Weiss domain structure which actually is formed is determined by the requirement that the total energy must be minimum. A number of energies have to be taken into account, the most important of these being the energy of the boundary between the domains, the domain wall energy. Bloch [8] showed that the magnetization does not abruptly shift direction at the boundary, but changes direction gradually from atom to atom, as shown in figure 6. As a result of a competition between exchange energy and crystal anisotropy there is a given minimum thickness of the domain wall, the energy of which is the sum of both energies.

The energy associated with the total domain wall area competes with the gain in demagnetizing energy, thus giving rise to a specific width of the domains. Also the magnetoelastic energy comes into play. Given a finite magnetostriction, strains are set up in a configuration†. Work has to be done to fit the domains together, causing the configuration of figure 5d.with more closure domains to be energetically more favourable.

There are several methods of making the Weiss domain structure visible under the microscope. With a colloidal solution of magnetic Fe_3O_4 the so-called powder pattern or Bitter pattern can be made visible. Figure 7 gives an example of this. Owing to stray fields at the surface of the crystal the powder coagulates at the position of the Bloch walls. For optically transparent crystals the Weiss domains can be seen by making use of the optical Faraday-effect [9]. A third method is based on the magneto-optical Kerr-effect [10].

In an external applied field H, and starting from the unmagnetized state, the energy can be lowered in two ways (see figure 8):

1. Rotation processes, in which the magnetization is turned into the direction of the applied field.

2. Domain wall movement, by which the domain having the magnetization vector nearest to the field H grows at the expense of its neighbour.

In the same way as indicated in a preceding paragraph a permeability caused by wall movement would be infinite, if there were no opposing forces. However, the permeability caused by domain wall movement is limited by the fact that the domain wall configuration gives a minimum value for the magnetic energy of the system which is measured [11]. Further it is at this point that the microstructure comes into discussion. Any imperfections in the material - nonmagnetic inclusions or voids, dislocations, concentration fluctuations, internal stresses - will hinder wall movement. If we limit our discussion to non-magnetic inclusions and holes it can be stated that domain walls prefer to contain the inclusion. In figure 9 such a situation is shown. The effect is a decrease in magnetostatic energy, for the same reason as discussed above in regard to the external surface of the specimen. The wall area too, and thus the total wall energy, is reduced. The microstructural characteristics therefore cause the walls to be bound with a certain stiffness to their positions of equilibrium, limiting the wall mobility.

The magnetization curve can be discussed in terms of these two magnetization processes (see figure 10). The initial slope of the curve, starting from the unmagnetized state, is completely reversible. The domain walls are fixed at the imperfections in the material and reversible wall displacements predominate. At larger field strengths the slope increases, the walls then being pulled loose from the imperfections. The walls can travel relatively large distances, but irreversibly, until all domain walls have disappeared. A further increase in induction occurs by rotation of the magnetization vector into the field direction until complete saturation is reached.

Generally the magnetic field necessary to obtain irreversible wall movements is small compared to the anisotropy field H^A. Consequently the coercive force normally measured in any magnetic material is small.

† as shown in figure 5c. In this configuration

5. Single-domain particles. Permanent magnets.

The most straightforward relation between microstructure and magnetic properties is found in the permanent magnet materials based on single-domain behaviour of their constituent particles.

We have seen that the basic reason for the formation of domains is the reduction in magnetostatic energy. When the diameter of a magnetized particle decreases (see figure 11), the magnetostatic energy drops off as the cube of the diameter D of the particle. The domain wall energy, however, drops off only as the square of the diameter. The effect will be that below some critical diameter, D_{cr}, no magnetic energy is gained by dividing the particle into Weiss domains. Below D_{cr} single domain particles exist in which no stable Bloch walls can be formed.

In the absence of domain walls demagnetization can only occur by rotation of the magnetization vectors of the particles against the anisotropy forces. Thus, for high anisotropy fields high coercive forces can result, with H_c of the same order of magnitude as H^A, a necessary condition for permanent magnetic properties.

The critical size, D_{cr}, can be calculated for simple geometrical configurations, giving approximate values [12]. For soft magnetic materials, with low magnitude of the wall energy and thus a relatively large wall thickness, D_{cr} is small. For nickel ferrite a value of 0.08 μ can be calculated [13]. In hard magnetic materials, with a large anisotropy, the wall energy is high and thus the value of D_{cr} relatively large. For the hexagonal compound $BaFe_{12}O_{19}$ a D_{cr} of about 1 micron is calculated [14].

The origin of the permanent magnetic properties of $BaFe_{12}O_{19}$ (or $BaO.6Fe_2O_3$) is the pronounced uniaxial magnetic anisotropy, with the preferred direction of the magnetization parallel to the c-axis. A large single crystal of this compound has low coercivity, owing to the formation of Bloch walls. For permanent magnetic properties the constituent crystallites must be made smaller than the critical diameter. In figure 12 the coercive force H_c is plotted as a function of grain size for some materials, showing the increase in coercive force when the mean grain size decreases.

For a permanent magnet the demagnetization curve, which is the part of the hysteresis loop where B and H are opposite, is of importance. The quality of a permanent magnet is described by its energy product B·H, which reaches a maximum somewhere on the demagnetization curve. It is clear that a high energy product also calls for a high induction. But the induction is roughly proportional to the apparent density of a material, and thus a sintering process is applied in order to increase the density, in which growth of the constituent particles above D_{cr} has to be avoided [15]. This requirement can only be partly fulfilled, as heat treatment is generally associated with grain growth. In figure 13 two hysteresis curves are drawn, one for an optimally fired specimen (curve 1), the other for a specimen with low coercive force resulting from grain growth during sintering (curve 2).

Much work has been done on studies of grain growth phenomena during sintering, and the effects on magnetic properties. As the value of D_{cr} (about 1 micron) is just within the range where the magnetic ceramics normally have their mean particle diameter before sintering, fabrication is consequently critical. Much attention has been given to the development of additions to aid in a better control of the manufacturing procedure, e.g. by retarding grain growth during sintering. Most of these additions are only of value for the specific procedure used by the manufacturer (raw materials, furnace, etc.).

The most disastrous effect on the magnetic properties arises from discontinuous grain growth during sintering. Owing to the magnetic interaction of the domains in adjacent grains, flux reversal in one grain will directly influence its surroundings and finally introduce an avalanche-like effect, lowering the coercive force considerably. Discontinuous grain growth in this material is characterized by the high growth velocity. In the hexagonal material under discussion the growth velocity in the different crystallographic directions is of especial importance. The growth velocity is largest in the basal plane, causing the crystals to be thin plates, with the c-axis perpendicular to the plate. This is shown in figure 14. The ratio of diameter to thickness is about 2 for crystallites of about 1 micron diameter, and appears to increase linearly to about 15 for discontinuously grown crystals of 500 microns diameter (figure 15). Magnetically this plate shape has significant consequences, as the effective demagnetizing field is very large for these thin plates.

Another aspect of microstructure is that the constituent particles can have

an orientation texture. In remanence the magnetization vectors of a uniaxial material like barium hexaferrite will lie in the easy direction nearest to the saturating field under the influence of the anisotropy forces. (See figure 16.) This decrease in induction, and thus in energy product, will not occur when the constituent particles are aligned with their c-axis parallel to the magnetizing field. By a special procedure, in which use is made of the magnetic anisotropy field of the material, this can actually be achieved and thus the maximum energy product increased considerably [16]. In figure 17 hysteresis curves are given for barium hexaferrite, relating to an isotropic and a crystal-oriented sample. Figure 18 shows a photomicrograph of the crystal-oriented sample.

Other interesting aspects of microstructural events during sintering, e.g. increase of texture during sintering and anisotropic shrinkage, are not discussed in this paper.

6. Single Crystals vs Polycrystalline Materials

In the preceding section an example was given where a polycrystalline material was essential for the hard magnetic properties. A single crystal can be considered as the other extreme. Domain wall processes are favoured over rotations, which is essential for soft magnetic materials. Apart from economic considerations, many difficulties arise in preparing single crystals with a controlled chemical constitution. Moreover, no satisfactory techniques have yet been developed in which single crystals of cubic materials can be grown from fluxes, as they generally contain inclusions.

Owing to the lack of a reference, e.g. a single crystal, the definite influence of small variations in the material, unknown interactions between domains and a number of other factors, it is often difficult to decide whether the microstructure actually found is essential for the physical properties measured. Therefore we will show in the following paragraphs only examples where gross effects in the physical properties are related to microstructural variations.

7. Initial Permeability and Coercive Force

The initial permeability and coercive force of a material are closely related, as both are determined by the two basic processes for magnetization. Thus they are very sensitive to porosity, size and distribution of the pores, the average size of the grains, and whether a second phase is present.

The initial permeability is determined by rotation processes or by reversible bulging of the domain walls, without changing the Weiss domain pattern as a whole. The coercive force is a mean critical field, governed by irreversible rotation processes or by irreversible domain-wall displacements. As rotation processes are determined predominantly by intrinsic properties of the material, they are fairly independent of microstructural variations and can be calculated with good approximation. It is found that the initial permeabilities of sintered specimens are much higher and the coercive forces much lower than one can expect from rotation processes alone. Thus wall displacements do contribute appreciably.

In figure 19 the initial permeability is given as a function of the porosity p of a series of nickel ferrites and of nickel-zinc ferrites [17]. The value for p=0 in this figure is the result measured on a nickel ferrite single-crystal. The value of the permeability which has been calculated for p=0 when only rotation processes occur, is about 8. It appears that the increase in permeability with decreasing porosity of the material must be attributed to an increase in the contribution of wall displacements. Also the coercive force becomes smaller with decreasing porosity, as shown in figure 20. The linear dependence found is as expected for domain-wall displacements. Presumably the sharp increase at the highest values of p is caused by the fact that single-domain behaviour is approached.

The samples with varying porosities were obtained by sintering at different temperatures. Sintering is accompanied as a rule by grain growth, which also affects permeability. In figure 21 the measurements of Guillaud [18] have been given for the initial permeability μ_8 as a function of grain size for manganese zinc ferrites with constant chemical composition. There are two inflections in the curve. The lower inflection, at about 5-6 microns, is attributed to a change from rotational permeability in small grains to a permeability due to wall displacements for larger grains. However, from recent results published by Paulus [19] on this system, it appears that also an appreciable increase in density occurs in the same region of grain sizes (see figure 22). Thus one cannot unambiguously attribute the increase

in permeability to either the decrease in number of pores or the increase in grain size. Owing to the fact that the chemical composition is very sensitive to changes in the oxygen content of the atmosphere and to evaporation of zinc oxide, ceramic technology has so far failed in this respect, as measurements should be made in a range of porosities for a given constant grain size. Also the mean pore size has to be taken into account, as the blocking of domain walls at pores is determined by the ratio of pore size to wall thickness. In the manganese-zinc ferrites an appreciable increase in the mean pore size occurs during the heat treatment.

The same considerations presumably hold for the measurements on nickel-zinc ferrites, made by the same authors. However, no measurements on one and the same chemical composition have been published.

The effects of discontinuous grain growth have not been investigated thoroughly. Guillaud [18] attributes the upper limit of the permeability in figure 21 to the appearance of pores in the crystals. According to [19] discontinuous grain growth starts in this system at about 10 microns. This can just as well be the reason for densification to stop, as is known from theories on sintering [20]. We have studied this phenomenon in a nickel-zinc ferrite, $Ni_{0.36}Zn_{0.64}Fe_2O_4$, using a material which was known to give discontinuous grain growth during sintering. In figure 23 results are given of measurements on samples made from prefired powder. The samples were heated at a constant heating rate of 250°C per hour up to the temperature given, and next rapidly cooled to 900°C. From 900°C to room temperature the samples were slowly cooled. Up to a temperature of 1200°C grain growth was very small, all grains being smaller than one micron. Sintering was appreciable, as a density of about 97.5% of the X-ray density was obtained. After 1200°C grain growth could be seen under the microscope, up to 1 or 2 microns, and above this temperature discontinuous grain growth started. A very sharp break in the density-temperature curve is seen at this temperature. In figure 24 photomicrographs are given of the etched samples after

a) the temperature of 1200°C, where grain growth is clearly visible,

b) the temperature of 1210°C, where discontinuous grain growth has started; and

c) at a much higher temperature where the new equilibrium grain size is formed.

There is no break in the permeability curve. We believe that the main effect on the initial permeability μ_o is the decrease in porosity. A further increase in permeability, when the density is constant, is obtained by the gradual disappearance of the very small grains. Apparently the domain-wall mobility which favours a high permeability is more hindered when the pores are located on the grain boundaries of the grains than when the pores are trapped within larger grains.

A second phase or inclusion should have the same influence on μ_o and H_c as a pore or void. However, because of the difference in thermal expansion of the two phases, stresses are set up in the ferrite matrix. When the material has a certain value for the magnetostriction, a stress anisotropy energy can be formed which can be relatively high with respect to the other anisotropies. This effect has been studied by Carter in magnesium ferrite [21]. The second phase was formed by partly reducing the ferrite, as the solubility of the metal oxide phase MeO in the spinel phase is generally very low. At a high content of the reduced oxide phase, stresses were high enough to crack the ferrite crystals around the inclusion.

The decrease in initial permeability and the increase in coercive force found by us in the nickel-zinc ferrites $(Ni_{0.33}Zn_{0.67}O)_{1+x}(Fe_2O_3)_{1-x}$ for $x>0$, as shown in figure 25, has to be attributed to the same effect. In these ferrites the crystalline anisotropy is very low, whereas the magnetostriction has a value still high enough to cause a sufficiently large stress anisotropy to affect the permeability and coercive force. In the range measured the volume fraction of the second phase, a divalent metal oxide, is far too low to account for the decrease in μ_o and the increase in H_c. All these specimens have a density differing from the X-ray density by less than 0.25%. Both μ_o and H_c show a perfect inverse behaviour in this case.

By a special method the internal demagnetization caused by pores can be determined experimentally. In figure 26 the internal demagnetization coefficient N_i has been plotted as a function of the porosity p. Curve a was measured for a cubic spinel (ferroxcube). The value of N_i goes to zero for p=0.

A typical effect of microstructure occurs in the hexagonal ferroxplana materials, in which the basal plane is a preferential plane for the magnetization

[22]. In a polycrystalline sample, with random orientation of the crystallites, a large demagnetizing effect arises from the strong forces which bind the magnetization vectors to the preferential plane. In figure 27 the lines of force have been drawn for a schematic situation in which the preferential planes lie within the plane of the figure, except for one crystal. The lines of force bend around this crystal, which therefore acts as an air gap. From measurements of N_i it appears that in isotropic ferroxplana materials an appreciable value for N_i remains when p=0 (curve h Fig. 26.) Thus, even in a fully dense hexagonal ferrite a virtual porosity is present, corresponding to a cubic ferrite of 30% porosity.

It is possible to give the crystallites a preferred orientation by utilising the magnetic anisotropy forces. This can result either in a "fan" texture, in which the c-axes of the crystallites lie at random in a plane (see figure 28), or in a texture as shown for barium hexaferrite (see figure 18), in which the c-axes are oriented more or less parallel. Measurements on specimens with an increased degree of orientation f, in which f = 0 for random and f = 1 for parallel orientation of the c-axes, show the expected decrease of N_i, as shown by curve c in figure 26. The technically important effect is a large increase of the permeability, mainly resulting from this decrease of N_i, as shown in figure 29.

8. High-Frequency Behaviour

Up till now we have only discussed the static magnetic properties of magnetic ceramics. Except for the permanent magnets, their practical usefulness is at high frequencies and we shall discuss some of the microstructural aspects of the high-frequency behaviour. We shall limit our discussion to the properties up to radio frequencies.

A sinusoidal field gives an induction that lags behind the field in time. This time lag gives rise to losses, expressed as the loss angle tan δ. In low-induction applications one is primarily interested in the quality factor $Q = 1/\tan \delta$. The losses can be divided into hysteresis, eddy-current and residual losses. Because of the complexity of the physical relation between these losses and the microstructural characteristics of the ferrite, only some view-points will be brought forward.

For low hysteresis losses a homogeneous structure seems to be necessary. With less uniform grain size distribution and with grains having pores enclosed, the hysteresis losses are greatly increased [18], [23].

The eddy-current losses in most ferrites are negligible, unless the ferrous content is high. Ferrous ions lower the resistivity of ferrites considerably. In manganese-zinc-ferrous ferrites, which have the most useful properties for many applications (especially for telecommunications) up to frequencies of about 1Mc/s, the ferrous content is essential for the specific magnetic properties desired. The low resistivity, about 10-100 $\Omega \cdot$cm, caused by this ferrous content results in eddy-current losses which are relatively high, compared to the other magnetic losses. A peculiar effect is the decrease in the eddy-current losses when Ca-ions are added in a quantity of about 0.1 mole-% [18,24]. The preference for the Ca-ions to be located at grain boundaries was concluded from several experiments. It was also shown that the resistivity measured within the individual grains is lower than the resistivity measured across the grain boundaries; when Ca-ions are present the difference is much larger (Fig. 30). During cooling of these ferrites a reoxidation occurs. The addition of Ca-ions apparently brings about the appearence of an open porosity, so that quick reoxidation can also occur at the core of the specimen. Although the reoxidation of the bulk of the crystals is increased as compared with specimens in which no Ca-ions are present, the main effect is the high state of oxidation at the grain boundaries if Ca-ions are present.

Little effective work has been done on the influence of microstructure on residual losses. Among many other factors, domain-wall relaxation processes definitely seem to have an influence, especially when inhomogeneities are present. The same holds for the losses in those applications where high inductions are used (transformer cores) and thus irreversible wall movements play a preponderant role.

It appears that every group of materials has its optimum frequency range where it can be used. The upper frequency limit is given by the so-called natural resonance frequency, where the losses increase sharply. In fig. 31 the relative loss factor tan δ / μ is given for different classes of ferrites, as a function of frequency.

The very soft manganese-zinc-ferrous ferrite show excellent magnetic properties in the lower frequency range. The high permeability in these materials is caused by a large contribution from wall movements [18]. In this lower frequency range, wall mobility is apparently high enough to cause no losses.

In the higher frequency ranges, however, wall mobility is generally not sufficiently high. To obtain reasonably low losses at these high frequencies only moderate permeabilities can be used, in which no large contribution from domain wall movements is present. Although both small grain size and a finely divided porosity within the grains are effective to make low-loss materials for these high frequencies, the most effective way to obtain low losses is by completely freezing the domain walls by the substitution of a few percent of cobalt ions.

9. Conclusion

The world production of magnetic ceramics is rapidly increasing. It is now about 12,000 tons a year with a value of about $30,000,000. In the foregoing the discussion has been limited to several groups of magnetic ceramics, in which the microstructure had a clear influence. This relationship is most straightforward in the ceramic permanent magnetic materials. A clear relationship is also found with the properties of the static hysteresis loop. For the magnetic properties measured under dynamic conditions, the number of other factors influencing these properties increases. As many of them are physically not well understood, it is more difficult to establish a clear relationship between these phenomena and the microstructure.

Ceramic technology can supply the methods and tools necessary for achieving certain required microstructures, also for fundamental studies of the physical phenomena. Hot-pressing undoubtedly is one of these methods [25].

There are several other applications in which specific properties of ferrites form a keypoint. Ferrites for radar and microwave communication components require a very low porosity [26]. The same holds for ferrites used in magnetostrictive transducers. In recent times the study of ferrites with square hysteresis loops, as used in memory cores, has been directed to the microstructure with more success than before [27]. Further studies of the fundamental aspects in those fields of the technology of magnetic ceramics, which determine the microstructure, will certainly help both to provide a better understanding of the physical properties and a better control of their fabrication.

The author thanks his collegues Dr. G.H. Jonker, Dr. E.W. Gorter, A. Broese van Groenou and C. Kooy for critically reviewing the manuscript.

References

[1] J.L. Snoek, New Developments in Ferromagnetic Materials, Elsevier Publishing Comp. New York-Amsterdam (1947).

[2] E.J.W. Verwey and E.L. Heilmann, Physical Properties and Cation Arrangement of Oxides with Spinel Structures, J.Chem. Phys. 15, 174-180 (1947).
E.J.W. Verwey, P.W. Haaijman and F.C. Romeyn, Physical Properties and Cation Arrangement of Oxides with Spinel Structures, J.Chem.Phys.15, 181-187 (1947).

[3] L. Néel, Propriétés magnétiques des ferrites: Ferrimagnétisme et Antiferromagnétisme, Ann. de Phys. 3, 137-198 (1948).

[4] C. Guillaud and H. Creveaux, Préparations et propriétés magnétiques des ferrites de manganese et de cobalt, Compt.Rend.Ac.Sc.Paris, 230, 1256-1258 (1950).
C. Guillaud, Propriétés magnétiques des ferrites, J.Phys.Rad., 12, 239-248 (1951).
C. Guillaud and H. Creveaux, Propriétés Ferromagnétiques des Ferrites Mixtes de Cobalt et de Zinc et de Manganèse et de Zinc, Compt. Rend.Ac.Sc.Paris, 230, 1458-1460 (1950)
C. Guillaud and M. Sage, Propriétés Magnétiques des Ferrites Mixtes de Magnesium et de Zinc, Compt. Rend. Ac.Sc.Paris, 232, 944-946 (1951)
E.W. Gorter and J.A. Schulkes, Reversal of Spontaneous Magnetization as a Function of Temperature in LiFeCr Spinels, Phys.Rev.,90 (3), 487-488 (1953).

[5] E.W. Gorter, Some Properties of Ferrites in Connection with their Chemistry, Proc. I.R.E. 43, 1945--1973 (1955).

[6] J. Smit and H.P.J. Wijn, Ferrites, Philips Technical Library, 1959.

[7] P. Weiss, L'Hypothèse du Champ Moléculaire et la Propriété Ferromagnétique, Journ. de Phys. 6, 661-690 (1907)

[8] F. Bloch, Zur Theorie des Austauschproblems und der Remanenzerscheinung der Ferromagnetika, Zeit.f.Physik, 74 295-335 (1932).

[9] C. Kooy and U. Enz, Domain Configuration in Layers of $BaFe_{12}O_{19}$, Philips Res.Repts. 15 (1), 7 - 29 (1960).

[10] I. Hanke und W. Metzdorf, Abbildung magnetischer Bereichs-strukturen von Ferriten mit Hilfe des magnetooptischen Kerr-Effekts, Z. angew. Phys.15 (2), 191-192 (1963).

[11] A. Broese van Groenou, private communication.

[12] C. Kittel, Phys.Theory of Ferromagnetic Domains, Rev.Mod.Phys. 21 (4), 541-583 (1949).

[13] S.L. Blum, Microstructure and Properties of Ferrites, J.Am.Ceram.Soc.41 (11), 489-493 (1958).

[14] J.J. Went, G.W. Rathenau, E.W. Gorter and G.W. van Oosterhout, Ferroxdure, a Class of New Permanent Magnet Materials, Philips Techn. Rev. 13, 194-208 (1951/52).

[15] A.L. Stuijts, Sintering of Ceramic Permanent Magnetic Material, Trans.Brit. Ceram.Soc. 55, 57-74 (1956)

[16] A.L. Stuijts, G.W. Rathenau and G.H. Weber, Ferroxdure II and III, Anisotropic Permanent Magnet Materials, Philips Techn. Rev.16, 141-147 (1954).

[17] Reference[6] page 245.

[18] C. Guillaud, The Properties of Manganese-Zinc Ferrites and the Physical Processes Governing Them, Proc.Inst.Electr. Engrs.104B, 165-173 (1957).

[19] M. Paulus, Influence des pores et des inclusions sur la croissance des cristaux de ferrite, Phys.Stat.Sol. 2, 1325-1341 (1962)

[20] J.E. Burke, Role of Grain Boundaries in Sintering, J.Am.Ceram.Soc., 40, 80--85 (1957).

[21] R.E. Carter, Effect of Oxygen Pressure on Microstructure and Coercive Force of Magnesium Ferrite, J. Am.Ceram.Soc., 41 (12), 545-550 (1958).

[22] A.L. Stuijts and H.P.J. Wijn, Crystal-Oriented Ferroxplana, Philips Techn. Rev. 19, 209-217 (1957/58).

[23] W. Heister, Magnetic Properties and Grain Structure of Mn-Zn Ferrites, J.Appl.Phys. 30 (4), 22S-24S (1959)

[24] M. Paulus et Ch. Gaullaud, Structure Granulaire et Propriétés des Ferrites, J.Phys.Soc. Japan, 17, Suppl. B-I, 632-640 (1962). Proc. Int.Conf.Magnetism and Crystallography, 1961, Kyoto.

[25] W.W. Malinofsky and R.W. Babbitt, Fine-Grained Ferrites. I. Nickel Ferrite, J.Appl.Phys. 32 (3), 237S-238S (1961).
W.W. Malinofsky, R.W. Babbitt and G.C. Sands, Fine-grained Ferrites, II, $Ni_{1-x}Zn_xFe_2O_4$. J. Appl.Phys. 33 (3), 1206-1207 (1962).

[26] A.L. Stuijts, J. Verweel and H.P. Peloschek, Dense Ferrites and Their Applications, Proc.Intern. Conf. on Nonlinear Magnetics, Washington, April 17-19, 1963; I.E.E.E. Spec. Publ. T-149.

[27] J.E. Knowles, Philips Techn. Rev., 24, 242-251 (1962/63).
P.D. Baba, E.M. Gyorgy, and F.J. Schnettler, Two-Phase Ferrites for High-Speed Switching. J.Appl. Phys., 34 (4), 1125-1126 (1963).
E.A. Schwabe and D.A. Campbell, Influence of Grain Size on Square-Loop Properties of Lithium Ferrites, J.Appl.Phys., 34 (4), 1251-1253 (1963).

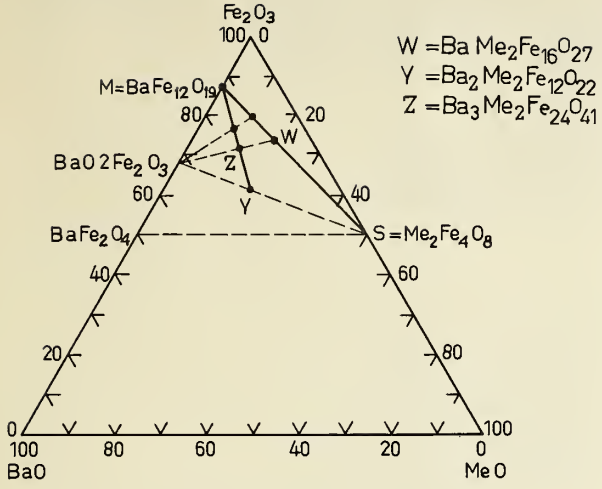

FIGURE 1. Composition diagram for the ferromagnetic ferrites. Me is a divalent ion or a combination of divalent ions.

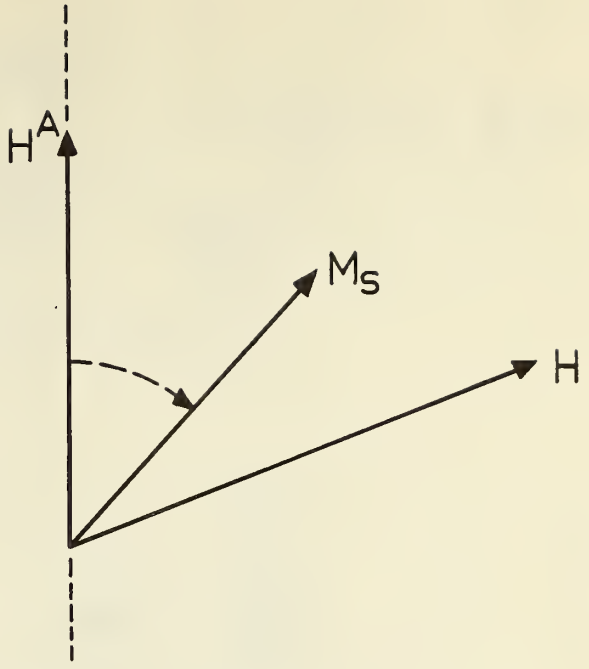

FIGURE 2. Change of the direction of the magnetization vector M_s in an applied field H.

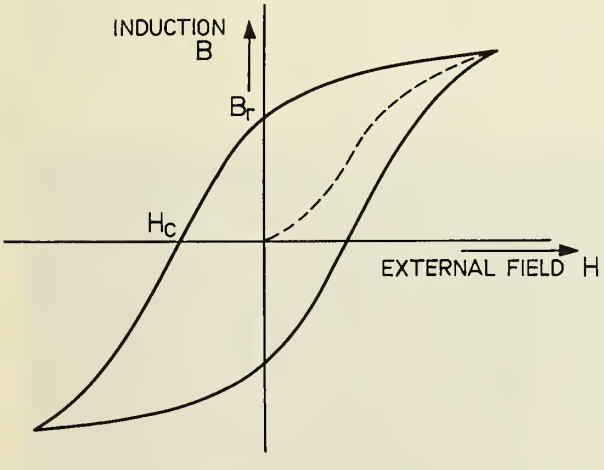

FIGURE 3. Hysteresis loop of a magnetic material.

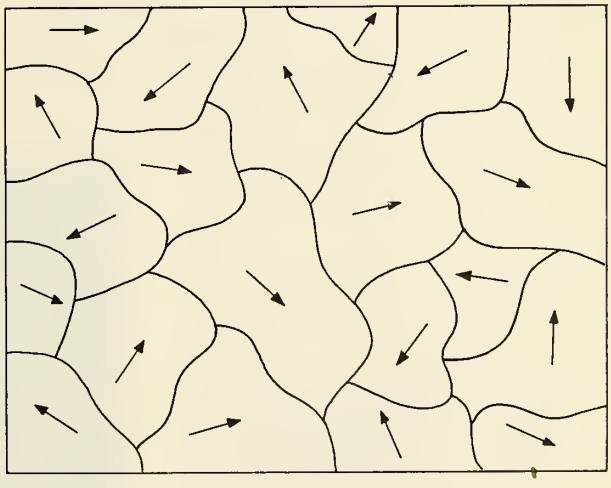

FIGURE 4. Weiss domains in a ferromagnetic material. Unmagnetized state.

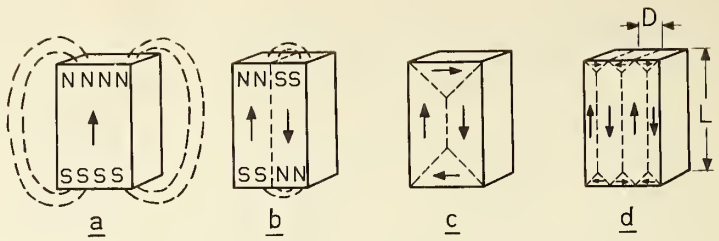

FIGURE 5. Examples of Weiss domain configurations.

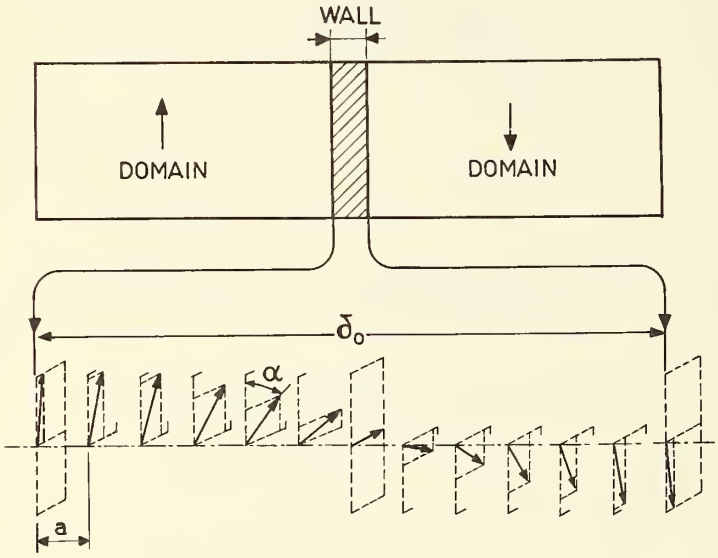

FIGURE 6. Spin configuration inside a Bloch wall.

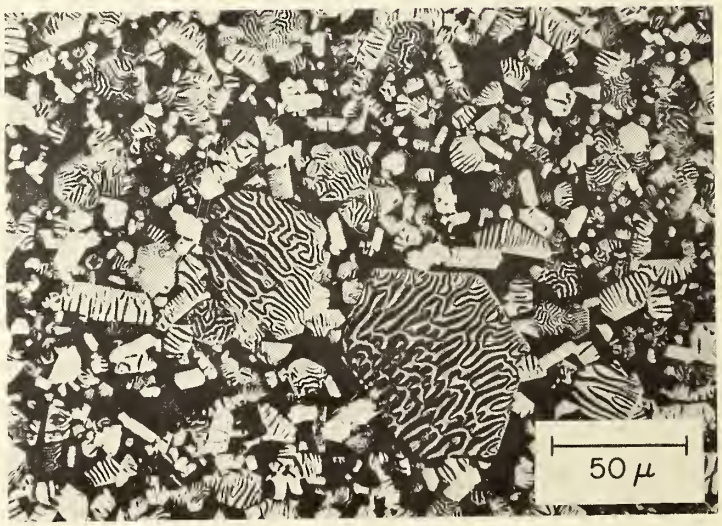

FIGURE 7. "Bitter" powder pattern on crystals of $BaFe_{12}O_{19}$, embedded in a glassy phase (courtesy of G. H. Jonker).

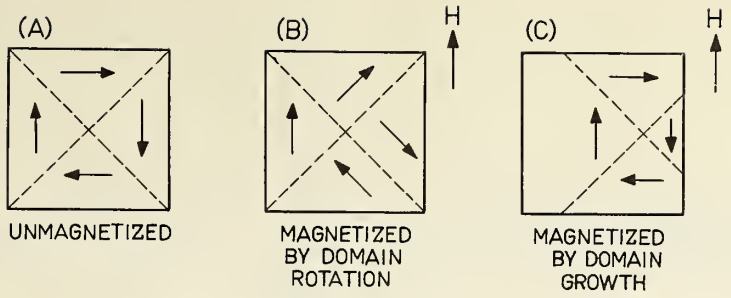

FIGURE 8. Magnetization Processes: (a) unmagnetized state; (b) magnetized by domain rotation; (c) magnetized by domain growth.

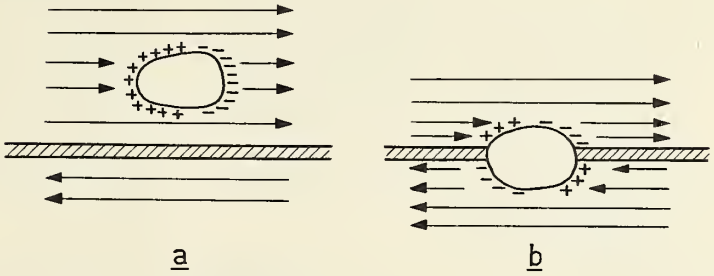

FIGURE 9. Decrease of demagnetization energy when a domain wall intersects a pore or inclusion.

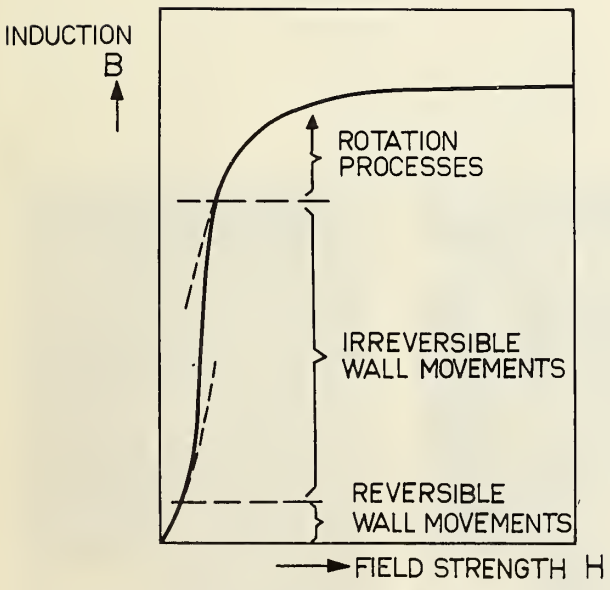

FIGURE 10. Different magnetization processes along the magnetization curve.

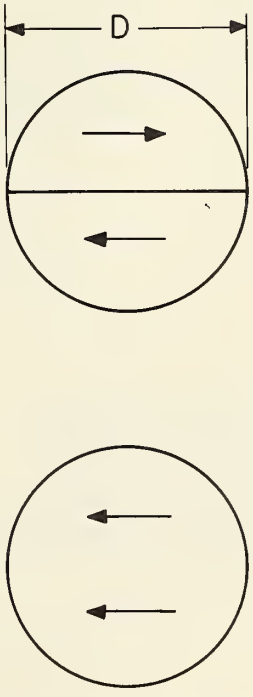

FIGURE 11. Magnetization in a small particle without and with a Bloch wall.

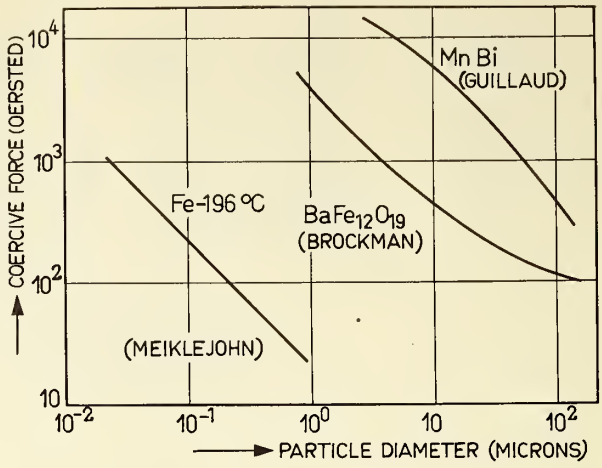

FIGURE 12. Coercive force H_c as a function of particle diameter for iron, $BaFe_{12}O_{19}$ and manganese bismuth.

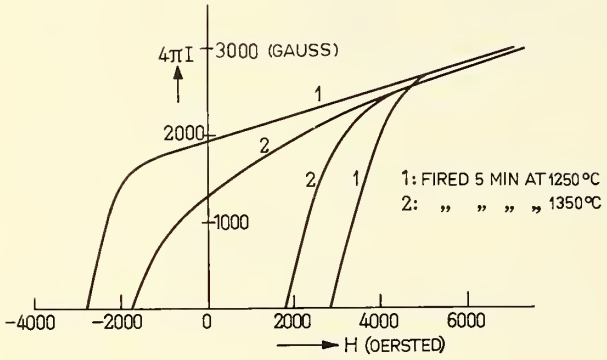

FIGURE 13. Upper half of the hysteresis loop for $BaO \cdot 6Fe_2O_3$ with random crystal orientations.

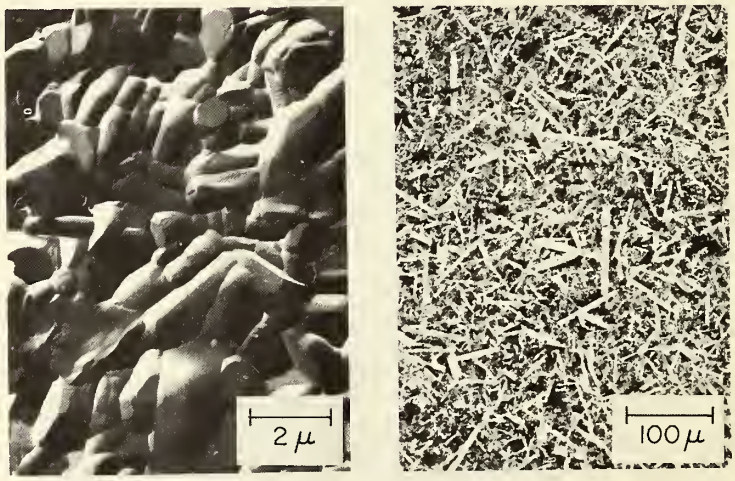

(a) (b)

FIGURE 14. Photomicrographs of sintered specimens of polycrystalline $BaO \cdot 6Fe_2O_3$ showing a) grain size for optimum magnetic properties and b) discontinuous grain growth.

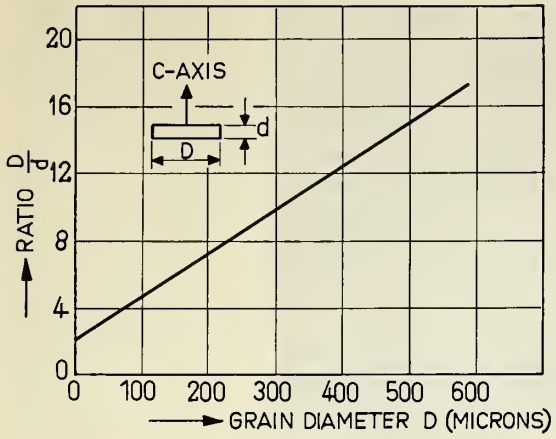

FIGURE 15. Ratio of diameter to thickness of discontinuous grown grains in sintered $BaO.6Fe_2O_3$ as a function of grain diameter D.

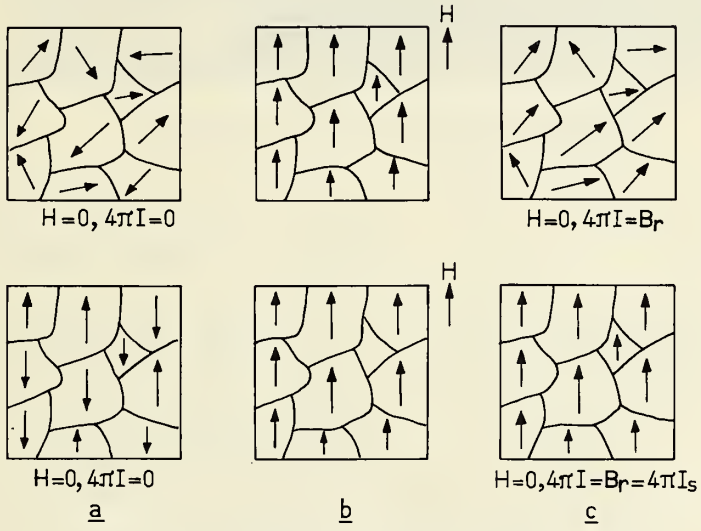

FIGURE 16. A sintered mass of barium hexaferrite a) unmagnetized, b) magnetized in a field H and c) converted into a permanent magnet.
Upper row: crystallites in random orientation; bottom row: parallel-oriented crystallites.

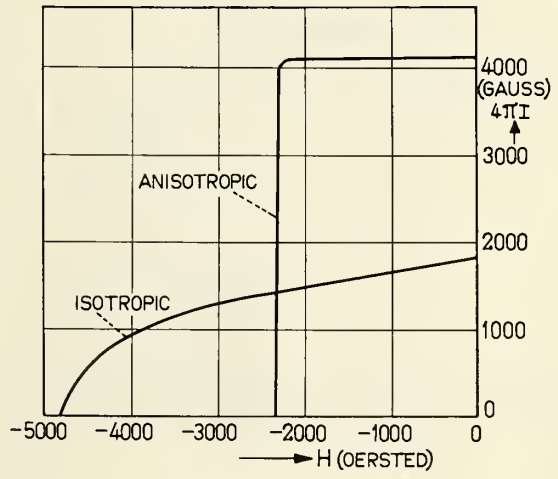

FIGURE 17. Demagnetization curves of barium hexaferrite for a) isotropic and b) crystal-oriented sample.

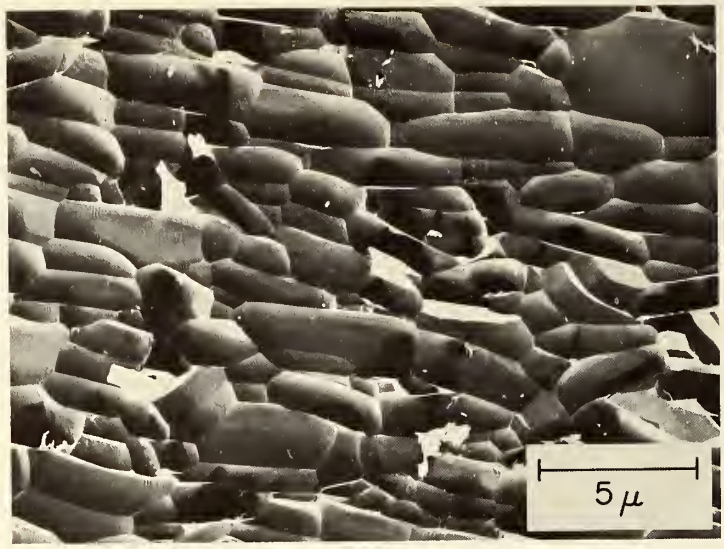

FIGURE 18. Photomicrograph of a crystal-oriented barium hexaferrite sample, thermally etched.

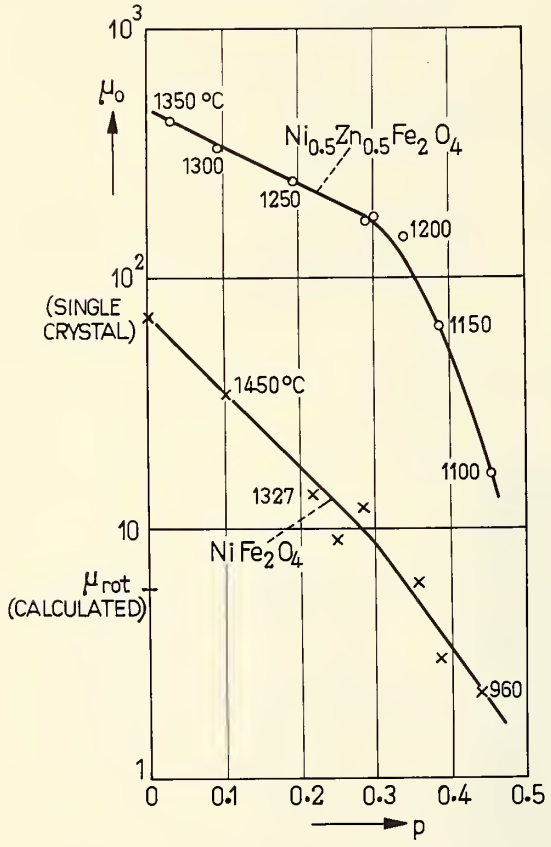

FIGURE 19. Variation of the initial permeability μ_o with the porosity p for $NiFe_2O_4$ and $Ni_{0.5}Zn_{0.5}Fe_2O_4$. (After Smit en Wijn [17]).

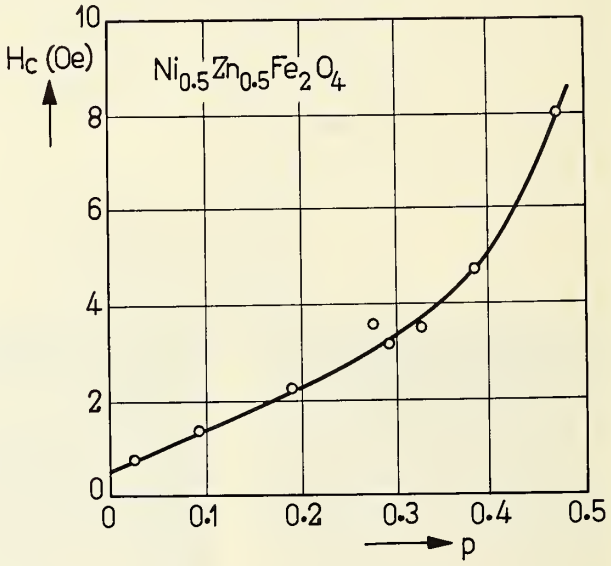

FIGURE 20. Variation of the coercive force H_c with the porosity p of a series of nickel-zinc ferrites. (After Smit and Wijn [6]).

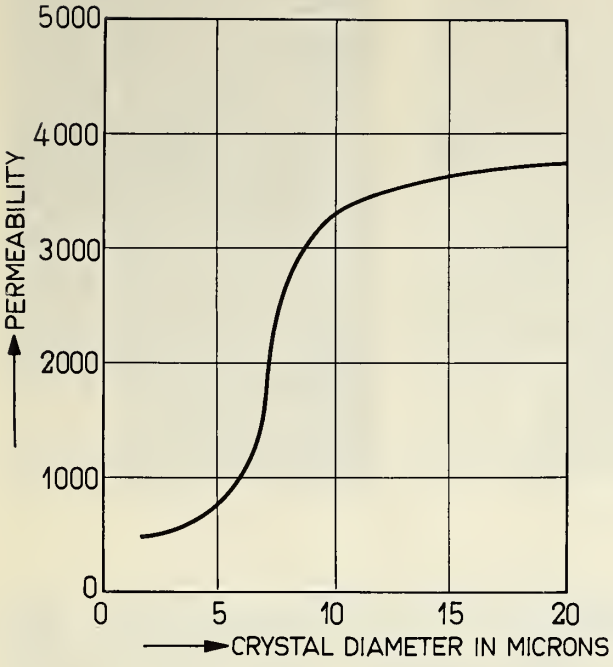

FIGURE 21. Variation of the initial permeability μ_o with grain diameter in manganese-zinc ferrites. (After Guillaud [18]).

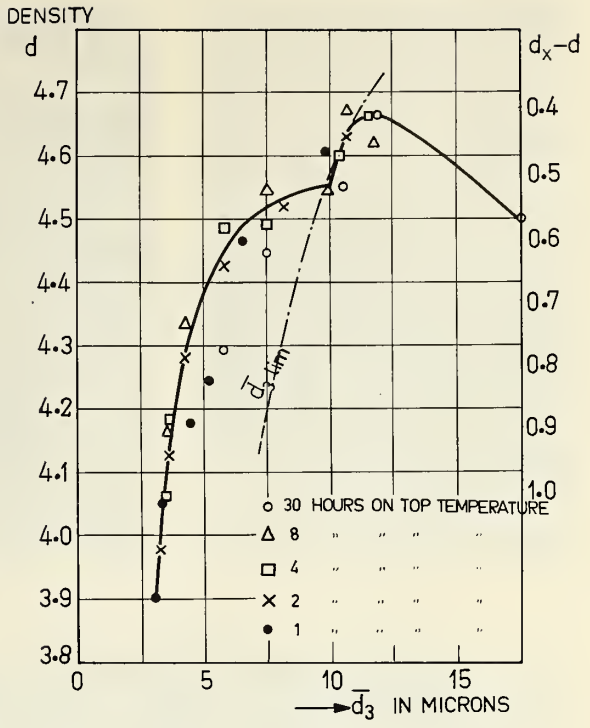

FIGURE 22. Density of manganese-zinc ferrite, with the same chamical composition as those in fig. 21, as a function of the mean diameter of the grains. (After Paulus [19]).

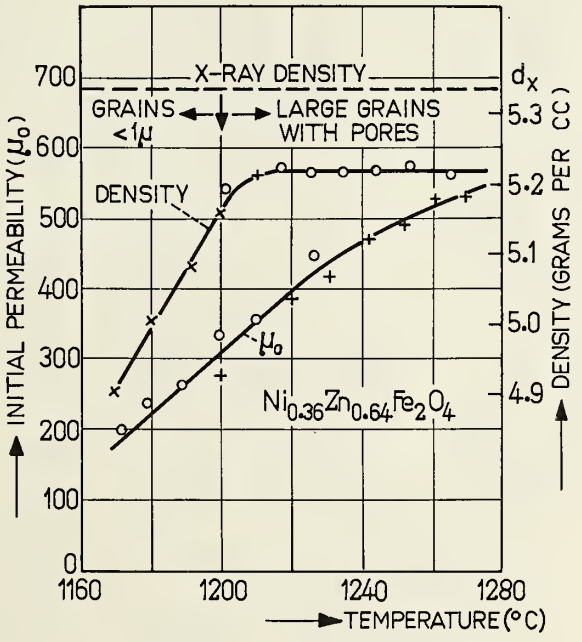

FIGURE 23. Initial permeability and density as a function of the temperature to which the samples have been heated. Heating-rate 250°C/hr.

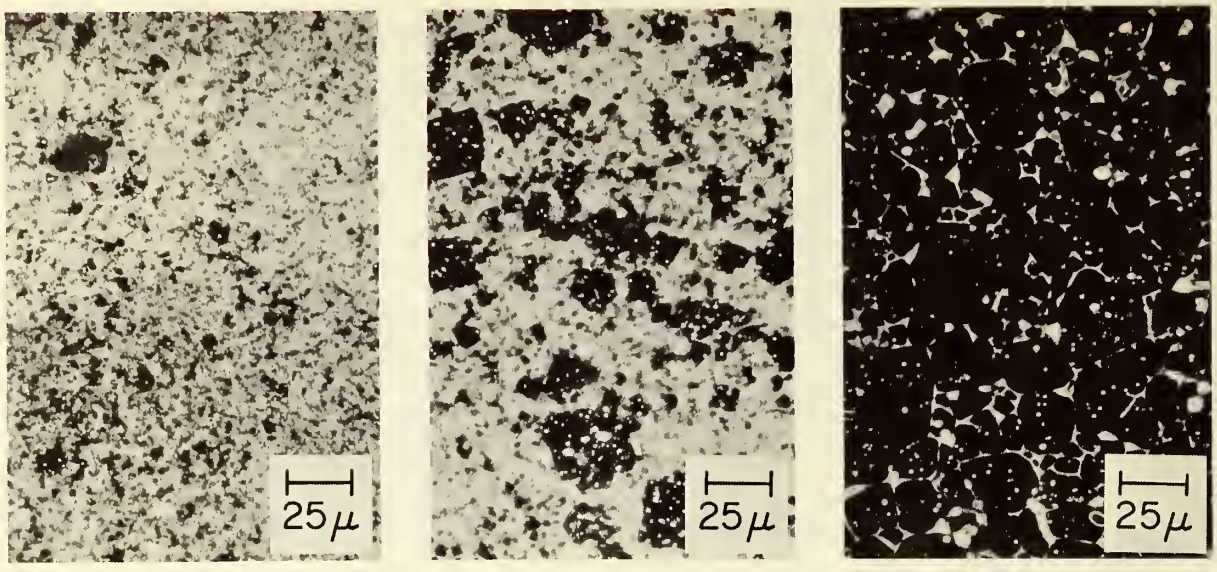

FIGURE 24. Photomicrographs of samples from fig. 23 at a) 1200°C, b) 1210°C and c)~1270°C.

FIGURE 25. Initial permeability μ_o, coercive force H_c and density for a range of nickel-zinc ferrites with excess metal oxide. All the specimens are very near to X-ray density.

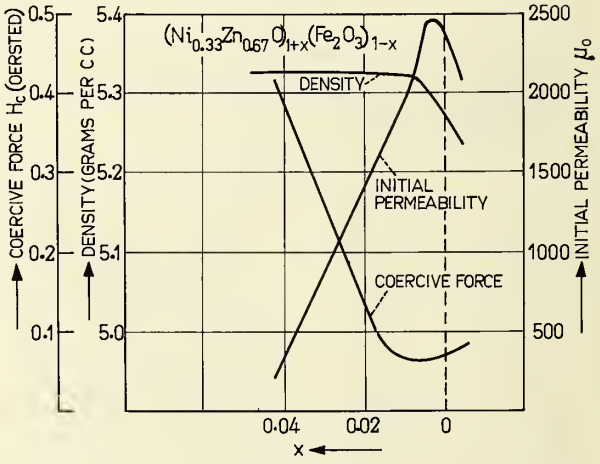

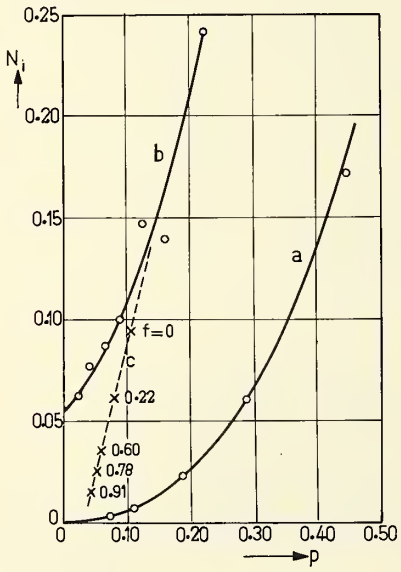

FIGURE 26. Internal demagnetization coefficient N_i as a function of the porosity p: a) for ferroxcube; b) for isotropic ferroxplana; c) for crystal-oriented Co_2Z with different degree of orientation f.

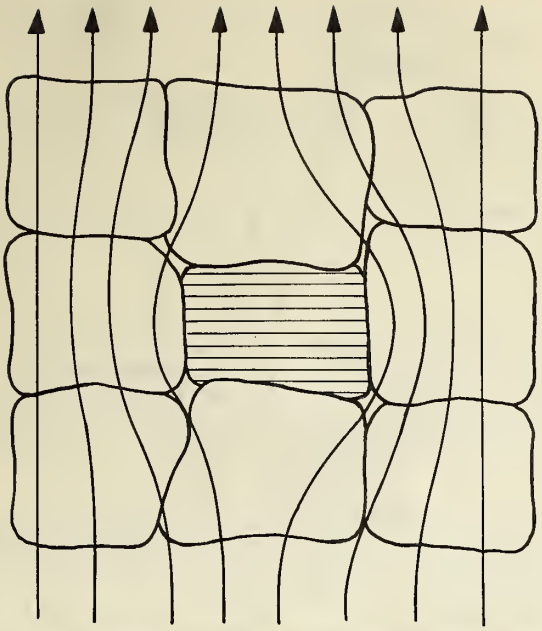

FIGURE 27. Demagnetizing effect of a crystal whose basal plane (hatched) is at right angles to the magnetic flux.

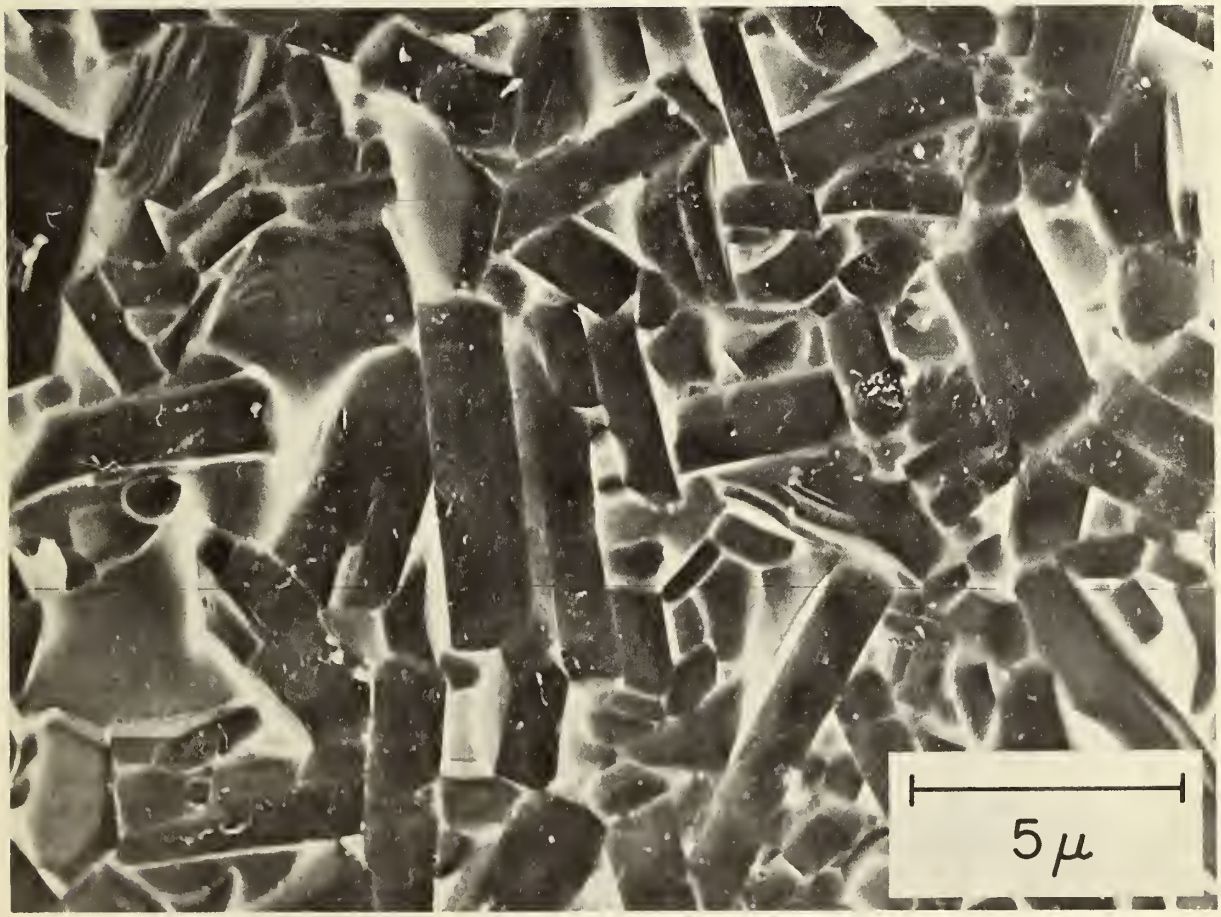

FIGURE 28. Photomicrograph of a ferroxplana material with "fan" texture. The c-axes of the crystallites lie at random in the plane of the figure (thermally etched).

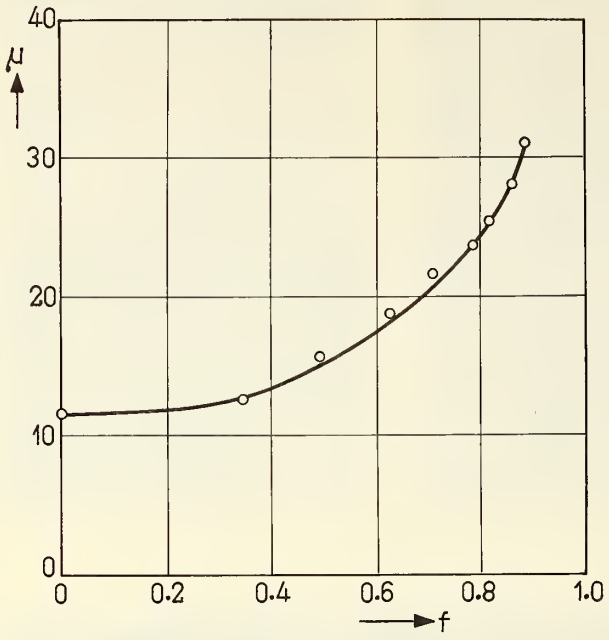

FIGURE 29. Initial permeability μ_o of Co_2Z ($Ba_3Co_2Fe_{24}O_{41}$) with different degree of orientation f.

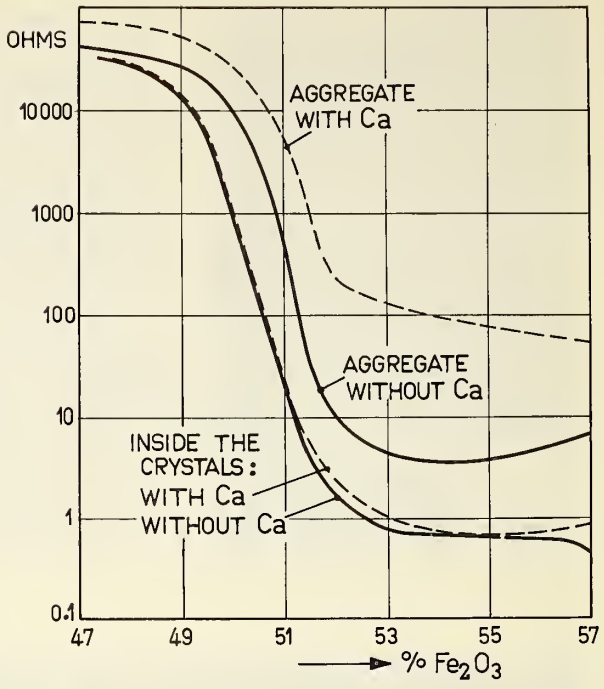

FIGURE 30. Resistivity of manganese-zinc ferrites, with and without Ca-addition, as a function of the Fe_2O_3-content. (After Paulus and Guillaud [24]).

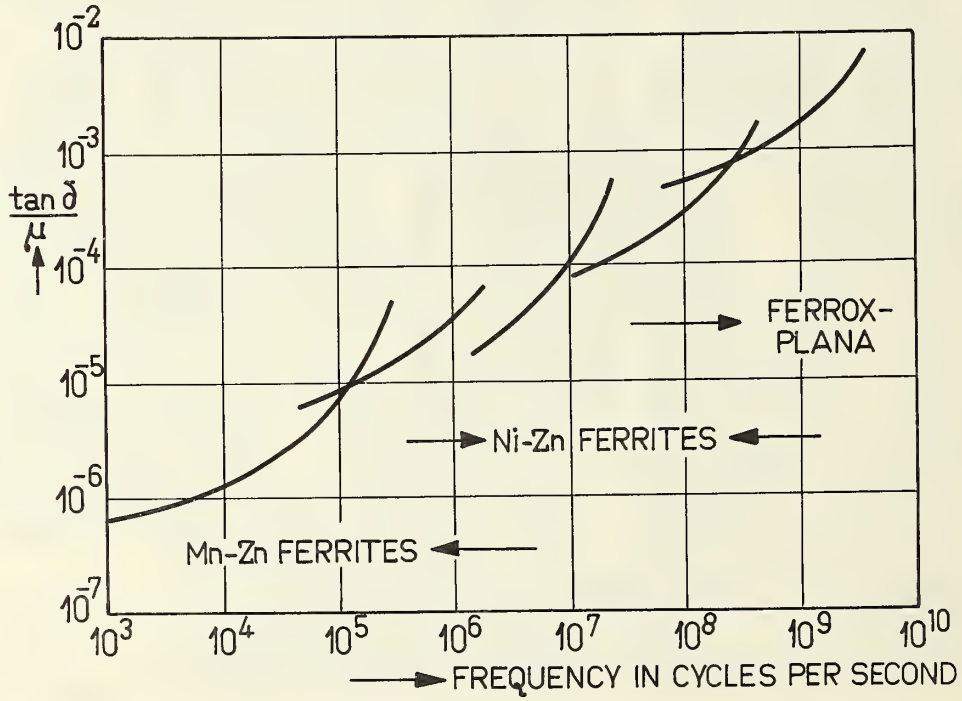

FIGURE 31. The relative loss factor $\tan \delta/\mu$ for different groups of ferrites as a function of frequency.

Microstructure of Porcelain

Sten T. Lundin

1. Introduction

The principal raw materials in the manufacture of porcelain are kaolin clay, feldspar and quartz. The primary purpose of these three components may be described rather roughly in the following way. The clay gives the body the necessary plasticity during forming and cohesion during drying. The feldspar acts as a flux and glass former in the firing, and the quartz is a filler material ensuring less shrinkage and more stability to the body during firing.

The bodies pass through several processes on their way to the final product, the most important being forming, drying and firing. The composition of a body is not determined only by the desired properties of the material in the finished product, but also by the properties required of the body during the different phases of manufacture. The composition of the body may vary considerably according to the purpose of the product [8][1]. However, we will not discuss the differences between various types of triaxial whiteware bodies here, but will deal with the common characteristic features of their microstructure.

We are interested in the microstructure of the porcelain as it determines the material properties. The things we want to know about the microstructure are the nature, quantity and distribution of phases and pores. We also want to know the degree of inhomogeneity in the glass phase, and the structural stresses present in the different phases.

I will here give a review of our present knowledge and at the same time also try to explain why the microstructure looks the way it does.

2. Composition of Porcelain

In table 1 the normal composition range of the raw body is given together with the chemical composition of the fired bodies. If the raw materials in the bodies are pure kaolinite, potash feldspar and quartz, the total system after dehydration can be represented in the ternary system K_2O-Al_2O_3-SiO_2, for which Schairer and Bowen have given the equilibrium diagram [14, 15]. But technical bodies always have more than these three components, and these minor constituents are important, for they have a great influence on the changes during firing. In the absence of data on the multicomponent systems, Shelton has suggested converting the extra components to equivalent contents of the main components similar in character [17].

The phases occurring in triaxial whiteware bodies are normally mullite $3Al_2O_3 \cdot 2SiO_2$, quartz and a glass phase. In addition cristobalite may sometimes be present as a fourth phase in bodies with a high percentage of quartz. The nature and percentages of the crystalline phases can be determined by X-ray diffraction analysis. As a rule technical porcelain contains about 10 - 25 per cent mullite, 5 - 25 per cent quartz, and 65 - 80 per cent glass. The glass phase is thus the major part of the porcelain. In addition, there are always pores in whiteware bodies. Even when the bodies are fired to impermeability, a porosity of 4 - 8 per cent remains as closed pores.

---

[1] Figures in brackets indicate the literature references at the end of this paper.

TABLE 1 Composition Range of Porcelain

A. Components in the raw body

	per cent
China clay	30 - 60
Ball clay	
Feldspar	25 - 35
Quartz	10 - 40

B. Chemical composition of the fired body

	per cent	Shelton's grouping
SiO_2	70 - 80	RO_2
TiO_2	< 1	RO_2
Al_2O_3	15 - 25	Al_2O_3
K_2O	2 - 5	R_2O
Na_2O	1 - 2	R_2O
CaO	< 1	R_2O
MgO	< 1	R_2O
Fe_2O_3	< 1	R_2O

C. Phase composition of the fired body

	per cent
Mullite	10 - 25
Quartz	5 - 25
Cristobalite	0 - 10
Glass	65 - 80

3. Appearance of the Microstructure in the Optical Microscope

The microstructure of porcelain may be studied by different methods, but the replica technique on polished and etched specimens is the simplest one and gives the best results. A photomicrograph of an electrical insulator porcelain is shown in figure 1. This is a general picture with a magnification of about 400x taken on a collodion replica with transmitted light. The micrograph shows that porcelain is a very heterogeneous material with the crystalline phases rather unevenly dispersed in a continuous glass matrix.

Reminiscences of the original boundaries of the quartz and feldspar grains in the raw body can be distinguished in the micrograph. In this porcelain an extensive dissolution of the quartz grains has occurred as shown by the wide solution rims. Of the mullite phase, only the larger of the crystals which have grown in the feldspar relicts can be seen. No formation of cristobalite is found in this sample. The pores of the porcelain are indicated by black areas in the micrograph.

The occurrence of cracks around and even within the quartz grains can easily be seen. Most or nearly all of these cracks do not exist in the untreated porcelain material but are formed during the preparation of the specimen in the grinding and polishing operations by the release of microstresses within the quartz grain and the surrounding glass phase. These stresses are due to the great difference in the thermal expansion coefficient between the crystalline quartz and the glass phase.

The information obtained from this type of micrograph is mainly concerned with the grain size distribution of the quartz and feldspar components and their blending in the raw body, the degree of dissolution of the quartz, and the orientation effects present.

Figure 2 shows the microstructure of another electrical insulator porcelain with a higher quartz percentage and less quartz solution, and figure 3 the structure in a vitreous sanitary ware at higher magnification. The firing temperatures have here been too low to give an appearence of the individual mullite crystals.

In figure 4, showing the structure of a porcelain fired at higher temperature, mullite crystals can be seen in the feldspar relicts but not in the clay matrix. Some of the quartz grains have started transformation into cristobalite.

4. Appearance of the Microstructure in the Electron Microscope

Only a small part of the mullite phase can be observed by the optical microscope, owing to the extremely small size of the mullite crystals. In order to determine the quantity and distribution of the mullite phase the replica method has to be used in connection with the electron microscope.

Figures 5a and 5b show electron micrographs of an electrical porcelain at a magnification of about 2500. We see here still more strikingly that the original composition of the raw body with respect to quartz, feldspar and clay determines the distribution of the crystalline phases in the fired product. The appearance of the mullite phase in the feldspar relicts is as distinct as can be desired, for the mullite crystals isolated by the etching have stuck to the replica. The mullite phase in the original clay fields has a different appearance. The mullite crystals are here present in more compact aggregates, and the isolated crystal layer in the surface does not stick to the stripped replica, which, therefore, has an uneven surface at these places.

The mullite crystals in the original feldspar and clay fields are different in size, shape and degree of aggregation. This is due to the different formation conditions of the mullite phase in these two types of fields. In order to understand this, we must study the reactions during the firing of the body.

5. Changes during Firing

First a short survey will be given of the different processes that occur in the structure during the firing of the body. Then the high temperature changes resulting in the mullite phase distribution, the quartz grain dissolution, and cristobalite formation will be discussed in connection with the ternary diagram, K_2O-Al_2O_3-SiO_2.

In the raw body, relatively large quartz and feldspar grains are surrounded by clay crystal plates and stacks. Thus the contact surfaces consist of quartz-kaolin and feldspar-kaolin, but only exceptionally of quartz-feldspar. Then the potash feldspar always contains some albite or soda feldspar.

When the body is heated, the chemically bound water in the kaolin clay is expelled at 500-600°C giving a metakaolin phase $Al_2O_3 \cdot 2SiO_2$ [1]. The next change occurs at 700-1000°C in the feldspar, where the mixed alkali feldspars are transformed into the homogeneous high temperature form sanidine [12].

Brindley and Nakahira [2] showed in their excellent work (1959) that the metakaolin phase at 925-950°C condenses to a spinel type phase $2Al_2O_3 \cdot 3SiO_2$ and amorphous silica.

A melt phase begins to form in the same temperature interval by boundary reaction between sanidine and the amorphous silica in the clay relicts. For a potash feldspar with 20 per cent albite this occurs already 60° below the eutectic temperature of 985°C in the ternary system K_2O-Al_2O_3-SiO_2 [11]. But at these low temperatures the diffusion rates are very low, and thus the melt formation proceeds very slowly in the beginning. The alkali liberated in the feldspar reaction starts diffusing into the clay relicts. The sintering of the body also starts with the melt formation, very slowly at first, but accelerating as the proportion of melt increases and its viscosity is lowered.

At about 1000-1050°C the mullite phase begins to develop in the clay phase relicts from the spinel type phase with further discarding of silica. At a somewhat higher temperature the mullite phase also begins to develop in the feldspar relicts by crystals growing from the boundaries.

At about 1200°C the mullite phase is completely developed in the clay relicts and normally also in most of the feldspar relicts. During the continued firing at higher temperatures, recrystallization of the mullite phase continues resulting in larger crystals.

The quartz phase has a very low reactivity and the grains are not noticeably affected by the other components below 1200°C. But about this temperature the dissolution of the quartz grains begins developing solution rims of crystal-free glass. If enough quartz is present to saturate the melt, the quartz dissolution stops and the quartz begins to transform into cristobalite.

When the temperature is decreased during the last part of the firing, there is a small increase in the mullite content due to crystallization from the melt. No other crystallization occurs, and the melt now forms the glass phase in the porcelain.

6. The Use of the Phase Diagram K_2O-Al_2O_3-SiO_2

Several attempts have been made to describe the changes occurring during firing and also to explain the microstructure, starting from the equilibrium diagram of K_2O-Al_2O_3-SiO_2, and using Shelton's grouping [3, 5, 11, 17].

Equilibrium concerning the total system in a triaxial whiteware body is never attained at any point in the current firing schedules. Not even the polymorphic forms of the silica corresponding to equilibrium are present at high temperatures. Nor does the melt crystallize to tridymite and potash feldspar during the cooling of the body. However, the proportions of mullite phase and melt can be estimated satisfactorily from the diagrams. This fact, combined with a consideration of the relative rates of the different process elements, makes the diagram very useful for describing some of the reaction changes at high temperatures.

But trying to predict from the ternary diagram the quantity of melt in the body at temperatures below 1100 - 1200°C gives great divergence from experimental data. There are two reasons for this. First the active phases do not correspond to the equilibrium phases (the presence of the spinel phase and the absence of a leucite phase) and second the presence of Na_2O lowers the liquidus surfaces appreciably. At these temperatures the melt formation is not an equilibrium state problem but instead a rate problem.

It is not until the feldspar phase has disappeared and the mullite phase formed that the changes in the phase composition of the body can be represented advantageously in the ternary diagram. Here the use of the diagram will be demonstrated for two cases, (a) an explanation and estimation of the mullite content in different fields and (b) for describing the change in melt composition during the quartz grain dissolution [11].

7. Formation and Distribution of the Mullite Phase

The diffusion processes within the reaction layer between the feldspar and the clay relict will be determined by the concentration gradients and the diffusion rates of the components.

The formation of the mullite phase and its distribution between the clay relicts and the feldspar relicts will thus be determined by the relative magnitude of the diffusion rates of K_2O and Al_2O_3 components, and by the contact surface and diffusion distances, i.e. the grain size and grain distribution of the feldspar phase.

The alkali, which diffuses over to the clay phase relicts, there accelerates the formation of the mullite phase. The mullite phase is formed first within the clay phase relicts beginning at about 1050°C by discard of silica from the cubic spinel phase. When the alkali content in the melt of the feldspar relicts is reduced sufficiently and the melt becomes supersaturated with mullite, the mullite phase in the feldspar relicts begins to form from nuclei and already existing mullite crystals at the original grain boundary feldspar-kaolinite. The growth is determined here by the type and direction of the crystal surfaces. The growth is most rapid on [001] surfaces directed toward the inner part of the feldspar relicts, and the mullite phase within the feldspar fields thus acquires its characteristic appearance of a great number of crystal needles running outwards from the original grain boundary toward the inner parts of the feldspar relicts (figure 6a).

On the basis of the simplifying approximation that the mass transfer of Al_2O_3 may be ignored compared with the mass transfer of alkali over the grain boundaries, the distribution of the mullite phase between the clay and the feldspar relicts after completed reaction can be estimated from the equilibrium diagram.

Let us study the conditions in a particular body, consisting of 50 per cent kaolinite, 25 per cent potash feldspar and 25 per cent quartz, corresponding to traditional European hard porcelain. After dehydration of the clay the composition of the total system is represented in the ternary phase diagram by the point P1 (figure 7). The total system now consists of the three reactants, potash feldspar, dehydrated clay and quartz, with the corresponding composition points W ($K_2O \cdot Al_2O_3 \cdot 6SiO_2$), P3 ($Al_2O_3 \cdot 2SiO_2$) and SiO_2. The solution of the quartz grains below 1200°C can be neglected, and the quartz phase be regarded as an isolated system, which does not affect the remaining sub-system feldspar-clay relicts.

When the alkali content of the feldspar relicts is decreased, their composition point moves from W toward the point $Al_2O_3 \cdot 6SiO_2$. At the same time the alkali content of the clay relicts is increased, which causes their composition point to move toward $K_2O \cdot Al_2O_3 \cdot 2SiO_2$.

When the firing temperature increases from 1100° to 1200°C the reaction rate of the mullite formation increases very rapidly. At 1200°C the mullite formation may be regarded as completed in both the clay and feldspar relicts, if the feldspar grains are not too large. At this temperature the sub-system contains only mullite and melt in

equilibrium. The melt will have the composition marked by a square point in the diagram and the compositions of the feldspar and clay relicts are given by the points P4 and P5 respectively. This corresponds to a mullite content of 12 per cent in the feldspar relicts and of 52 per cent in the clay relicts. The mullite content within the clay relicts should thus be about four times as great as within the feldspar relicts. This agrees well with the picture of the mullite phase distribution obtained from electron micrographs of etched surfaces and of grains where the glass phase has been dissolved with hydrofluoric acid.

8. Size and Shape of the Mullite Crystals

It is very difficult to describe quantitatively, and simply, the mullite phase of a body as to size, shape and distribution of the crystals. The electron micrographs of etched surfaces give some idea, but local variations are so great that it is difficult to obtain a reliable evaluation of the entire mullite phase (figures 6b and c). The best way is to grind the sample and then isolate the mullite phase by treating with hydrofluoric acid. From the large aggregates of mullite crystals obtained the individual needles can be loosened without any extensive damage and dispersed in water by the action of a colloid mill (figure 8).

In this way the mullite phase from different kinds of porcelain may be investigated and compared, giving the result that mullite phase in technical porcelains fired at different temperatures or with different feldspars may differ considerably as to mean size and size distribution. But we still know very little about the effect of these variations on the properties of the porcelain.

The mullite crystals have throughout the characteristic prismatic needle shape. The length of the needles may be very great in the feldspar relicts. The present author has observed mullite needles 0.05 μ wide and 10 μ long, that is to say, with a proportion of about 200 times between length and width.

As a result of the growth conditions, the crystals may, within small zones, occasionally lie parallel to each other. The mullite aggregate in figure 9 illustrates part of such a feldspar relict. The sample is taken from a ground electrical porcelain and the glass phase in the grain dissolved in hydrofluoric acid. In stereo this picture gives a good idea of the mutual positions of the mullite crystals in the glass. One is inclined to make a comparision with the reinforcing bars used in a concrete structure. We also notice how non-uniform the width of the crystals is, even within this small section. In the same picture can also be seen some smaller crystal aggregates which come from the original clay fields. These aggregates are much more compact, and are made up of small and shorter mullite needles.

Comer has shown the orientation of mullite crystals in three preferred directions 120° to each other in kaolinite flakes fired at low temperatures [4]. In the clay relicts in porcelain these orientation effects cannot be distinguished with certainty. The explanation must be that the kaolinite relicts become deformed by viscous flow, and this hexagonal outline destroyed or disordered.

9. The Dissolution of the Quartz Phase and the Formation of Cristobalite

When discussing the appearance of the quartz grains in the microstructure it is best first to analyze the limiting equilibrium conditions.

It follows from the ternary diagrams, that if a homogeneous melt with the composition point P1 should crystallize under equilibrium conditions, mullite is the primary phase starting crystallization at about 1800°C. When the temperature has decreased to 1230°C, the melt also becomes saturated with tridymite. The melt composition point then follows the boundary line with simultaneous crystallization of mullite and tridymite down to the eutectic at 985°C, where also feldspar starts crystallizing. In solid state there follow two transitions in the silica phase, first to high temperature quartz at 870°C and then to low temperature quartz at 573°C.

There are two important deviations from this equilibrium schedule; (a) the only silica forms that have been observed in technical porcelains are quartz and cristobalite, (b) no crystallization from the melt of either silica or feldspar occurs during the cooling, but a glass phase is formed instead.

When the body is fired, the reactions between clay and feldspar are relatively rapid compared with the dissolution of the quartz grains in the melt. The formation of the mullite phase is mainly completed before the dissolution of the quartz grains becomes noticeable. At the beginning of the dissolution, therefore, the quartz particles

are in a matrix of mullite and melt, where the melt has, on the whole, the same composition.

The composition of the melt phase in a porcelain is determined by the presence of mullite, the temperature, and the amount of quartz dissolved. Starting from the proportion 2:1 of kaolinite and potash feldspar, and assuming that the melt is always saturated with mullite, the composition point of the melt will move during an isothermal quartz dissolution at 1300°C along the corresponding isotherm within the mullite field (figure 10). Experimental data where the quartz and mullite percentages have been determined by X-ray diffraction analyses and then the mean composition of the melt calculated confirm this [11].

The total mullite content is changed only slightly during the dissolution of the quartz. If there is so much quartz in the system that the phase boundary line to the tridymite field is reached just when the quartz has been completely dissolved, the mullite content of the total system will be changed from 23.7 per cent at the beginning of the quartz dissolution to 22.7 per cent at the completion of the dissolution. The dissolution of the quartz is thus attended by a slight decrease in the total mullite content.

If enough quartz is present, the melt will become saturated and the dissolution stops. Then the transformation of the remaining quartz into cristobalite begins. More precisely, the cristobalite phase begins to form when the rate of transition to cristobalite at the phase boundary is greater than the rate of quartz dissolution. The cristobalite phase forms an outer zone round the quartz, and the transformation is apparently a solid state reaction starting from the surface of the quartz grain (figure 11).

The quartz content at the start of the cristobalite formation may be estimated in the following way. At this point, the phase boundary composition of the melt, and after a certain time also the total composition of the melt, correspond to the saturation point of cristobalite. This value is unknown, but may be approximated by the saturation value of the tridymite according to the phase diagram, which gives a somewhat too high result. The difference in temperature between the stable tridymite liquidus surface and the metastable cristobalite surface is only small according to Schairer and Bowen [15].

The dissolution of quartz is a transfer process where alumina and alkali diffuse in the direction towards the quartz surface and there is a mass flow in the melt in the opposite direction. Further, the rate-determining step in the dissolution process is probably the alumina transfer through the crystal-free dissolution zones around the quartz grains. The absence of mullite crystals in the solution rims is due to the fact that the mullite phase in the matrix was already fully developed before the solution of the quartz grains started, and then the solution of the quartz also involves a consumption of alumina resulting in a dissolution of the mullite crystals nearest the quartz grains.

10. Pores and Fracture Surfaces

Sometimes it is of interest to study the appearance of the pores in the fired and sintered body. This is almost impossible with the optical microscope, but the electron microscope, with its greath depth of field, is an excellent tool, and the stereoscopic technique can be used with great advantage in the interpretation of the micrographs [10, 16, 18]. These circumstances will be illustrated by a few pictures.

The first, figure 12, shows closed pores in an unetched fracture surface of a normal insulator porcelain. Information about the size, shape and other characteristics of the pores can be obtained from such micrographs. In this case, for example, a faint image of mullite crystals can be seen on the inside surface of the pores. This reveals a beginning bloating effect in the porcelain. If the porcelain is overfired, an increase in porosity is obtained, due to the release of gases solved in the melt. In the resulting bloating pores, the melt has been forced back and the mullite crystals are left bare, as shown in figure 13.

In the same way, studies of the microstructure of fracture surfaces of whiteware bodies are possible only with the aid of the electron microscope. My own investigations confirm what can be expected from an ocular inspection of the shard. A smooth, high-sheen fracture surface shows that the fracture runs practically independently of the crystal structure, and a grainy surface shows that the fracture runs principally along the old grain boundaries.

In this connection only one especially interesting illustration will be given, figure 14. It is a picture of an unetched fracture surface from a test loaded rod and shows a pore in more unusual surroundings. In one direction the pore merges into a zone with a structure markedly different from both the appearance of the pore and the rest of the fracture surface. This zone was first assumed to be a drying crack, i.e. a local crack formed during drying, and which later was not completely cured in firing. This zone, however, has exactly the same structure as is found on delayed fracture surfaces in porcelain (figure 15), that is, cracks which, under constant or slightly varying stress grow from an outer surface at a very low speed so that the total fracture time might be a matter of years. This may imply that figure 14 illustrates the first stage in the progress of a fracture, beginning at a pore in the material.

11. Degree of Inhomogeneity in the Glass Phase

The porcelain in its entirety is a very heterogeneous material with crystalline phases and pores dispersed in a glass matrix. The distribution of the mullite phase is very uneven between the clay and the feldspar relicts, which emphasizes the heterogeneity by giving the different regions different properties.

However, the most important phase is the continuous glass phase, which gives porcelain its fundamental properties. What we want to know about the glass phase is its local composition or degree of inhomogeneity. The direct experimental study of this in the glass phase is subject to great difficulties.

A common mistake made earlier was to draw conclusions regarding the homogeneity of the glass phase from values of the diffraction index measured on thin sections observed in the optical microscope. As a matter of fact these observations have not been made on a glass phase, but on a two phase system, glass and mullite, with varying mullite content. This has given rise to the opinion that the glass phase in fired porcelain is most inhomogeneous, having different compositions in different regions. The high viscosity of the system has also contributed to this opinion, but on this point it must be remembered that the high apparent viscosity can only partly be traced back to the melt phase, for the dispersed mullite phase increases it most efficiently.

Instead conclusions regarding the homogeneity of the glass phase must be drawn indirectly from a combination of (a) quantitative phase determinations, (b) rate measurements, and (c) electron microscopic observations of the phase distribution. Such studies have indicated that the melt phase is not at all so inhomogeneous as previously believed, but instead has its composition regulated by the presence of the mullite phase. The kinetic data provide evidence that at temperatures above 1200°C, equilibrium conditions between melt and mullite phase are approximately reached. This is also true of the feldspar regions once the mullite phase is formed there. The high transfer rates are due to the high specific surface of the mullite phase, giving short diffusion distances in the melt phase.

The greatest degree of inhomogeneity in the glass phase is caused by the dissolution of the quartz grains. The rate determining step is here assumed to be the alumina diffusion from the adjacent mullite crystals, causing the essential part of the concentration gradient to fall within the crystal-free solution rims around the quartz grains.

Within the types of porcelain in which a cristobalite phase is formed, this concentration gradient has disappeared, too. The highest degree of homogeneity in the glass phase will thus be reached in porcelain bodies with no quartz phase or with such high quartz content that the melt has become saturated and cristobalite formed.

12. Internal Microstresses

Due to the great difference in the thermal expansion coefficient between the crystalline quartz and the glass phase, high internal microstresses arise in the porcelain during the cooling of the body.

A knowledge of the kind and magnitude of these stresses is very important when studying and explaining the influence of microstructure on such properties as thermal expansion and mechanical strength. This knowledge has to be gained by theoretical analyses combined with experimental measurements on thermal expansion behavior and on the induced strain in the lattice of the crystalline phases.

The quartz grains strive to contract more than the glass matrix during the cooling of the body. As a result tensile stresses arise in the quartz grain. In the surrounding glass phase radial tensile stresses and tangential compression stresses are formed, both having their largest value at the boundary to the glass phase and then rapidly

decreasing with incereasing distance from the quartz grain. The analysis also shows that the tensile stresses within the quartz grains decrease with increasing quartz content, and that they are independent of the grain size at constant quartz percentage [11].

For example, experimental strain measurements on a particular porcelain body with 6 per cent quartz gave a mean tensile stress in the quartz phase of about 4200 kg/cm^2. This value may be compared with the normal range for the modulus of rupture of porcelain, 500-1000 kg/cm^2, and the estimated flow point of silicate glasses 20,000 kg/cm^2.

The question now arises whether these internal stresses are of such a size that they may cause local fractures, with microfissures within or around the quartz grains as indicated in the micrographs (figure 16). The modulus of rupture for porcelain is much lower but refers to much larger volumes and gives, therefore, no information in this case, owing to the statistical nature of strength. Measurements of the strain in the quartz phase, and of the temperature dependence of the thermal expansion, indicate that the stress state is the normal and dominant one, but they do not exclude the existence of microcracks [11].

Microfissures of this kind are believed to exist in porcelain bodies [6, 7, 9], but no reliable data on their frequency have yet been forthcoming. If they do exist, they must be weak points in the material and presumptive starting points for growing cracks when the body is mechanically loaded. A decrease in the grain size of the quartz is known to give an increase in both mechanical strength and thermal expansion coefficient, and these effects could then be explained by the decrease in size and frequency of the microfissures.

If microfissures do not exist, but only the microstresses, what does that mean to the mechanical strength? The existence of high tensile stresses in the quartz grains and of high radial tensile stresses in the surrounding glass phase must be a weakness especially regarding the crack nucleation during loading. The existence of the tangential compression stresses must, on the other hand, make the crack nucleation in these directions and crack propagation in the glass phase more difficult. Which of these two effects is the most important is very much disputed [13, 19]. An increase of the quartz content in the porcelain usually means an increase in mechanical strength, and this effect might be explained by the decreased proportion of the weaker glass phase combined with higher mean tangential compression stresses in the glass phase.

13. The Microstructure of Porcelain - an Exhausted Field of Research?

There is always a need for improving the limiting properties of a material, and porcelain is no exception. In technical porcelains, for instance, mechanical strength is frequently the limiting property. In order to improve it in an efficient way, we must aquire a much better understanding of the influence of the microstructure than we have at present.

The electron microscope and the X-ray diffraction technique have given us a clear picture of the microstructure as far as the percentages and phase distributions are concerned. But we have to go further and investigate structural details in the continuous glass phase, such as concentration gradients, pores, microfissures and solved gases, in order to elucidate the effects of these different factors. The main interest will be centered around the glass phase, and around the crystal phases mostly as modifiers of the glass phase properties.

As to mechanical strength, special attention must also be paid to the surface structure and the chemical conditions there. We do not yet know the nature of the weak points in the porcelain, nor the nucleation mechanism of the cracks in the fracture, or if there is a possibility of stopping a crack once it has started. We have only some empirical rules to follow but no real understanding.

The microstructure of porcelain and its influence on the material properties is thus far from being an exhausted field of research, and there is still scope for significant future developments and improvements in this ancient and highly appreciated material.

References

[1] G. W. Brindley and M. Nakahira, J. Am. Ceram. Soc. 40, 346 (1957).

[2] G. W. Brindley and M. Nakahira, J. Am. Ceram. Soc. 42, 311 (1959).

[3] G. W. Brindley and D. M. Maroney, J. Am. Ceram. Soc. 43, 511 (1960).

[4] J. J. Comer, J. Am. Ceram. Soc. 43, 378 (1960).

[5] A. Dietzel and N. N. Padurow, Ber. deut. keram. Ges. 31, 7 (1954).

[6] W. H. Earhart, Ohio State Univ. Eng. Sta. News 12, 25 (1940); Ceram. Abstr. 19, 206 (1940).

[7] R. F. Geller, D. N. Evans and A. S. Creamer, Bur. Standards J. Research 11, 327 (1933).

[8] W. D. Kingery, Introduction to Ceramics, p. 148, John Wiley & Sons (New York, 1960).

[9] I. M. Lachman and J. O. Everhart, J. Am. Ceram. Soc. 39, 30 (1956).

[10] S. T. Lundin, Trans. 4th Intern. Ceram. Congr. Florence, p. 383 (1954).

[11] S. T. Lundin, Studies on Triaxial Whiteware Bodies, Almqvist & Wiksell (Stockholm, Sweden, 1959).

[12] W. S. MacKenzie and J. V. Smith, Am. Mineralogist 40, 707 (1955); ibid 41, 405 (1956).

[13] R. Masson, Trans. 8th Intern. Ceram. Congr. Copenhagen, p. 393 (1962).

[14] J. F. Schairer and N. L. Bowen, Am. J. Sci. 245, 193 (1947).

[15] J. F. Schairer and N. L. Bowen, Am. J. Sci. 253, 681 (1955).

[16] K. Schüller, Ber. deut. keram. Ges, 38, pp. 150, 208 and 241 (1961).

[17] G. R. Shelton, J. Am. Ceram. Soc. 31, 39 (1948).

[18] H. Stäger and H. Studer, Tech. Mitt. 49, 170 (1956).

[19] A. Winterling, Ber. deut. keram. Ges. 38, 9 (1961).

FIGURE 1. Electrical insulator porcelain with extensive quartz grain dissolution (etched 10 sec, 0 °C, 40% HF, collodion replica).

FIGURE 2. Electrical insulator porcelain with low quartz grain dissolution (etched 10 sec, 0 °C, 40% HF, collodion replica).

FIGURE 3. Vitreous sanitary ware (etched 10 sec, 0 °C, 40% HF, collodion replica).

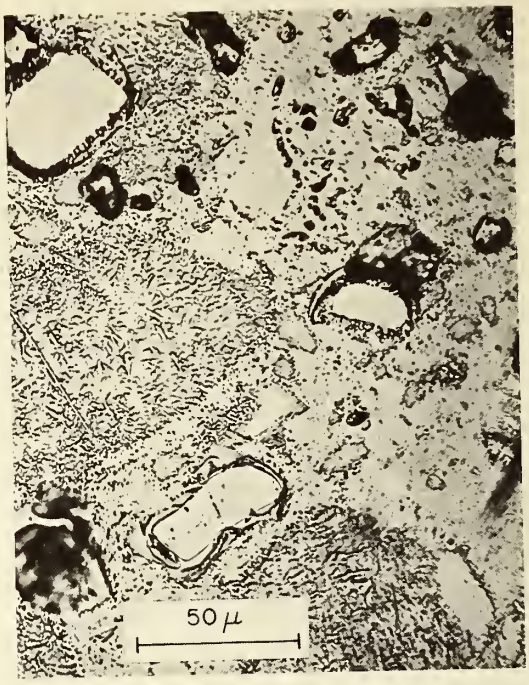

FIGURE 4. Vitreous triaxial whiteware body fired at 1300 °C (etched 20 min, 50% NaOH, 100 °C, collodion replica).

a

b

FIGURE 5. Two examples (a and b) of electron micrographs of electrical insulator porcelain (etched 10 sec, 0 °C, 40% HF, silica replica).

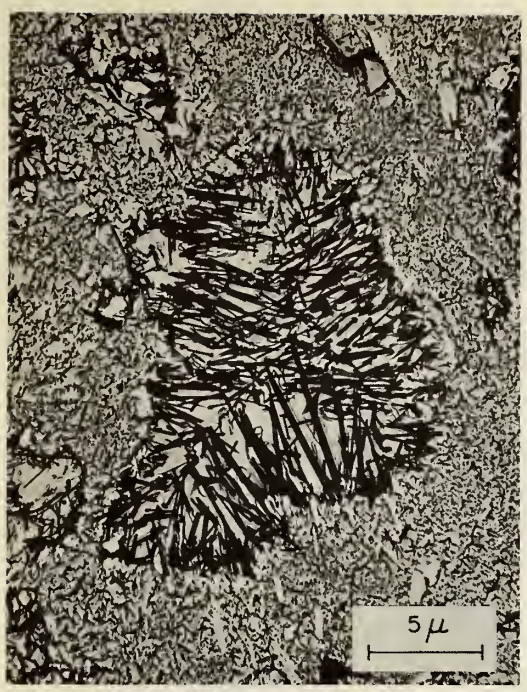

a

b

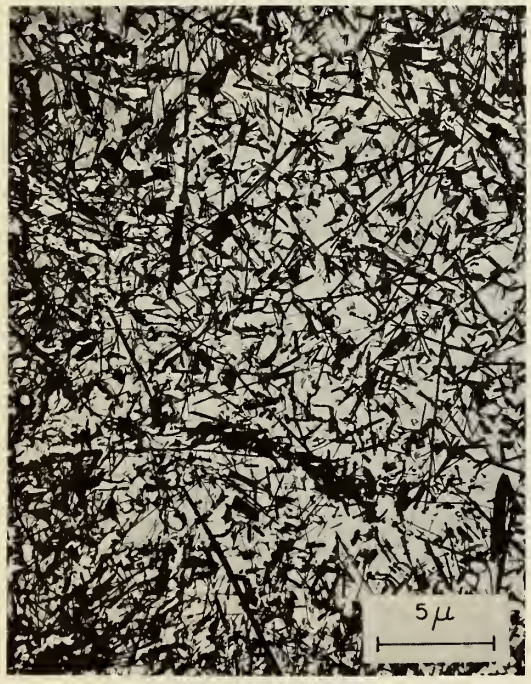

c

FIGURE 6. Mullite needles growing into feldspar relicts (insulator porcelain, etched 10 sec, 0 °C, 40% HF); (a) silica replica, (b) aluminum replica, (c) silica replica.

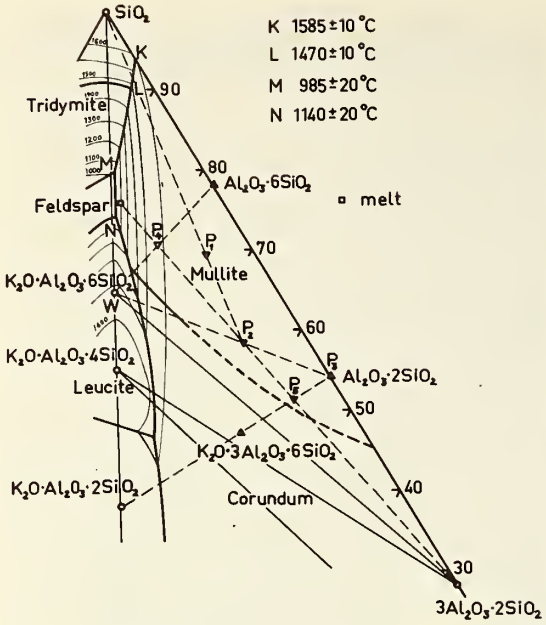

FIGURE 7. Portion of the phase diagram for the system K_2O-Al_2O_3-SiO_2 after Schairer & Bowen [14,15]. The composition points correspond to, P1= total system. P2 = sub-system clay and feldspar, P3 = metakaolin, P4 = feldspar relicts, and P5 = clay relicts.

FIGURE 8. Isolated and dispersed mullite phase of an insulator porcelain.

FIGURE 9. Stereoscopic views of a part (the large aggregate) of the mullite phase from a feldspar relict region showing the magnitude and relative position of the mullite crystals. To the left some smaller, more compact aggregates from clay relicts can be seen.

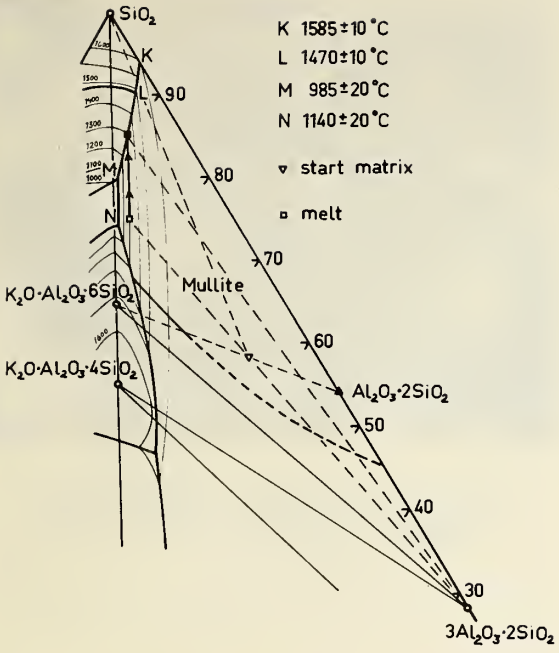

FIGURE 10. The change in melt composition during the quartz dissolution, when the melt is saturated with mullite.

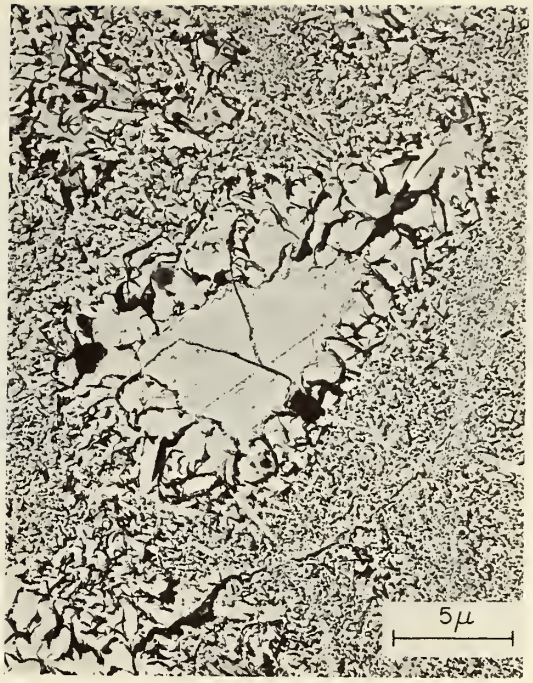

FIGURE 11. Quartz grain partly transformed into cristobalite (etched 20 min, 50% NaOH, 100 °C, silica replica).

FIGURE 12. Stereoscopic views of closed pores in an unetched fracture surface (aluminium replica).

FIGURE 13. Closed pore with mullite crystals in an overfired body (unetched fracture surface, aluminium replica).

FIGURE 14. Pore with crack in an unetched fracture surface (aluminium replica).

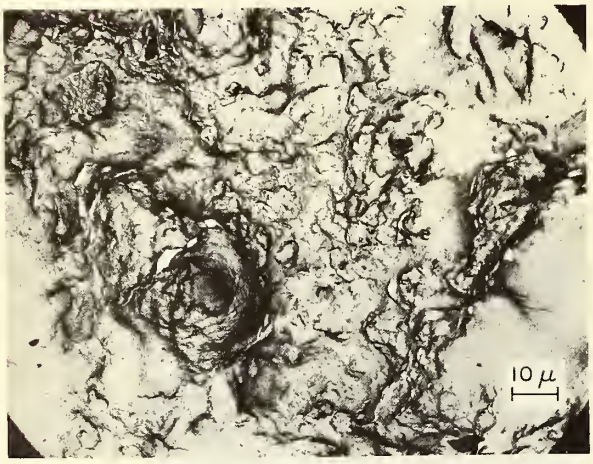

FIGURE 15. Surface structure of a delayed fracture in an electrical porcelain insulator (aluminium replica).

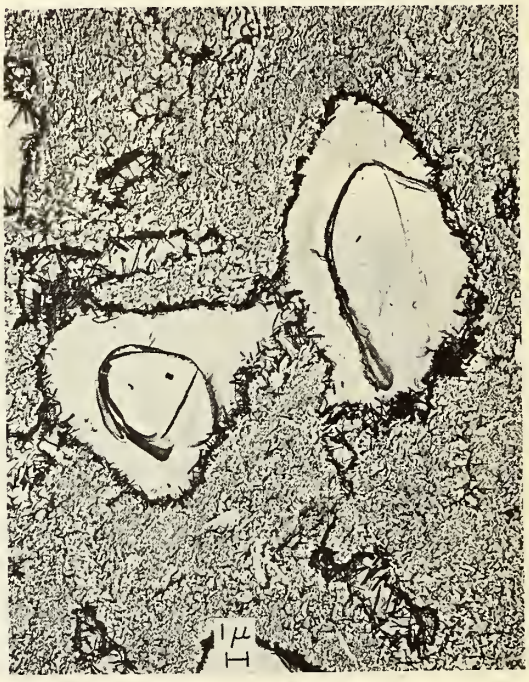

FIGURE 16. Partly dissolved quartz grains with microstress cracks (fracture surface, silica replica).

☆ U S GOVERNMENT PRINTING OFFICE : 1964 O - 720-834

PENN STATE UNIVERSITY LIBRARIES
A00007191989